# Turbulent Gas Breakup Modeling and Acoustic Void-Fraction Determination Studies in Support of Cavitation Damage Mitigation of the Spallation Neutron Source Target Vessel

**A Dissertation Presented for the Doctor of Philosophy Degree**

**The University of Tennessee, Knoxville**

**Stuart Alexander Walker**

**May 2012**

# ABSTRACT

Pressure pulses induced by proton beam deposition lead to cavitation and pitting erosion of the Spallation Neutron source (SNS) target vessel; this damage limits the lifetime of the vessel. Dampening the pressure pulse by adding compressibility to the bulk mercury in the form of microbubbles is a promising technique for damage mitigation. The physics governing gas bubble breakup in turbulent flows is examined leading to mechanistic based scaling models for the gas breakup in a swirling jet type microbubble generator. These models are verified experimentally in an air/water system using a commercial swirling jet bubbler and compared to a legacy empirical model. Verifying the performance of a microbubble generator in a liquid metal application requires knowledge of both the gas void fraction and the bubble size distribution. Since the sound speed in a bubbly mixture is a strong function of the gas void fraction, a fixed point auto-correlation technique is developed to determine the sound speed in a bubbly mixture. The auto-correlation method is verified in a water solid waveguide using a driven piston source and stationary hydrophone.

# TABLE OF CONTENTS

# LIST OF FIGURES

# List of Tables

## LIST OF SYMBOLS AND ABBREVIATIONS

$Q_i$ , total energy

$m_i$ , mass

$c_p$ , constant pressure heat capacity

$c_v$ , constant volume heat capacity

$c$ , sound speed

$p$ , pressure

$\rho$ , density

$\tau$ , external forces

$\mu_i$ , dynamic viscosity

$\nu$ , kinematic viscosity

$\nu_t$ , turbulent viscosity

v, fluid velocity

$D_i$ , diameter

$\sigma$ , surface tension

$N_i$ , dimensionless group

$\dot{V}$, volumetric flow rate

$L_i$, length

$f$, friction factor

$\omega$, swirl rate

$\beta$, scale parameter

$\alpha$, scale parameter

$K$, constant of proportionality

$\Delta$, dimensionless diffusivity

$B_i$, bulk modulus

$k_i$, thermal conductivity

$R_0$, bubble radius

$\delta_{pen}$, thermal penetration depth

$\varepsilon$, energy dissipation rate

Subscripts

*beam*, incident beam

target, SNS target module

$d$ , droplet

$We$ , Weber number

$Vi$ , viscosity group

$crit$ , conditions for critical bubble size

max , maximum

$l$ , liquid

$pipe$ , SNS flow system pipe

Re , Reynolds number

$g$ , gas

$exit$ , nozzle exit

$loss$ , pressure loss

$m$ , mixture

$a$ , adiabatic

$T$ , isothermal

$WG$ , waveguide

# 1 Introduction

A wide variety of research endeavors use neutron scattering techniques to study the geometry, motion, and interaction of atoms within a material. The Spallation Neutron Source (SNS) utilizes a one gigaelectron volt proton beam of near 1.4 M-Watt time averaged power impinging on a liquid mercury target to obtain the world's highest pulsed neutron beam intensity. The proton energy deposition occurs within the target in approximately one microsecond with a pulse repetition frequency of 60 Hertz.

The power deposited in the target induces significant material stresses which lead to mechanical failure in solid target neutron sources. Liquid metals are not subject to radiation damage or fatigue stress, which coupled with a high atomic number, makes a liquid mercury target ideal [2]. However, the deposition of power generates a pressure pulse within the mercury target and the interaction of the pressure pulse with the stainless steel pressure boundary causes cavitation pitting and erosion, which could limit the lifetime and operational power of the SNS facility [3].

Several promising methods of mitigating the effects of cavitation result from increasing the liquid mercury compressibility, thereby decreasing the pressure amplitude caused by the pulse energy deposition. Methods of increasing the compressibility of the system are currently being tested extensively and involve introducing a gas wall at the pressure boundary and introducing a homogeneous cloud of small gas bubbles within the target volume. Gas wall methods have shown progress with the introduction of surface topography to control the gas near the wall; however reliably positioning a gas layer and subsequent gas removal are significant engineering opportunities which must be addressed [4]. Small gas bubble addition to the bulk fluid has proven to be a practical cavitation damage mitigation strategy due to low gas solubility in the mercury [5]. Small bubbles that normally dissolve in water or organic fluids have long lifetimes and will persist in the mercury flow loop [5]. Bubble removal methods may be required if coalescence results in large bubbles or stratified coolant flow [6].

Generating microbubbles in liquid metals is another engineering opportunity. Swirling jets with coaxial gas flow are used in the environmental and chemical processing industries to generate small gas bubbles in organic solutions and may be a viable technique for microbubble generation at the SNS [11]. The modeling of the physics for the gas filament break-up is not well established, and this impedes scaling of the device to use with fluids other than water and organics where data are available [19]. Observations of the physical break-up phenomena leading to scaling relationships describing the average bubble diameter are presented. These relationships are then compared to empirical models in water using a commercial swirling jet device.

Verifying the performance of homogeneous bubble injection methods for damage mitigation within the mercury target requires the measurement of bubble populations, including size distribution and gas volume fractions. Two strategies for determining sound speeds in bubbly mixtures along a waveguide which involve measuring pressure nodes and antinodes have been presented in the literature [20,21]. A fixed point strategy measures the wavelength of standing waves using a fixed sensor and varying frequency while a fixed frequency method uses a fixed frequency and moving sensor. A fixed point strategy is ideal for the SNS environment; however, these techniques present sound speed resolutions which are limited by the time required to establish sufficient acoustic energy to form standing wave modes. A single-point correlation technique is presented as the basis for a fixed point void-fraction measurement strategy suitable for the SNS application. Several notable features of this strategy include: fixed pressure sensors, single (or a few) drive frequencies, and resolution limited by the system hardware/software sampling rates.

Chapter 2 discusses the spallation neutron source facility and beam energy deposition within the mercury target. The development of turbulent gas break-up models based on droplet deformation physics as well as the results of comparison with legacy empirical models is then presented in Chapter 3. This enables the scaling of a swirling jet bubbler from water/air to a mercury/helium system. A fixed point void-fraction measurement strategy is outlined in Chapter 4. Sound speeds in a pure water system are measured in a vertical waveguide using the single point correlation technique. This water solid data set establishes the single point correlation technique as an experimentally viable theoretical method of determining sound speeds in a waveguide.

The major original contributions of this work include the presentation of mechanistic based scaling models describing the gas breakup of a commercial swirling jet bubbler and the theoretical foundation for a fixed point void-fraction measurement strategy. These two ideas further the knowledge base required to successfully mitigate cavitation damage to the SNS target vessel.

# 2 SPALLATION NEUTRON SOURCE

## 2.1 DESCRIPTION OF THE SNS FACILITY

The Spallation Neutron Source is a high power accelerator driven user facility located at the Oak Ridge National Lab in Oak Ridge, TN. The accelerator complex is shown in Figure 2.1.1. Negatively charged hydrogen ions are produced and accelerated to an energy of 2.5MeV in the front-end system. The hydrogen ion beam is delivered to a large linear accelerator, or linac, which consists of three separate accelerators. The drift-tube linac and coupled-cavity linac accelerate the beam to an energy of about 200MeV. Superconducting niobium cavities, which are cooled using liquid helium to an operating temperature of 2K, further accelerate the beam to an energy of 1 GeV. The 1 GeV hydrogen ion beam is injected into an accumulator ring structure that bunches the ions for delivery to the mercury target. The accumulated ion beam is passed through a stripper foil which removes the electrons leaving a proton beam with time averaged power of 1.4 MW. The proton beam impinges on a liquid mercury target housed in a stainless steel flow system; the flow system is shown in Figure 2.1.2. The mercury target flow system contains a total circulating volume of 1360 liters (18,400 kg-Hg) while the target module, shown in Figure 2.1.3, contains a volume of 60 liters (795 kg-Hg). The proton beam interacts with the mercury target through a spalling reaction to create high energy neutrons. The high energy neutrons are moderated using water and liquid hydrogen. The moderated neutrons are directed down 18 instrument beam lines. [7,8]

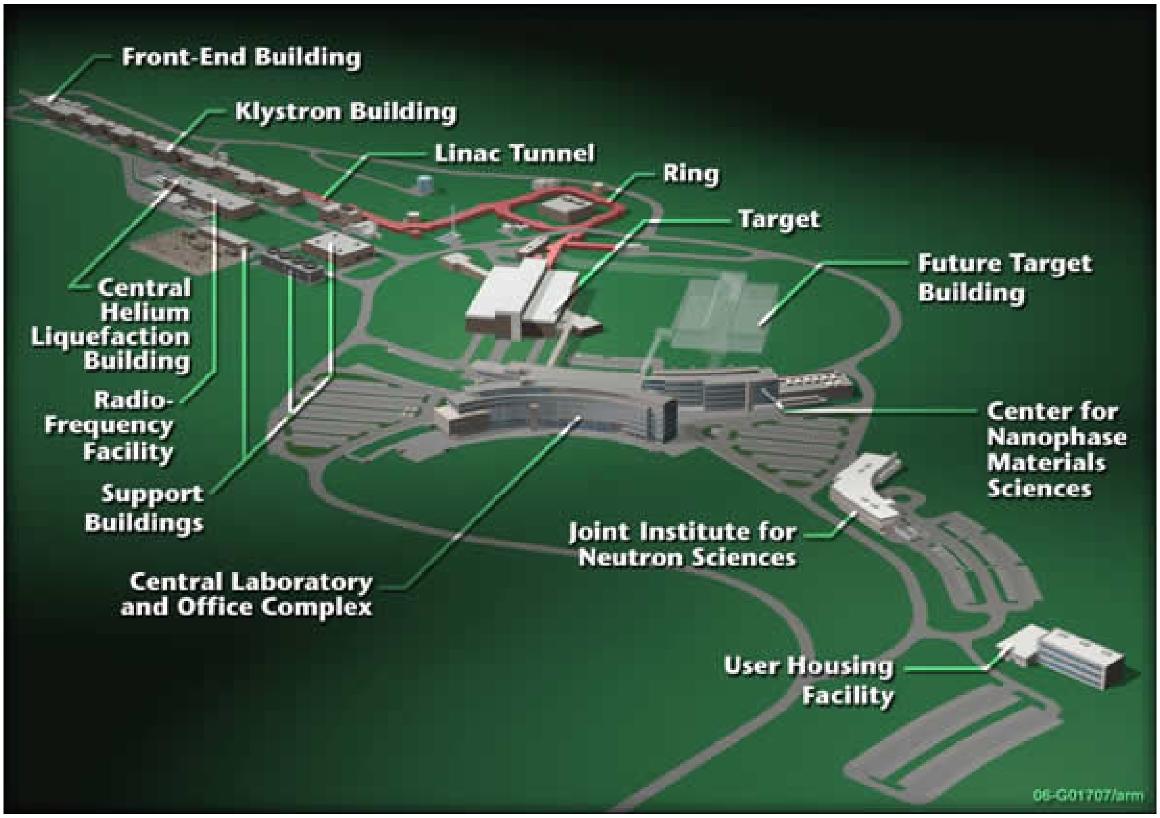


Figure 2.1.1: Conceptual drawing of the SNS accelerator complex; courtesy of ORNL Neutron Sciences [8].

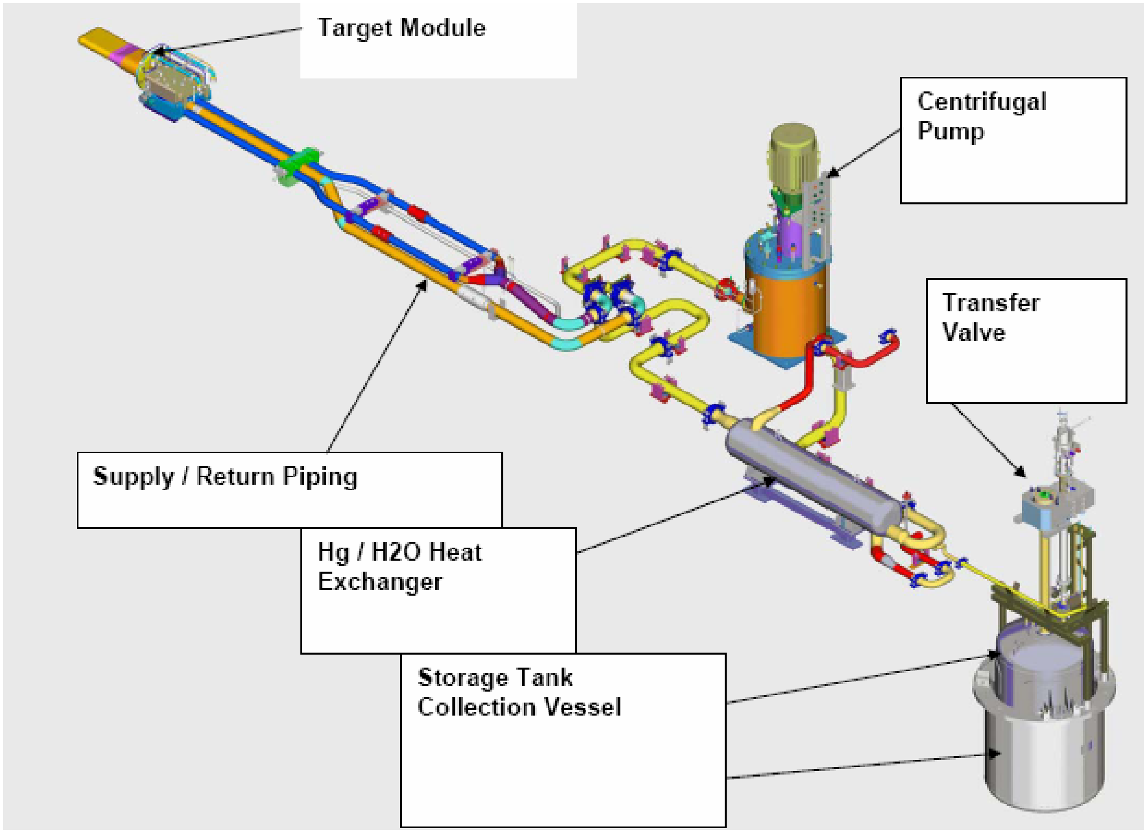


Figure 2.1.2: Mercury flow system; image courtesy of Peter Rosenblad [7].

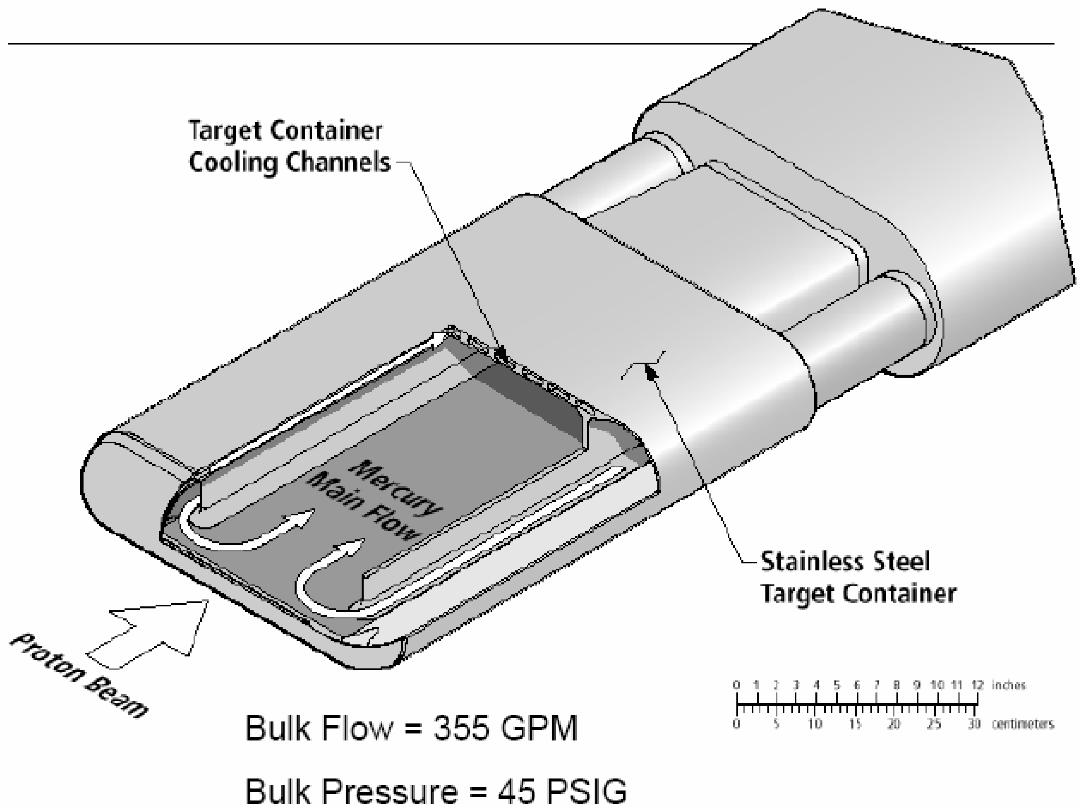


Figure 2.1.3: SNS target module revealing bulk mercury flow pattern; image courtesy of Peter Rosenblad [7].

## 2.2 ENERGY DEPOSITION IN THE SNS TARGET

At the SNS facility the beam energy deposition occurs in the target according to,

$$Q = mc_v \Delta T \tag{2.2.1}$$

where $c_v$ is the specific heat capacity for a constant volume process, and m is the mass of the target material that stops the beam energy, Q, causing temperature rise, $\Delta T$. The initial energy deposition is a constant volume process because the sound speed in mercury is near 1400 m/s, such that pressure information can only move 1.4 mm during the energy deposition event of one microsecond. This causes a constant volume temperature rise, which elevates the local pressure following the equation of state for the mercury. Referring back to Figure 2.1.3, the proton beam energy is deposited on the nose region; this energy deposition causes a shock wave due to the local pressure rise in the mercury. The pressure induced in the target mass absorbing the beam energy can be approximated from the sound speed equation, which provides a relationship between pressure and density for an isentropic process,

$$c^2 = \left.\frac{dP}{d\rho}\right|_s \tag{2.2.2}$$

Combining (2.2.1) and (2.2.2) using the chain rule, the pressure induced by one pulse is approximately (2.2.3)

$$\Delta P \cong c^2 \left[\frac{Q}{mc_v}\right] \frac{d\rho}{dT} \tag{2.2.3}$$

Where the heat capacity is for a constant volume process. The isentropic process line lies between the constant pressure and constant volume process lines. The difference in heat capacities for these two processes is written as

$$C_p - C_v = V_m T \frac{\alpha^2}{\beta_T} \tag{2.2.4}$$

Where α is the isobaric coefficient of thermal expansion and β is the isothermal compressibility. Using values given in Appendix A, the difference in heat capacities for mercury is $C_p - C_v = 4.8 \times 10^{-22} \, {}^{J}\!/_{mol \cdot K}$ and for water the difference is $C_p - C_v = 9.0 \times 10^{-21} \, {}^{J}\!/_{mol \cdot K}$. This shows that for an isentropic process the heat capacity is essentially the same as the isobaric case therefore Eq. 2.2.3 can be stated as

$$\Delta P = c^2 \left[ \frac{Q}{mc_p} \right] \frac{d\rho}{dT} \tag{2.2.5}$$

The pressure increase relates the target material sound speed, mass, specific heat capacity, and thermal expansion to the deposition energy. [1] Thus to limit pressure changes while preserving performance, a target with low sound speed and thermal expansion, while also having a high volume specific heat capacity is desirable.

## 2.3 Beam Deposition Modeling

The propagation of the pressure wave that results from the proton beam energy deposition can be thought of as the inverse of the water-hammer pressure pulse that results from a sudden stop of flow; where a sudden valve closure provides the appropriate change in kinetic energy. From 2.2.3, a 1MW energy deposition corresponds to a nominal pressure increase for a mercury target of approximately 20MPa [9]. For a constant area duct, Figure 2.3.1, the 20 MPa pressure change can be thought of as the result of an abruptly stopped flow through the following relationship [10]

$$\Delta P = \rho c v_0 \tag{2.3.1}$$

With a mercury density of $\rho = 13{,}500\, kg/m^3$ and sound speed $c = 1{,}500\, m/s$ the associated stopped flow velocity is $v_0 \cong 1 m/s$. In other words, the change in kinetic energy associated with a $v_0 \cong 1 m/s$ mercury flow being stopped by a sudden valve closure generates a system pressure increase of 20MPa. This is modeled below using a 1D finite element model. The model is then used to predict the pressure increase associated with a similar change in kinetic energy for a bubbly mixture where $c = 150\, m/s$.

The complex target geometry is reduced to a 1D pipe geometry for simplicity of modeling while still preserving the wave physics required to demonstrate a reduction in peak pressure. The following development details a finite element solution of the mass and momentum conservation principles suitable for simulating the propagation of the pressure pulse in a single component 1D system.

The mass and momentum balances for inviscid incompressible isothermal single phase flow through a constant cross section 1D geometry generates

$$\frac{\partial P}{\partial t} + A \cdot \frac{\partial v}{\partial x} = 0 \tag{2.3.1}$$

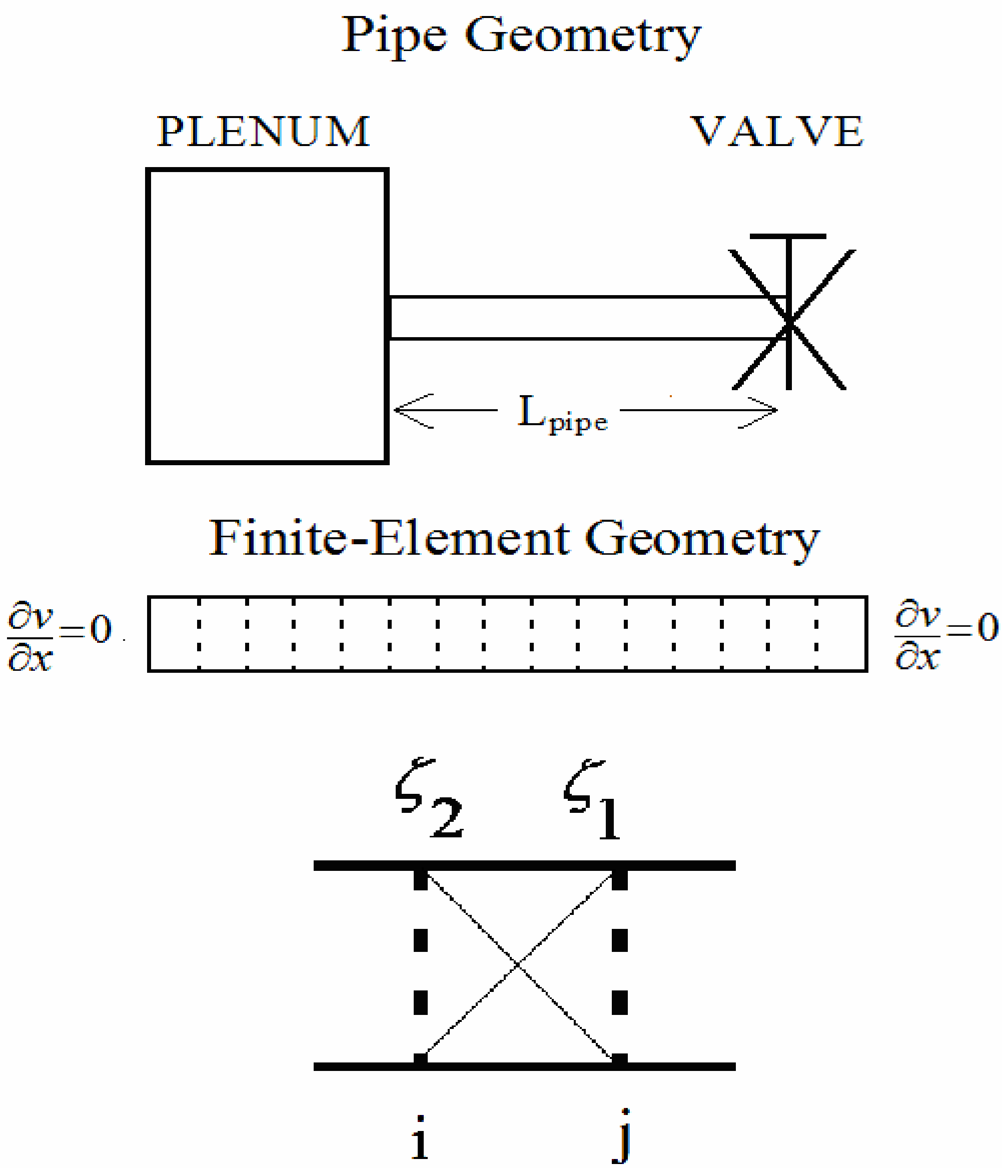


Figure 2.3.1. Water-hammer geometry, finite-element nodalization, and element basis function geometry.

$$\frac{\partial v}{\partial t} + B \cdot \frac{\partial P}{\partial x} = 0 \tag{2.3.2}$$

Where $A = \rho c^2$ and $B = 1/\rho$.

A one-dimensional model of the target window response to the proton beam energy deposition is developed in [9] using the wave equation which results from the combination of (2.3.1) and (2.3.2). This development is based on Figure 2.3.2 where the mercury is modeled in 1D and the target window is constrained by a spring. A finite difference technique is used to approximate the linear second order wave equation. This model is validated for the case of a target window with no mass and infinite compliance; this case is reexamined below using a Galerkin weak statement method.

A finite-element approximation to the 1D mass and momentum conservation principles in Equations (2.3.1) and (2.3.2) is developed which can handle non-linearities in the A and B coefficients. Further, the weak statement formulation provides several advantages over traditional difference techniques. The weak statement formulation is amenable to numerical error quantification. Also, the weak form allows the nodal interpolating functions to be defined following the discretization of the domain.

Equations (2.3.1) and (2.3.2) can be handled concisely in flux-vector form, (2.3.3), given the definitions of the coupled components in (2.3.4).

$$\vec{q}_t + \overline{\overline{C}} \cdot \vec{q}_x = 0 \tag{2.3.3}$$

$$\vec{q} = [P, v]^T ; \overline{\overline{C}} = \begin{bmatrix} 0 & A \\ B & 0 \end{bmatrix} \tag{2.3.4}$$

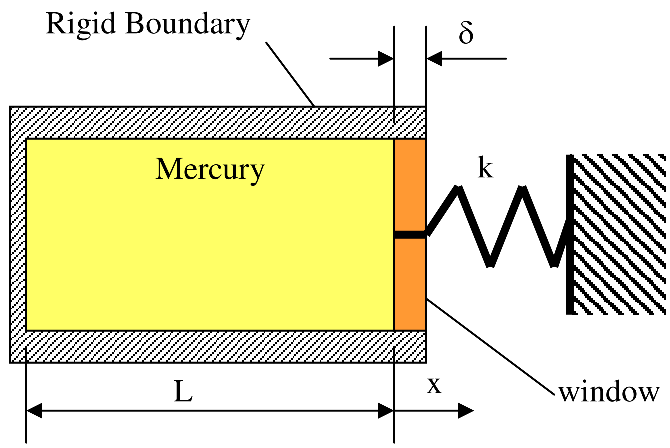


Figure 2.3.2: One-Dimensional Window Response Model of a spring-mass system [9].

Application of an approximate Galerkin weak statement yields (2.3.5) and (2.3.6).

$$GWS = \int_{\Omega} \Psi \cdot \left( \frac{\partial \vec{q}}{\partial t} + \overline{\overline{C}} \cdot \frac{\partial \vec{q}}{\partial x} \right) \cdot d\tau = 0 \tag{2.3.5}$$

$$GWS^{N} = \int_{\Omega} \Psi \cdot \left( \frac{\partial \vec{q}^{N}}{\partial t} + \overline{\overline{C}} \cdot \frac{\partial \vec{q}^{N}}{\partial x} \right) \cdot d\tau = 0 \tag{2.3.6}$$

A discretization of the domain allows the pressure and velocity to be interpolated using a polynomial; thus the only remaining unknowns are the nodal values. Consider a linear 1D element with linear interpolating polynomials given in (2.3.7). The nodal values of the pressure and velocity are defined in (2.3.8); this element definition generates the coupled interpolating polynomial given in (2.3.9). [27]

$$\begin{bmatrix} \zeta_1 \\ \zeta_2 \end{bmatrix}_e = \begin{bmatrix} 1 - \bar{x}/\ell_e \\ \bar{x}/\ell_e \end{bmatrix}_e \tag{2.3.7}$$

$$Q_e = \begin{bmatrix} \vec{q}_i & \vec{q}_j \end{bmatrix}_e^T = \begin{bmatrix} P_i & v_i & P_j & v_j \end{bmatrix}_e^T \tag{2.3.8}$$

$$\Psi_e = \begin{bmatrix} \tilde{\zeta}_i & \tilde{\zeta}_j \end{bmatrix}_e^T = \begin{bmatrix} \zeta_i & 0 & \zeta_j & 0 \\ 0 & \zeta_i & 0 & \zeta_j \end{bmatrix}_e^T \tag{2.3.9}$$

The pressure and velocity are approximated across an element by the linear combination of the interpolating polynomials and the nodal values according to (2.3.10).

$$\vec{q}^{N}(\zeta) = \Psi_e^T \cdot Q_e = \begin{bmatrix} \tilde{\zeta}_i & \tilde{\zeta}_j \end{bmatrix}_e \begin{bmatrix} \vec{q}_i \\ \vec{q}_j \end{bmatrix}_e = \tilde{\zeta}_i \cdot \vec{q}_i + \tilde{\zeta}_j \cdot \vec{q}_j \tag{2.3.10}$$

The action of the coupled interpolation is shown explicitly in (2.3.11).

$$\vec{q}^{\,N}(\zeta) = \begin{bmatrix} \tilde{\zeta}_1 & \tilde{\zeta}_2 \end{bmatrix}_e \begin{bmatrix} \vec{q}_i \\ \vec{q}_j \end{bmatrix}_e = \begin{bmatrix} \zeta_i \cdot P_i + \zeta_j \cdot P_j \\ \zeta_i \cdot v_i + \zeta_j \cdot v_j \end{bmatrix}_e = \begin{bmatrix} P \\ v \end{bmatrix}_e \tag{2.3.11}$$

Finally define the coupled data matrix for an element in (2.3.12).

$$\overline{\overline{C}}_e = \begin{bmatrix} 0 & A & 0 & A \\ B & 0 & B & 0 \\ 0 & A & 0 & A \\ B & 0 & B & 0 \end{bmatrix}_e \tag{2.3.12}$$

The nodal interpolations are linearly dependent therefore the discretization requires the approximate GWS to be written as an element summation over the entire domain, (2.3.13).

$$GWS^N = \sum_{\mu=1}^{N_e} \left( \int_{\Omega_e} \Psi_e \cdot \Psi_e^T \cdot d\tau \cdot \frac{\partial Q_e}{\partial t} + \overline{\overline{C}}_e \cdot \int_{\Omega_e} \Psi_e \cdot \frac{\partial \Psi_e^T}{\partial x} \cdot d\tau \cdot Q_e \right) = 0 \tag{2.3.13}$$

This form shows that the integrals are independent of the nodal values and are therefore formed once for a generic element and applied to any number of elements according to

$$GWS^N = \sum_{\mu=1}^{N_e} \left( [A200L]_e \cdot \frac{\partial Q_e}{\partial t} + \overline{\overline{C}}_e \cdot [A201L]_e \cdot Q_e \right) = 0 \tag{2.3.14}$$

Where the integration over the element is indicated symbolically; i.e. the prefix “A” and suffix “L” denotes a linear 1D element and the “200” indicates the integration of the undifferentiated basis functions while the “201” indicates the integration of the undiffereatiated basis function with a post-multiplied first derivative. The element integrations are performed explicitly for the first element in (2.3.15) and (2.3.16).

$$[A200L]_e = \int_{\Omega_e} \Psi_e \cdot \Psi_e^T d\tau = \int_{\Omega_e} \begin{bmatrix} \tilde{\zeta}_1 \\ \tilde{\zeta}_2 \end{bmatrix}_e \cdot \begin{bmatrix} \tilde{\zeta}_1 \\ \tilde{\zeta}_2 \end{bmatrix}_e^T d\tau = \int_{\Omega_e} \begin{bmatrix} \zeta_1 & 0 \\ 0 & \zeta_1 \\ \zeta_2 & 0 \\ 0 & \zeta_2 \end{bmatrix}_e \cdot \begin{bmatrix} \zeta_1 & 0 \\ 0 & \zeta_1 \\ \zeta_2 & 0 \\ 0 & \zeta_2 \end{bmatrix}_e^T d\tau$$
$$= \int_{\Omega_e} \begin{bmatrix} \zeta_1\zeta_1 & 0 & \zeta_1\zeta_2 & 0 \\ 0 & \zeta_1\zeta_1 & 0 & \zeta_1\zeta_2 \\ \zeta_2\zeta_1 & 0 & \zeta_2\zeta_2 & 0 \\ 0 & \zeta_2\zeta_1 & 0 & \zeta_2\zeta_2 \end{bmatrix}_e d\tau = \ell_e \cdot \frac{1}{6} \cdot \begin{bmatrix} 2 & 0 & 1 & 0 \\ 0 & 2 & 0 & 1 \\ 1 & 0 & 2 & 0 \\ 0 & 1 & 0 & 2 \end{bmatrix}_e \tag{2.3.15}$$

$$[A201L]_e = \int_{\Omega_e} \Psi_e \cdot \frac{\partial \Psi_e^T}{\partial x} d\tau = \int_{\Omega_e} \begin{bmatrix} \tilde{\zeta}_1 \\ \tilde{\zeta}_2 \end{bmatrix}_e \cdot \begin{bmatrix} \dfrac{\partial \tilde{\zeta}_1}{\partial x} \\ \dfrac{\partial \tilde{\zeta}_2}{\partial x} \end{bmatrix}_e^T d\tau = \int_{\Omega_e} \begin{bmatrix} \zeta_1 & 0 \\ 0 & \zeta_1 \\ \zeta_2 & 0 \\ 0 & \zeta_2 \end{bmatrix}_e \cdot \begin{bmatrix} \dfrac{\partial \zeta_1}{\partial x} & 0 \\ 0 & \dfrac{\partial \zeta_1}{\partial x} \\ \dfrac{\partial \zeta_2}{\partial x} & 0 \\ 0 & \dfrac{\partial \zeta_2}{\partial x} \end{bmatrix}_e^T d\tau$$
$$= \int_{\Omega_e} \begin{bmatrix} \zeta_1 \dfrac{\partial \zeta_1}{\partial x} & 0 & \zeta_1 \dfrac{\partial \zeta_2}{\partial x} & 0 \\ 0 & \zeta_1 \dfrac{\partial \zeta_1}{\partial x} & 0 & \zeta_1 \dfrac{\partial \zeta_2}{\partial x} \\ \zeta_2 \dfrac{\partial \zeta_1}{\partial x} & 0 & \zeta_2 \dfrac{\partial \zeta_2}{\partial x} & 0 \\ 0 & \zeta_2 \dfrac{\partial \zeta_1}{\partial x} & 0 & \zeta_2 \dfrac{\partial \zeta_2}{\partial x} \end{bmatrix}_e d\tau = \frac{1}{2} \cdot \begin{bmatrix} -1 & 0 & 1 & 0 \\ 0 & -1 & 0 & 1 \\ -1 & 0 & 1 & 0 \\ 0 & -1 & 0 & 1 \end{bmatrix}_e \tag{2.3.16}$$

The global assembly required in (2.3.14) is demonstrated in (2.3.17) and (2.3.18). The integrated element matrices contain zero entries at off-element locations.

$$Q = \sum_{\mu=1}^{N_e} Q_e = \begin{bmatrix} \tilde{\zeta}_1 \vec{q}_1 \\ \tilde{\zeta}_2 \vec{q}_2 \\ 0 \\ \vdots \end{bmatrix}_{N_e \times 1} + \begin{bmatrix} 0 \\ \tilde{\zeta}_1 \vec{q}_2 \\ \tilde{\zeta}_2 \vec{q}_3 \\ 0 \end{bmatrix}_{N_e \times 1} + \cdots + \begin{bmatrix} \vdots \\ 0 \\ \tilde{\zeta}_1 \vec{q}_{N_e-1} \\ \tilde{\zeta}_2 \vec{q}_{N_e} \end{bmatrix}_{N_e \times 1} \tag{2.3.17}$$

$$GWS^N = \sum_{\mu=1}^{N_e} \left( \frac{1}{6} \cdot \begin{bmatrix} 2 & 0 & 1 & 0 \\ 0 & 2 & 0 & 1 \\ 1 & 0 & 2 & 0 \\ 0 & 1 & 0 & 2 \end{bmatrix}_e \cdot \frac{\partial Q_e}{\partial t} + \overline{\overline{C}}_e \cdot \frac{1}{2} \cdot \begin{bmatrix} -1 & 0 & 1 & 0 \\ 0 & -1 & 0 & 1 \\ -1 & 0 & 1 & 0 \\ 0 & -1 & 0 & 1 \end{bmatrix}_e \cdot Q_e \right) =$$

$$= \left( \frac{1}{6} \cdot \begin{bmatrix} 2 & 0 & 1 & 0 \\ 0 & 2 & 0 & 1 \\ 1 & 0 & 2 & 0 \\ 0 & 1 & 0 & 2 \end{bmatrix}_{e=1} \cdot \frac{\partial}{\partial t} \begin{bmatrix} \vec{q}_1 \\ \vec{q}_2 \\ 0 \\ \vdots \end{bmatrix}_{N_e \times 1} + \overline{\overline{C}}_e \cdot \frac{1}{2} \cdot \begin{bmatrix} -1 & 0 & 1 & 0 \\ 0 & -1 & 0 & 1 \\ -1 & 0 & 1 & 0 \\ 0 & -1 & 0 & 1 \end{bmatrix}_{e=1} \cdot \begin{bmatrix} \vec{q}_1 \\ \vec{q}_2 \\ 0 \\ \vdots \end{bmatrix}_{N_e \times 1} \right) + \cdots$$

$$+ \left( \frac{1}{6} \cdot \begin{bmatrix} 2 & 0 & 1 & 0 \\ 0 & 2 & 0 & 1 \\ 1 & 0 & 2 & 0 \\ 0 & 1 & 0 & 2 \end{bmatrix}_{e=N_e} \cdot \frac{\partial}{\partial t} \begin{bmatrix} \vdots \\ 0 \\ \vec{q}_{N_e-1} \\ \vec{q}_{N_e} \end{bmatrix}_{N_e \times 1} + \overline{\overline{C}}_e \cdot \frac{1}{2} \cdot \begin{bmatrix} -1 & 0 & 1 & 0 \\ 0 & -1 & 0 & 1 \\ -1 & 0 & 1 & 0 \\ 0 & -1 & 0 & 1 \end{bmatrix}_{e=N_e} \cdot \begin{bmatrix} \vdots \\ 0 \\ \vec{q}_{N_e-1} \\ \vec{q}_{N_e} \end{bmatrix}_{N_e \times 1} \right)$$

$$\Rightarrow GWS^N = [A200L]_A \cdot \frac{\partial Q}{\partial t} + \overline{\overline{C}}_A \cdot [A201L]_A \cdot Q = \vec{0} \tag{2.3.18}$$

The coupled unsteady mass and momentum balances in 1D, (2.3.1) and (2.3.2), have been reduced to a set of linearly dependent ODE's in time using a linear spatial discretization. The substitutions indicated in (2.3.19) generate a theta implicit Newton statement amenable to algebraic time stepping where RES and MASS are defined as in (2.3.20).

$$\begin{aligned} GWS^N &= [MASS]_A \cdot \frac{\partial Q}{\partial t} + [RES] = 0 \\ \Rightarrow Q_n' &= -\frac{[RES]_n}{[MASS]_A} \end{aligned} \tag{2.3.19}$$

$$
\begin{aligned}
&Q_{n+1} = Q_n + \Delta t \cdot \left(\theta \cdot Q'_{n+1} + (1-\theta) \cdot Q'_n\right) + O\left(\Delta t^{f(\theta)}\right) \\
&= Q_n + \Delta t \cdot \left(\theta \cdot \left(-\frac{[RES]_{n+1}}{[MASS]_A}\right) + (1-\theta) \cdot \left(-\frac{[RES]_n}{[MASS]_A}\right)\right) + O\left(\Delta t^{f(\theta)}\right) \\
&\Rightarrow [MASS]_A \cdot (Q_{n+1} - Q_n) + \Delta t \cdot \theta \cdot [RES]_{n+1} - \Delta t \cdot \theta \cdot [RES]_n = -\Delta t \cdot [RES]_n \\
&\Rightarrow [MASS]_A \cdot (Q_{n+1} - Q_n) + \Delta t \cdot \theta \cdot \left(\overline{\overline{C}} \cdot [A201]_A \cdot Q_{n+1}\right) - \Delta t \cdot \theta \cdot \left(\overline{\overline{C}} \cdot [A201]_A \cdot Q_n\right) = -\Delta t \cdot [RES]_n \\
&\Rightarrow \left([MASS]_A + \Delta t \cdot \theta \cdot \overline{\overline{C}} \cdot [A201]_A\right) \cdot \Delta Q = -\Delta t \cdot [RES]_n \\
&[JAC] \cdot \Delta Q = -\Delta t \cdot [RES]_n \\
&\Rightarrow Q_{n+1} = Q_n - \Delta t \cdot [JAC]^{-1} \cdot [RES]_n
\end{aligned}
\tag{2.3.20}
$$

The solution algorithm is summarized below in Figure 2.3.3 and the MatLab implementation is given in Appendix B. The water hammer analogy provides a validation exercise for this algorithm as well as demonstrating the benefit of increasing the compressibility of the mercury target. As mentioned before a 20MPa pressure increase is expected to result from a 1MW target power. Using the analogy of a sudden valve closure, the flow velocity associated with a 20 MPa pressure change, a mercury density of $\rho = 13{,}500\,kg/m^3$ and sound speed $c = 1{,}500\,m/s$ is $v_0 = 1\,m/s$. The initial step velocity profile in the mercury duct is given in Figure 2.3.4 while the initial pressure distribution is a constant $P(x, t=0) = 1\times 10^5\,Pa$. At an instant t=0s the valve is closed and the flow velocity is reduced to $v_0 \cong 0\,m/s$; this information is propagated to the left along the duct at the speed of sound. The pressure and velocity distribution is given in Figures 2.3.5 and 2.3.6 for various times. The pressure change associated with the flow

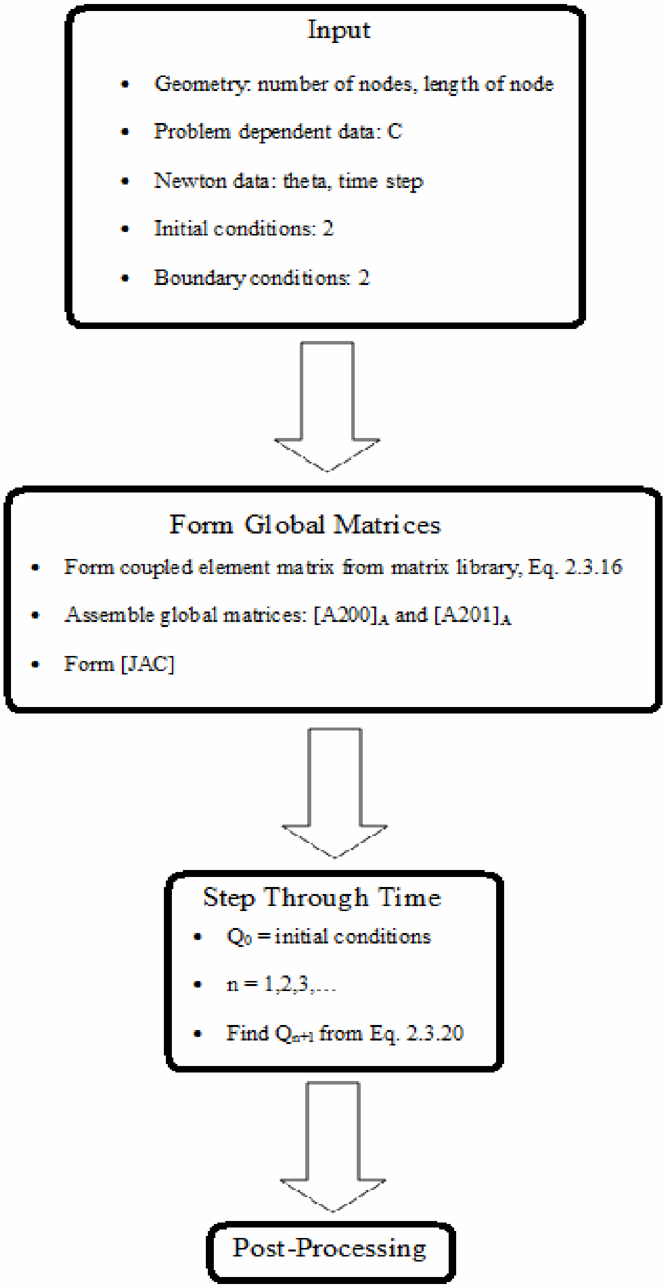


Figure 2.3.3: Flow chart describing the finite element solution of a 1D inviscid flow.

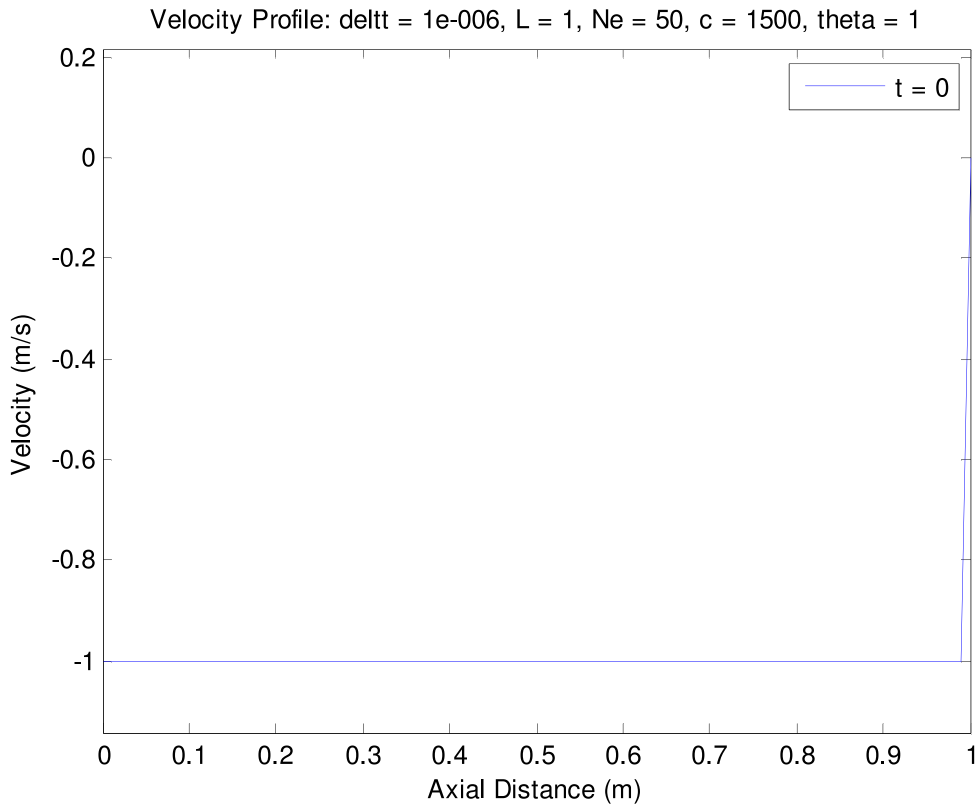


Figure 2.3.4: Initial axial velocity distribution.

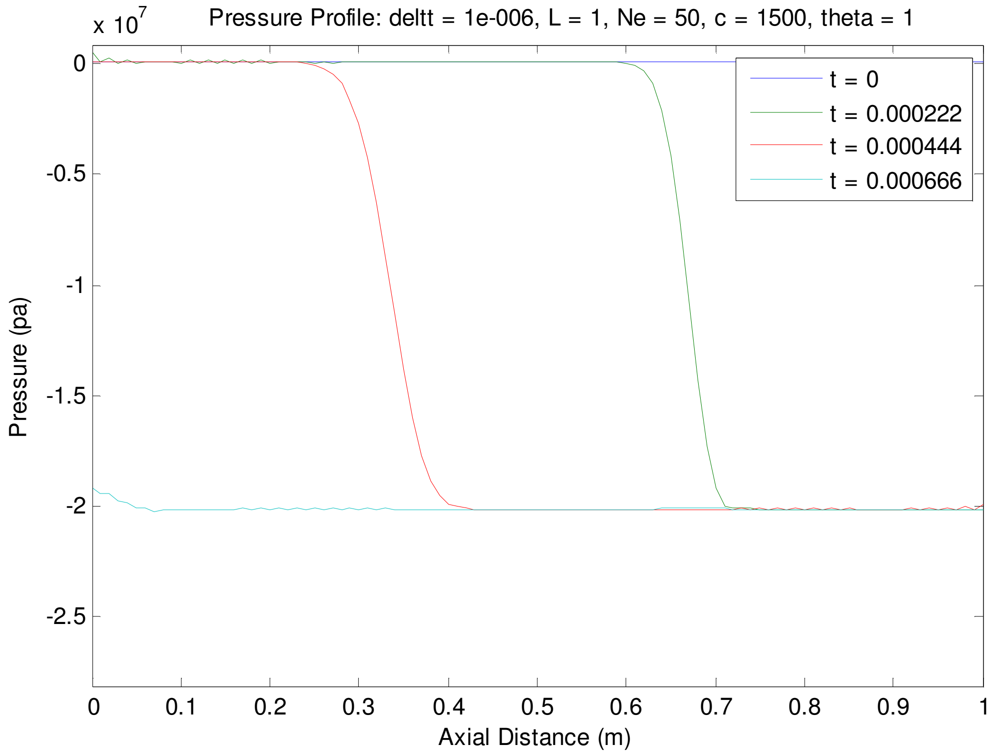


Figure 2.3.5: Axial pressure distribution for the mercury solid case plotted at several times.

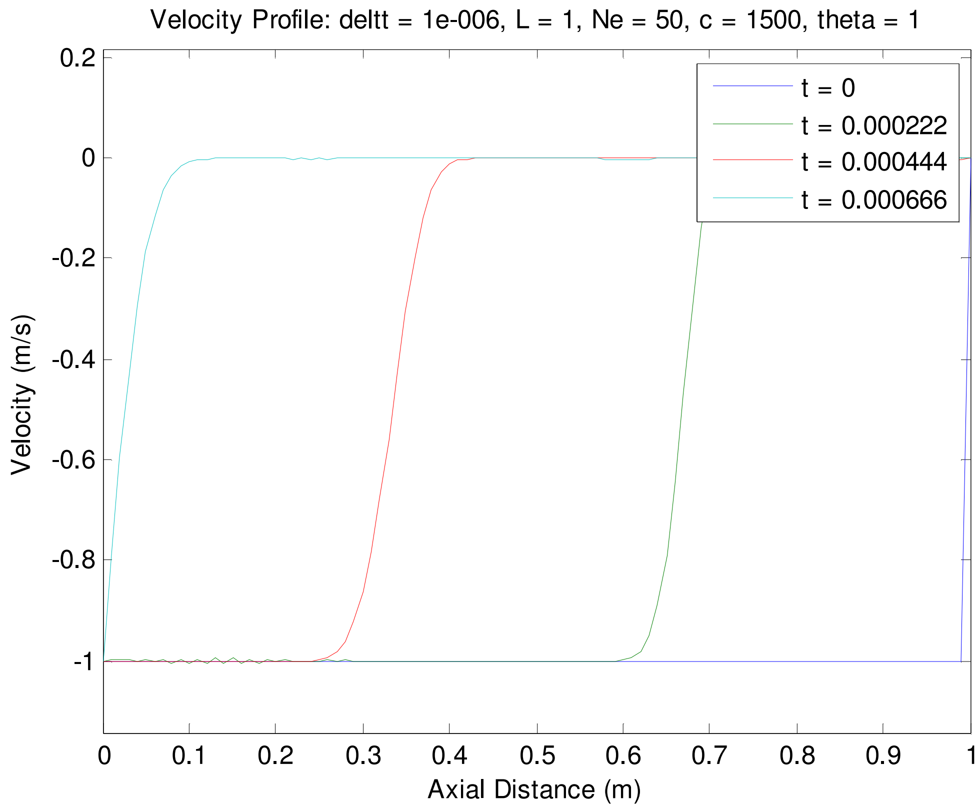


Figure 2.3.6: Axial velocity distribution for the mercury solid case plotted at several times.

stoppage is verified. It should be mentioned that this solution is a result of a fully implicit (theta = 1) algorithm using quadratic interpolation polynomials. The step velocity change at the valve face is propagated smoothly because of the artificial diffusion and the rate at which the solution is smoothed in time is amplified through the use of the higher order interpolation polynomials. Figure 2.3.7 is the pressure distribution found using linear interpolation polynomials; the rate at which the solution is smoothed through artificial diffusion is substantially less than the case of quadratic interpolation polynomials.

A similar exercise demonstrates the utility of adding compressibility to the target in the form of small helium bubbles. The sound speed is a strong function of void fraction and a representative sound speed of $c = 150\, m/s$ in a bubbly mixture is used for this exercise. [11] With all other algorithm parameters kept the same, pressure and velocity distributions are plotted for several times in Figures 2.3.8 and 2.3.9. The pressure increase associated with the flow stoppage is an order of magnitude less than the case of $c = 1{,}500\, m/s$ as expected from Eq. 2.3.1. Pressure changes within the mercury loop due to area changes in the piping system lead to void fraction variations ranging from 0.5% to 2%; this variation in void fraction leads to sound speed variations of 30-150 m/s. [30]

An iterative Newton method is outlined in anticipation of non-linear applications such as viscous flow.. An approximation to the GWS is defined in (2.3.21). The iterative change in Q is defined via matrix differentiation in (2.3.22). The (p+1) approximation to $Q_{n+1}$ is given in (2.3.23).

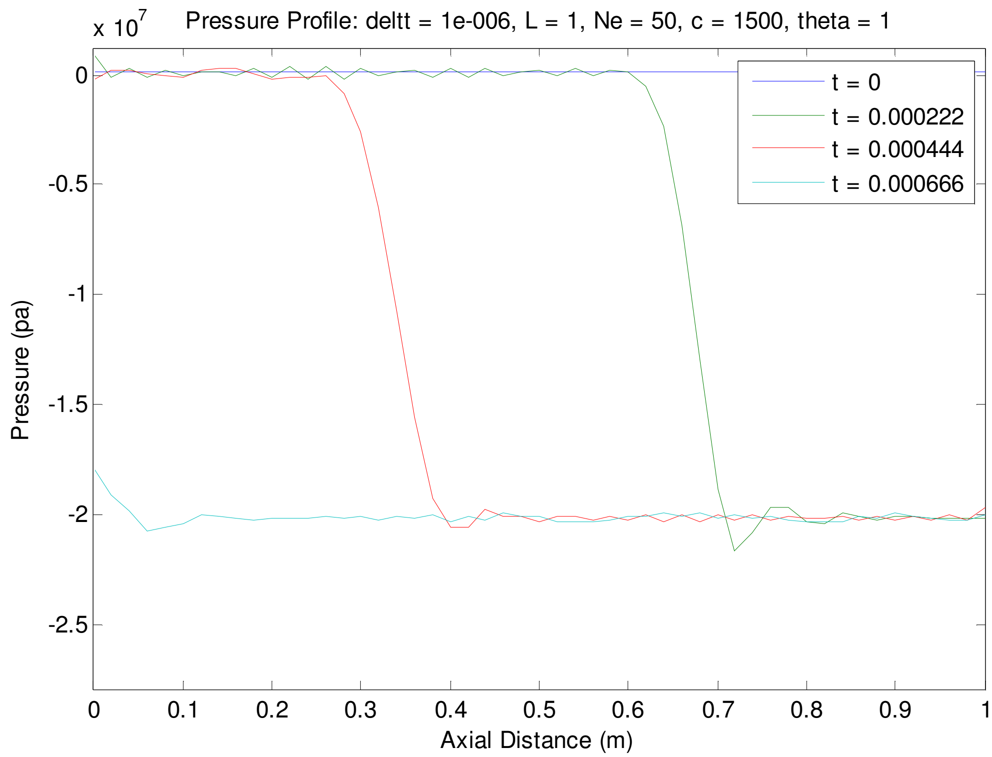


Figure 2.3.7: Axial pressure distribution for the mercury solid case plotted at several times calculated using linear interpolation polynomials.

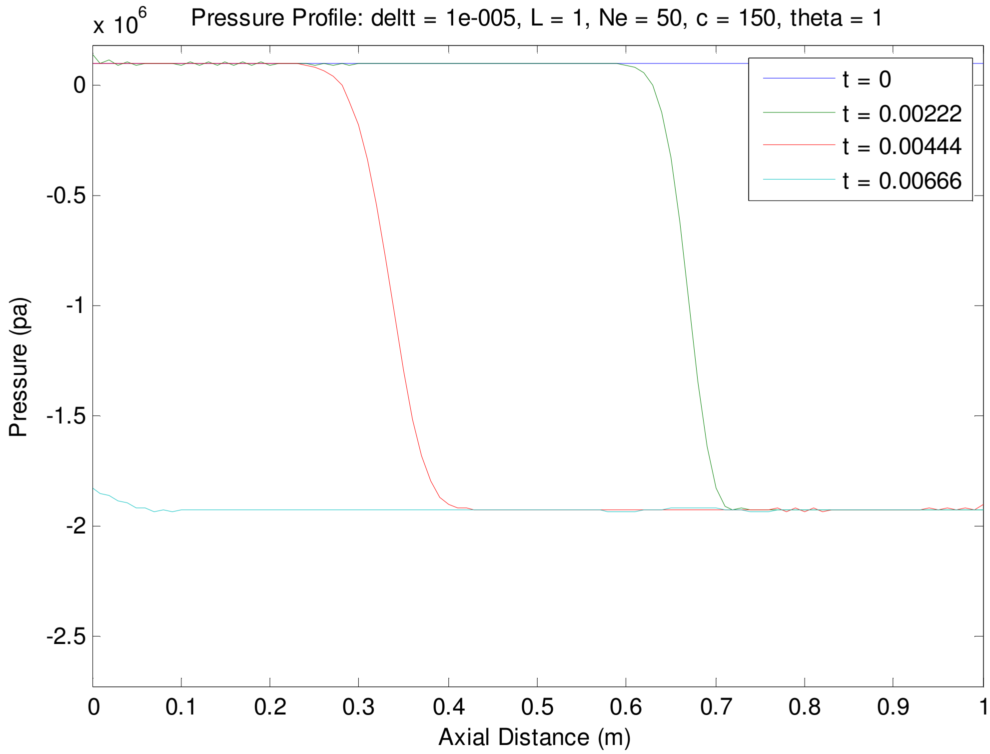


Figure 2.3.8: Axial pressure distribution for the mercury/bubbly mixture case plotted at several times.

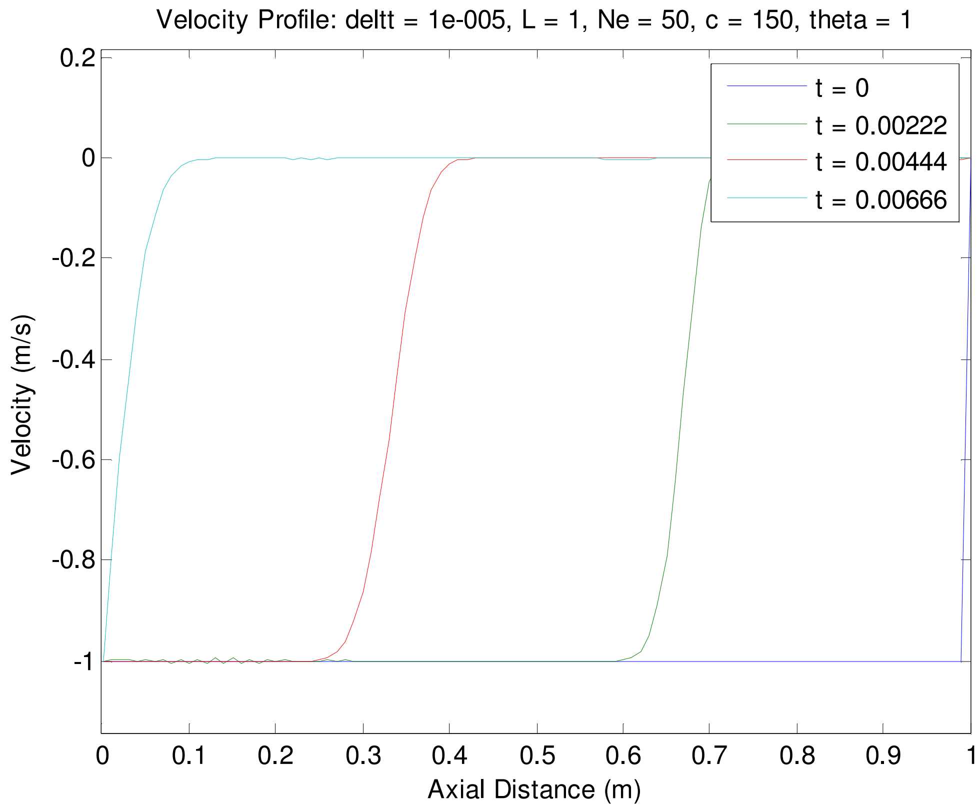


Figure 2.3.9: Axial velocity distribution for the mercury/bubbly mixture case plotted at several times.

$$\left[FQ\right]^{p} = \left[MASS\right]_{A} \cdot \Delta Q^{p} + \Delta t\left(\theta \cdot \left[RES\right]_{n+1}^{p} + \left(1-\theta\right) \cdot \left[RES\right]_{n}\right) \tag{2.3.21}$$

$$\left[RES\right]_{n+1}^{p} = \left(\overline{\overline{C}} \cdot \left[A201\right]_{A}\right) \cdot Q_{n+1}^{p}$$

$$\Delta Q^{p+1} = -\left[JAC\right]^{-1} \cdot \left[FQ\right]^{p} \tag{2.3.22}$$

$$\left[JAC\right] = \frac{\partial FQ}{\partial \vec{q}} = \begin{bmatrix} FQ(P) \\ FQ(v) \end{bmatrix} \begin{bmatrix} \partial/\partial P & \partial/\partial v \end{bmatrix} = \begin{bmatrix} \dfrac{\partial FQ}{\partial P} & \dfrac{\partial FQ}{\partial v} \\ \dfrac{\partial FQ}{\partial P} & \dfrac{\partial FQ}{\partial v} \end{bmatrix} = \begin{bmatrix} \left[MASS\right]_{A} & \Delta t \cdot \theta \cdot \overline{\overline{C}} \cdot \left[A201\right]_{A} \\ \Delta t \cdot \theta \cdot \overline{\overline{C}} \cdot \left[A201\right]_{A} & \left[MASS\right]_{A} \end{bmatrix}$$

$$Q_{n+1}^{p+1} = Q_{n+1}^{p} + \Delta Q^{p+1} \tag{2.3.23}$$

# 3 MICROBUBBLE GENERATION

## 3.1 SWIRLING JET BUBBLERS

Several researchers have presented microbubble generators based on injecting gas into a turbulent flow. [15,16, 28,29] A swirling jet bubbler is a candidate device to accomplish a suitable bubble population in the SNS target. Co-axial swirl jet bubble production devices, such as the commercially available device from the Nitta-Moore corporation, induce a high rate of rotation in a liquid flow, sometimes achieving over 1000 revolutions per second, and inject gas into the center of this flow to form a gas filament. The swirling liquid flow and gas filament are then injected into a larger volume of liquid to form a swirling liquid jet. The gas filament diverges to the outer jet perimeter when the swirling jet enters the larger liquid volume due to the rapid liquid deceleration and associated adverse pressure gradient. The gas filament is broken into small bubbles in the high shear region where the swirling jet meets the more quiescent fluid in the larger liquid volume. An Olympus I-speed video imaging system is used to examine the bubble formation in this high shear region for a water-helium system. Models are developed from this data and used to develop scale parameters for the bubble generation physics. These are used to scale the device geometry, flow, pressure loss and bubble production diameter using water-helium data.

## 3.2 SWIRLING JET BREAKUP DESCRIPTION

The physics of the Nitta-Moore device is described in terms of the three distinct regions pictured in Figure 3.2.1. Region (A) introduces an axisymmetric swirl to the

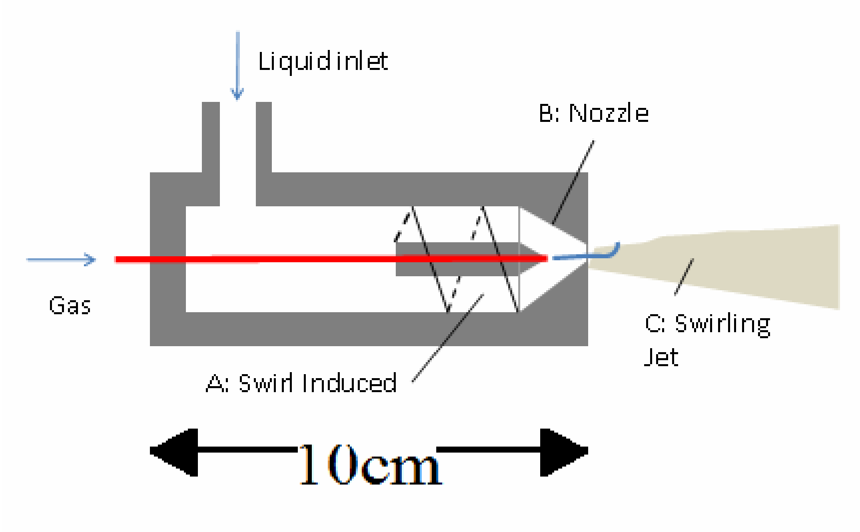


Figure 3.2.1: Schematic of Nitta-Moore Cross-Section.

liquid. In region (B) the gas is injected along the low pressure centerline, and the swirling flow is accelerated through a nozzle. The flow enters a plenum in Region (C), creating a swirling jet. Flow instabilities at the gas/liquid interface within region (B) and interaction of the gas with a strong shear layer in region (C) are both suggested here as possible breakup mechanisms which fit this physical description. High-speed video of the flow at the nozzle exit indicates the radial pressure gradient confines the gas jet to the flow centerline in region (B). As the jet exits the nozzle into region (C) the axial pressure gradient is reversed and the gas jet follows the steepest decent of the pressure gradient into the high shear region where the rotating jet meets the relatively quiescent fluid in the plenum. The small bubbles are produced where the gas filament intersects this region of high shear.

The gas filament rotates with the liquid jet as it diverts to the jet surface, and breaks into small bubbles in an annulus located a few exit orifice diameters downstream. The free shear layer formed where the jet meets the quiescent fluid in the plenum causes breakup of the gas filament; an embedded video of the gas filament breakup is provided, 2.2L_min.avi .

## 3.3 Characterization of the Forces which Lead to Droplet Deformation

Understanding the breakup of the gas filament within the turbulent shear layer begins by characterizing the forces which lead to droplet deformation. An immiscible fluid forming a globule within a continuous fluid phase is shown in Figure 3.3.1. The

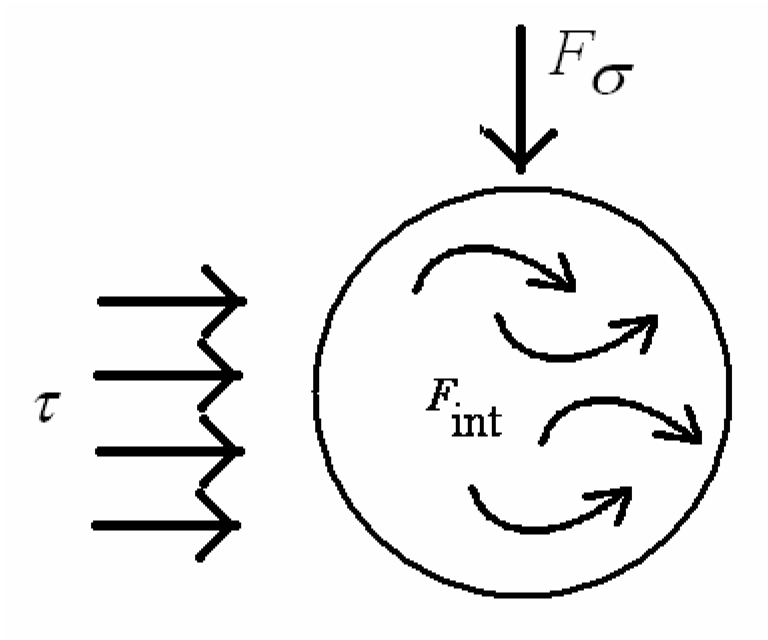


Figure 3.3.1: Forces acting on an immiscible globule.

splitting of this droplet is characterized by the relative hydrodynamic forces acting on the droplet. The external forces acting on the surface of the droplet due to the fluid shear and fluid inertia cause a deformation; this force can arise from viscous stress and dynamic pressure within the continuous phase; typically the external force per unit area is given the symbol, $\tau$. Internal flows within the droplet due to the deformation or relative velocities at the interface cause viscous shear stresses and dynamic pressures which further deform the droplet. Hinze argues that the internal velocities are on the order of magnitude of $\frac{\mu_d}{D_d}\sqrt{\frac{\tau}{\rho_d}}$ where $\mu_d$ is the globule viscosity, $\rho_d$ is the globule density, and $D_d$ is the globule diameter. [12] The deformation of the droplet is counteracted by an interfacial surface tension force which is expressed as the pressure defect of a spherical droplet, $\frac{\sigma}{D_d}$. Further, Hinze develops dimensionless groups which characterize the relative importance of these three forces; these are expressed as equations 3.3.1 and 3.3.2.

$$N_{We} = \frac{\tau D_d}{\sigma} \qquad (3.3.1)$$

$$N_{Vi} = \frac{\mu_d}{\sqrt{\rho_d \sigma D_d}} \qquad (3.3.2)$$

The first dimensionless group describes the ratio of the external forces to the surface tension forces as a generalized Weber number. This group is termed a generalized Weber number owing to the fact that external viscous stresses as well as external dynamic pressures are considered. A discussion of the shear forces and therefore

Weber numbers associated with water/helium and mercury/helium systems is presented in the following section. The second dimensionless group accounts for the viscosity within the droplet leading to internal flows and is therefore termed the viscosity group and is sometimes referred to as the Ohnesorge number. This viscosity group represents the ratio of viscous to internal inertia forces. Note that the Ohnesorge number contains only droplet properties and therefore does not represent a simple force ratio. For a helium bubble with radius of 30 micrometers the viscosity group takes on a value of $N_{Vi} = \mathrm{O}\left(10^{-4}\right) << 1$; therefore for a helium/Hg system, surface tension forces are more significant than internal viscous effects.

The greater the external forces compared to the restoring force associated with surface tension the greater the droplet deformation. At a critical Weber number value droplet breakup occurs. In general the critical Weber number is a function of both the generalized Weber number and the Ohnesorge number. [12] This can be expressed using the simple relationship

$$\left(N_{We}\right)_{crit} = C \cdot \left[1 + \varphi\left(N_{Vi}\right)\right] \tag{3.3.3}$$

where C is a constant representing $\left(N_{We}\right)_{crit}$ when internal viscous effects can be ignored meaning φ decreases to zero as $N_{Vi}$ approaches zero. Using this relationship it can be seen that C and φ both depend on the external flow conditions which give rise to the external stress, τ.

## 3.4 Drop Breakup in Turbulent Flow

In the previous section it was shown that because the viscosity group of a helium bubbles takes on a value much less than one the critical Weber number takes the form

$$\left(N_{We}\right)_{crit} = \frac{\tau D_{\max}}{\sigma} = Const$$

An appropriate definition of the shear force associated with the continuous phase provides a definition for the maximum bubble diameter in a turbulent flow. If the shear force is associated with the kinetic energy of the continuous phase a specific critical Weber number is defined by

$$\left(N_{We}\right)_{crit} = \frac{\rho_l v_l^2 D_{\max}}{\sigma} = Const \tag{3.4.1}$$

This approach is employed by the transient thermal hydraulic code, RELAP5-3D, developed by DOE for the NRC. The critical Weber number in RELAP5-3D is taken as $\left(N_{We}\right)_{crit} = 10$ for steam and water [13]. One can derive identical results if the dynamic pressure of the liquid flow is thought to balance the pressure defect of the bubble. Employing the critical Weber number used in RELAP5-3D and rearranging (3.4.1) gives an expression for the maximum droplet diameter

$$D_{\max} = \frac{10 \cdot \sigma}{\rho_l v_l^2} \tag{3.4.2}$$

The use of a critical Weber number of 10 is not established in the literature for a helium/mercury system and has only been validated for a few cases when liquid is the continuous phase as cited in the RELAP5-3D manual.

Hinze argues that at high Reynolds numbers the droplet deformation in highly turbulent flows is less dependent on viscous shearing action of the droplet than the dynamic pressure forces associated with turbulent motion on the scale of the maximum droplet diameter. The external force can be represented by the dynamic pressure

$$\tau = \rho_l \overline{v^2} \tag{3.4.2}$$

where $\overline{v^2}$ is the average value across the whole flow field of the squares of the velocity differences associated with a distance equal to the maximum droplet diameter. Therefore the generalized Weber number for a highly turbulent flow is given by

$$N_{We} = \frac{\rho_l \overline{v^2} D_{\max}}{\sigma} \tag{3.4.3}$$

In the case of isotropic homogeneous turbulence the main contribution to the kinetic energy is made by fluctuations where the Kolmogorov energy distribution law is valid. In this region the turbulent structure is entirely determined by the energy input per unit mass and time, the so called energy dissipation rate, ε. Batchelor [14] shows that the mean squared velocity in this region of the energy spectrum is represented by

$$\overline{v^2} = C_1 (\varepsilon D)^{2/3} \tag{3.4.4}$$

where, according to Batchelor, $C_1$ takes on a value of 2.0. Assuming that the viscosity group is negligible one finds from the definition of the critical Weber number that

$$(N_{We})_{crit} = \frac{\rho_l C_1 (\varepsilon D_{\max})^{2/3} D_{\max}}{\sigma} = const. \tag{3.4.5}$$

or

$$D_{\max} \propto \left(\frac{\sigma}{\rho_l}\right)^{3/5} \cdot \varepsilon^{-2/5} \qquad (3.4.6)$$

Several authors report values of the constant of proportionality based on various geometries. Clay [15] reports a value of 0.725 for concentric rotating cylinders while Martinez-Bazan [16] reports a value of 1.26 for a free jet.

## 3.5 Droplet Diameter in Turbulent Pipe Flow

Consider the fully developed flow in a section of circular duct pictured in Figure 3.5.1. The turbulent energy dissipation rate for the flow system is approximated by the pressure drop across the duct length, $\Delta P$, the volumetric flow rate, $\dot{V}$, and the total mass of the system, $m_{system}$, as

$$\varepsilon \cong \frac{\dot{V} \cdot \Delta P}{m_{system}} \qquad (3.5.1)$$

Traditional engineering models may be adopted to approximate the pressure drop associated with wall shear such that

$$\Delta P = \frac{1}{2} \rho v_l^2 \left( f \frac{L}{D_{pipe}} \right) \qquad (3.5.2)$$

where $v_l$ is the flow velocity, L is the pipe length and f is the friction factor which has the following function form

$$f = 0.316(\mathrm{Re})^{-1/4} \qquad (3.5.3)$$

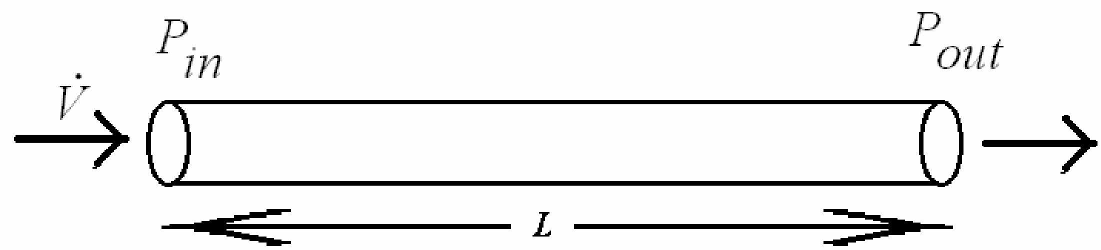


Figure 3.5.1: Schematic of pipe flow generating an energy dissipation term.

And

$$\mathrm{Re} = \frac{v_l D_{pipe}}{\nu_l} \tag{3.5.4}$$

with $\mathrm{Re} < 3 \times 10^4$ [17] being the Reynolds number associated with the bulk pipe flow in a smooth pipe. The maximum bubble diameter in a turbulent pipe flow may be found by combining (3.4.6) and (3.5.1)-(3.5.3) so that

$$D_{\max} = \tilde{C} \cdot \left(\frac{\sigma}{\rho}\right)^{3/5} \cdot D_{pipe}^{1/2} \cdot v_l^{-1/10} \cdot \nu_l^{-11/10} \tag{3.5.5}$$

where $\tilde{C}_{mixer} = 1.5$ , for the reported mixer model presented by Clay, and $\tilde{C}_{jet} = 2.6$, for the reported free jet model presented by Martinez-Bazan. These models are compared in Figure 3.5.2 for a helium/water system and Figure 3.5.3 for a helium/ mercury system with pipe diameter of 10cm and fluid properties as listed in Appendix A.

For higher Reynolds numbers in the $3 \times 10^4 < \mathrm{Re} < 1 \times 10^6$ range, the McAdams relation for the pipe friction factor is more appropriate

$$f = 0.184(\mathrm{Re})^{-1/5}$$

And the maximum diameter is found as

$$D_{\max} = \tilde{C} \cdot \left(\frac{\sigma}{\rho}\right)^{3/5} \cdot D_{pipe}^{12/5} \cdot v_l^{-2/25} \cdot \nu_l^{-28/25}$$

where $\tilde{C}_{mixer} = 0.067$ , for the reported mixer model presented by Clay, and $\tilde{C}_{jet} = 0.116$, for the reported free jet model presented by Martinez-Bazan. These models are compared RELAP5 models in Figure 3.5.4 for a helium/water system and Figure 3.5.5 for a helium/mercury system with pipe diameter of 10cm and fluid properties as listed in Appendix A.

## 3.6 Droplet Diameter in a Turbulent Round Jet

Returning to the physics of the swirling jet bubbler, we recognize that the energy dissipation rate is related to the turbulent viscosity. Therefore, in order to accomplish closed form scale models, an axisymmetric jet model is adopted which defines a turbulent viscosity using an outer wake model as [18]

$$\nu_t = 0.016 \cdot U_0 \cdot b_0 \tag{3.6.1}$$

Where $U_0$ defines the liquid velocity and $b_0$ is the jet width at a reference axial distance, $x_0$. The similarity variable assumes isotropic turbulence.

The energy dissipation per unit mass, $\varepsilon$, is found from the definition of a turbulent

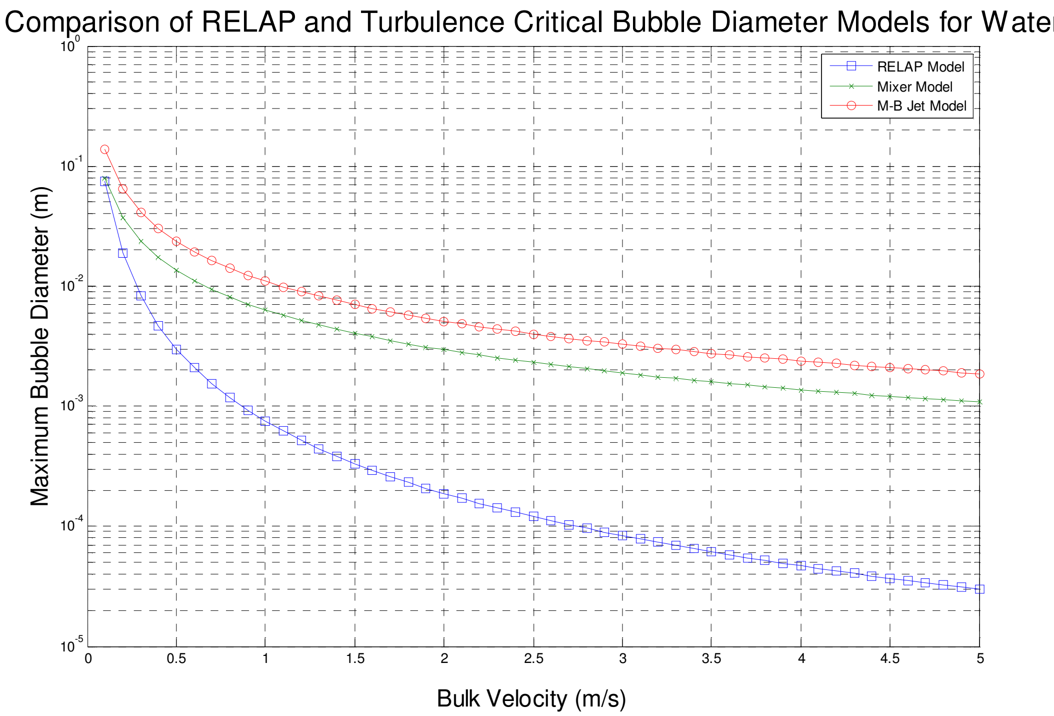


Figure 3.5.2: Comparison of critical Weber number models for helium/water system.

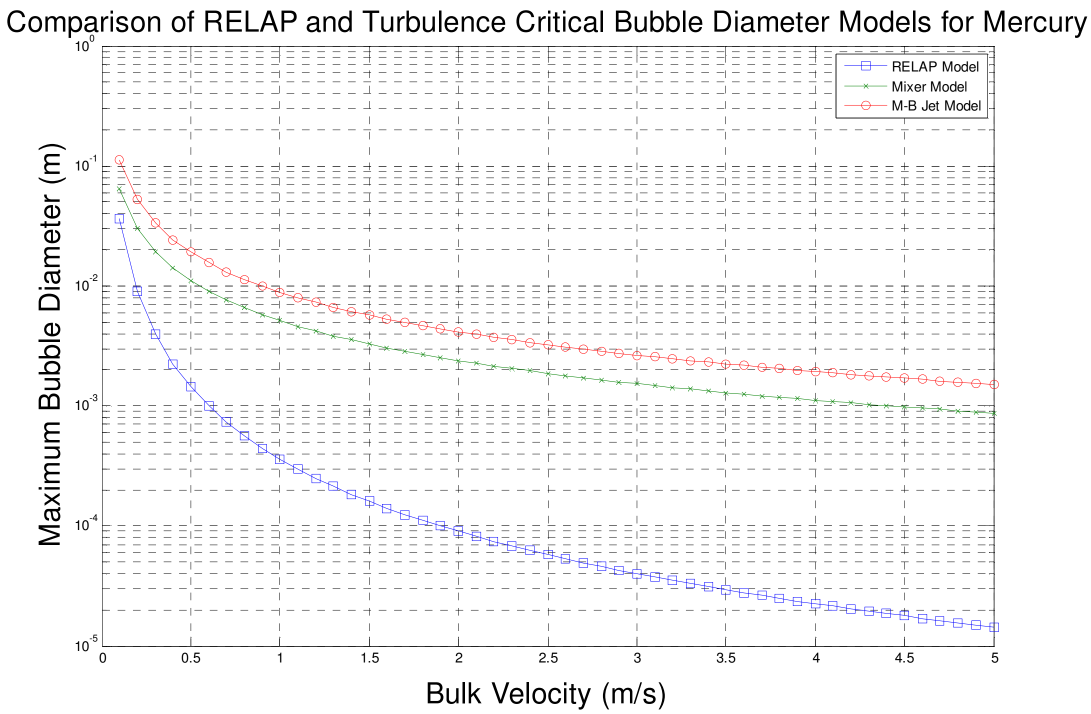


Figure 3.5.3: Comparison of critical Weber number models for helium/mercury system.

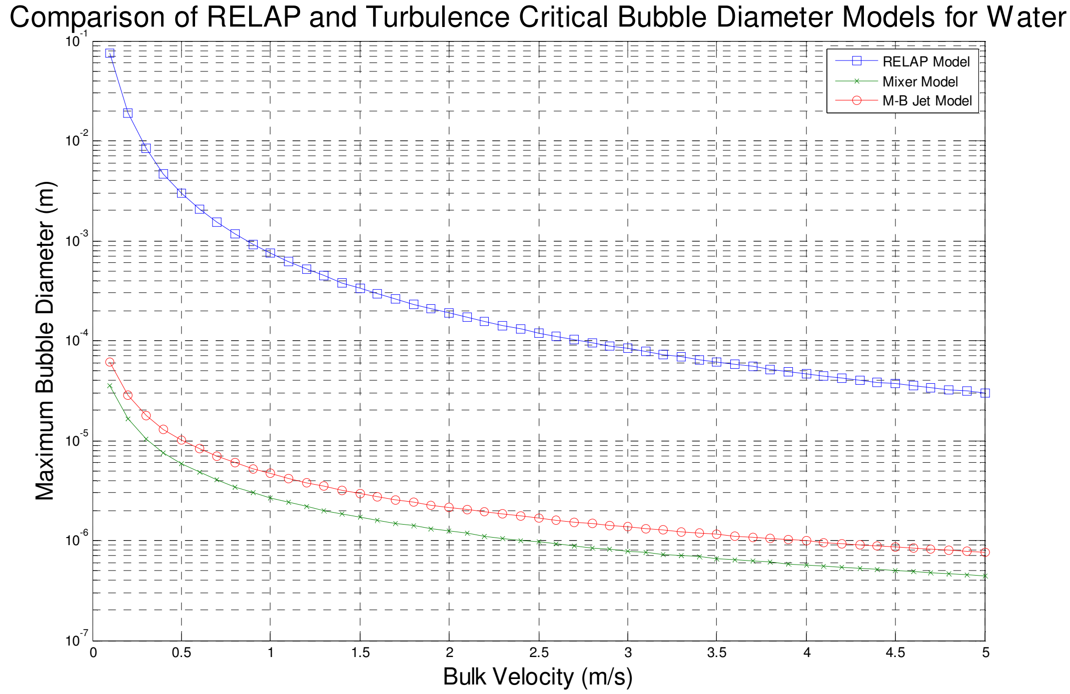


Figure 3.5.4: Comparison of critical Weber number models for helium/water system.

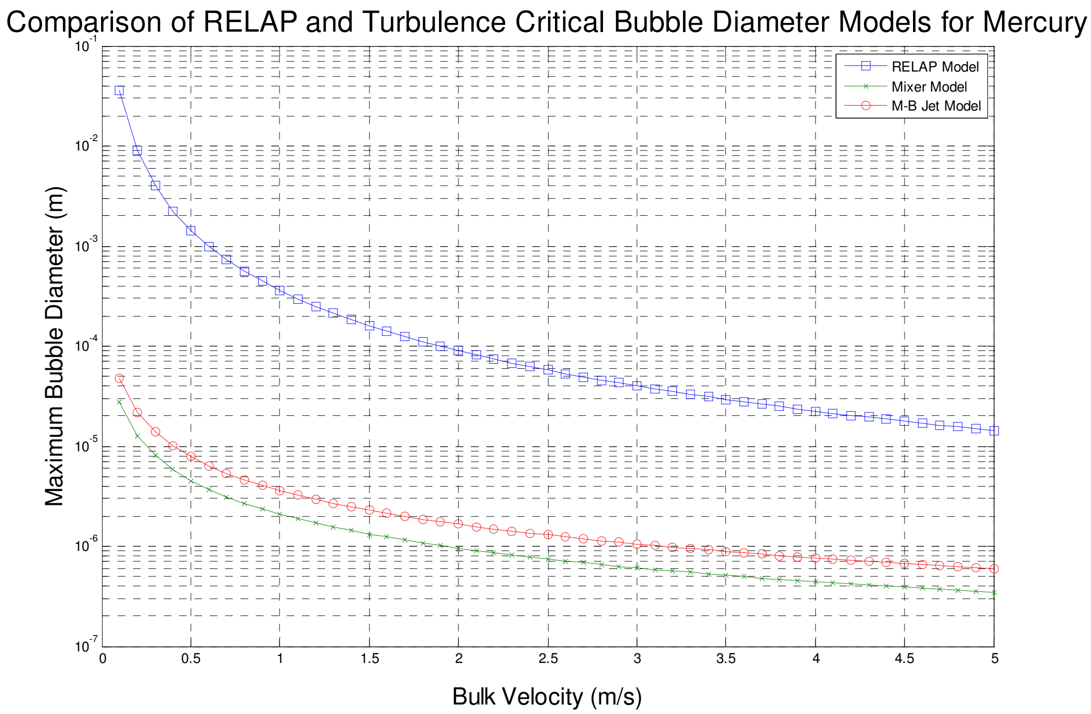


Figure 3.5.5: Comparison of critical Weber number models for helium/mercury system.

viscosity and the assumption that the strain-rate, $S_{ij}$, only varies with swirl,

$$\tau_{ij} = 2\nu_t S_{ij} \Rightarrow \varepsilon = \frac{2 \cdot S_{ij}}{l^2}\nu_t = f(\varpi)\cdot \nu_t \tag{3.6.2}$$

such that the strain rate, $S_{ij}$, is defined as

$$S_{ij} = \tfrac{1}{2} \cdot l^2 \cdot f(\varpi) \tag{3.6.3}$$

Combination of (3.4.6), (3.6.1) and (3.6.2) defines a critical bubble diameter for a swirling jet,

$$D_{\max} = C_2 \cdot \left(\frac{\sigma}{\rho}\right)^{3/5} \cdot \left(f(\varpi)\cdot U_0 \cdot b_0\right)^{-2/5} \tag{3.6.4}$$

where the constant of proportionality is chosen as $C_2 = 3.79$ or $C_2 = 6.59$ corresponding to a rotating cylindrical geometry or free jet geometry respectively.

## 3.7 Functional Analysis

Functional analysis of the flow variables assists in scaling from water to mercury systems. The variables pertinent to the jet characteristics are average bubble diameter, $d_{bub}$, nozzle diameter at the exit, $D_{nozzle}$, liquid and gas volumetric flow rates, $\dot{V}_{liq}$ and $\dot{V}_{gas}$, jet angular frequency, $\omega_{exit}$, liquid density, $\rho_{liq}$, viscosity, $\nu_{liq}$, and surface tension, $\sigma_{liq}$. The literature indicates that the gas flow rate has a minimal effect on average bubble size [19] and is not considered in this work. However, there is a threshold at which the gas travels through the jet with sufficient velocity to avoid complete breakup during interaction with the turbulent structure therefore increasing the average bubble diameter. Consideration of the pertinent variables leads to the functional form for the average bubble diameter given as

$$d_{bub} = d_{bub}\left(D_{nozzle}, \dot{V}_{liq}, \omega_{exit}, \rho_{liq}, \nu_{liq}, \sigma_{liq}\right) \tag{3.7.1}$$

Define the nozzle diameter, liquid flow rate, and liquid density as primary variables according to

$$\begin{aligned}
[Length] &\Leftrightarrow D_{nozzle} \\
[Time] &\Leftrightarrow D_{nozzle}^{3} \big/ \dot{V}_{liq} \\
[Mass] &\Leftrightarrow D_{nozzle}^{3} \cdot \rho_{liq}
\end{aligned} \tag{3.7.2}$$

Dimensional analysis of the remaining variables determines the equivalent form

$$\frac{d_{bub}}{D_{nozzle}} = f\left(\frac{\pi \cdot \omega_{exit} \cdot D_{nozzle}^{3}}{8 \cdot \dot{V}_{liq}}, \frac{\dot{V}_{liq}}{D_{nozzle} \cdot \upsilon_{liq}}, \frac{\rho_{liq} \cdot \dot{V}_{liq}^{2}}{D_{nozzle}^{3} \cdot \sigma_{liq}}\right) \Leftrightarrow We = f\left(\overline{\varpi}, \mathrm{Re}_{exit}\right) \tag{3.7.3}$$

With the average Weber number, *We*, non-dimensional swirl rate, $\overline{\varpi}$, and Reynolds number at the nozzle exit, $\mathrm{Re}_{exit}$, defined as

$$We \Leftrightarrow \frac{\rho_{liq} \cdot \dot{V}_{liq}^{2} \cdot d_{bub}}{D_{nozzle}^{4} \cdot \sigma_{liq}}$$

$$\overline{\varpi} \Leftrightarrow \frac{\pi \cdot \omega_{exit} \cdot D_{nozzle}^{3}}{8 \cdot \dot{V}_{liq}}$$

$$\mathrm{Re}_{exit} \Leftrightarrow \frac{\dot{V}_{liq}}{D_{nozzle} \cdot \nu_{liq}} \tag{3.7.4}$$

In a similar fashion, dimensional analysis of the pressure drop across the device and the radial pressure gradient within the nozzle generates relationships useful to engineering design. The fluted geometry fixes the angular frequency as a function of the device pitch and exit Reynolds number.

$$\Delta P_{loss} = f(\mathrm{Re}_{exit}) \tag{3.7.5}$$

$$\omega_{exit} = f(\mathrm{Re}_{exit}) \tag{3.7.6}$$

## 3.8 Scaling Critical Bubble Diameter

A power law, (3.8.1), is stated to represent the relationship in (3.7.3).

$$We = \beta \cdot \mathrm{Re}^{\alpha} \tag{3.8.1}$$

Expanding terms from the dimensionless groups given in (3.7.4) while adopting the power law representation of the relationship in (3.7.3) generates a functional relationship for the average bubble size

$$d_{bub} = \beta \cdot \left(\frac{\sigma}{\rho}\right) \cdot \left(\frac{\pi}{4}\right)^{\alpha} \cdot \left(\frac{D_{noz}^{\alpha}}{\nu_{liq}^{\alpha}}\right) \cdot U_0^{\ \alpha-2} \tag{3.8.2}$$

Comparing (3.6.4) and (3.8.2) implies $\alpha = 8/5$ and the form of β is offered by (3.8.3), where $h(\varpi)$ relates strain-rate, fluid properties and turbulence closure coefficients.

$$\beta = \left(\frac{D_{noz}}{\nu_{liq}}\right)^{-8/5} \cdot h(\varpi)^{-2/5} \tag{3.8.3}$$

A power law relationship is also presented for characterizing the measured performance of swirling jet bubblers by Tabei, 2007,

$$We = \beta \cdot \mathrm{Re}^{3/2} \tag{3.8.4}$$

with $\beta = \left(1.72 \times 10^{-6}\right) \cdot \varpi^{-3/2}$. The coefficients for these two models are dimensionless quantities relating swirl and fluid properties therefore, $\beta = \left(1.72 \times 10^{-6}\right) \cdot \varpi^{-3/2}$ will be taken for use in both models. It is interesting to note that the physics which supports (3.8.3) explicitly generates the coefficient of (3.8.4) for water as $\left(D_{noz}/\nu_{liq}\right)^{-8/5} = 1.72 \times 10^{-6}$. However, this physical interpretation is not provided by Tabei, 2007.

## 3.9 Experiment

The functional relationships presented in (3.7.3), (3.7.5) and (3.7.6) are compared to data found in a helium/water system using a commercial swirling jet device. Table 3.9.1 shows the range of values taken in (3.7.1) for this study. A loss coefficient for the device of $K_{loss} \cong 20$ is estimated from pressure loss and liquid flow rate measurements at the nozzle exit. Also, the direct correlation between swirl rate and device geometry is measured which establishes the relationship in (3.7.6). Finally, the power law exponent of $\alpha = 3/2$ from Tabei ,based on air/water data [19], and the power law exponent of

$\alpha = 8/5$ ,based on mechanistic scale arguments from this study, are compared to the bubble size distribution data. Although the quantitative difference of the two exponents is minor, the mechanistic outcome provides a higher confidence in extrapolation to other gas/fluid systems such as helium and mercury.

## 3.10 EXPERIMENTAL SETUP

The Nitta-Moore commercial swirling jet bubbler is pictured in Figure 3.10.1. Liquid is injected at Part (b) and gas is injected at Part (c), the liquid gas mixture exits Part (a). A cross-section of the device is presented in Figure 3.10.2 for clarification. For reference, the swirl and gas filament injection described as physics in Regions (A) and (B) occur in Part (a). The jet physics of Region (C) occurs in a liquid tank and is pictured in Figure 3.10.3; this observation tank is open to the atmosphere. The schematic of the test flow loop is given in Figure 3.10.4.

## 3.11 SCALING RESULTS

The viscous losses through the bubbler can be described using the one-dimensional steady incompressible energy equation in terms of the pressure losses, dynamic pressure, and loss coefficient, $K_{loss,}$ following the form,

$$K_{loss} = \frac{\Delta P_{loss}}{8 \cdot \pi^2 \cdot \rho_{liq} \cdot \dot{V}_{liq} \cdot D_{noz}^4} \qquad (3.11.1)$$

The liquid flow rate is measured using an Omega turbine meter with 0.3L/min accuracy in the 1-5L/min device operating range. The pressure drop across the device is measured using an upstream pressure gauge with 2 psi resolution in the 10-50 psi range. Gas flow

| Table 3.9.1: Range of Pertinent Variables | |
|---|---|
| Diameter of Exit orifice, $D_{nozzle}$ , (mm) | 4 |
| Liquid Flow Rate, $\dot{V}_{liq}$ , (L/min) | 2-4 |
| Angular Frequency, $\omega_{exit}$ ,(Rev/s) | 600-1300 |
| Liquid Density, $\rho_{liq}$ ,(Kg/m$^3$) | 1000 |
| Liquid Viscosity, $\nu_{liq}$ ,(m$^2$/s) | $1\times10^{-6}$ |
| Liquid Surface Tension, $\sigma_{liq}$ ,(N/m) | 0.075 |
| Average Bubble Diameter, $d_{bub}$ ,( $\mu m$ ) | 50-200 |

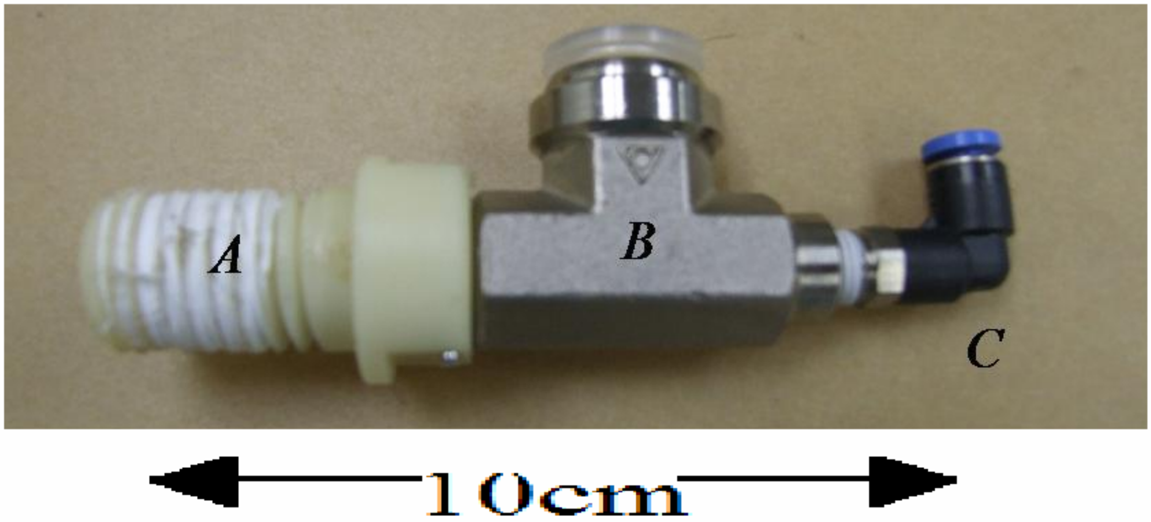


Figure 3.10.1: Image of commercial swirling jet micro-bubbler; parts A, B, and C are labeled to correspond with Figure 3.10.2.

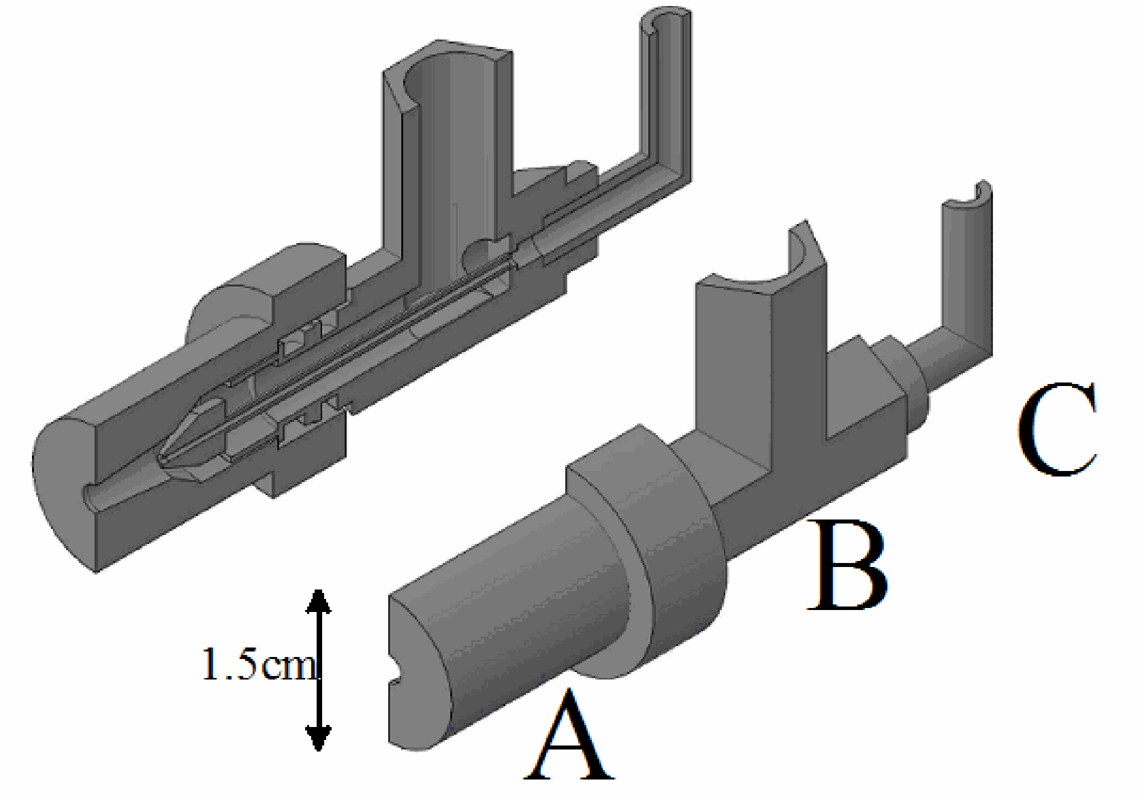


Figure 3.10.2: Cross-section of commercial bubbler; parts A, B, and C are labeled to correspond with Figure 3.10.1.

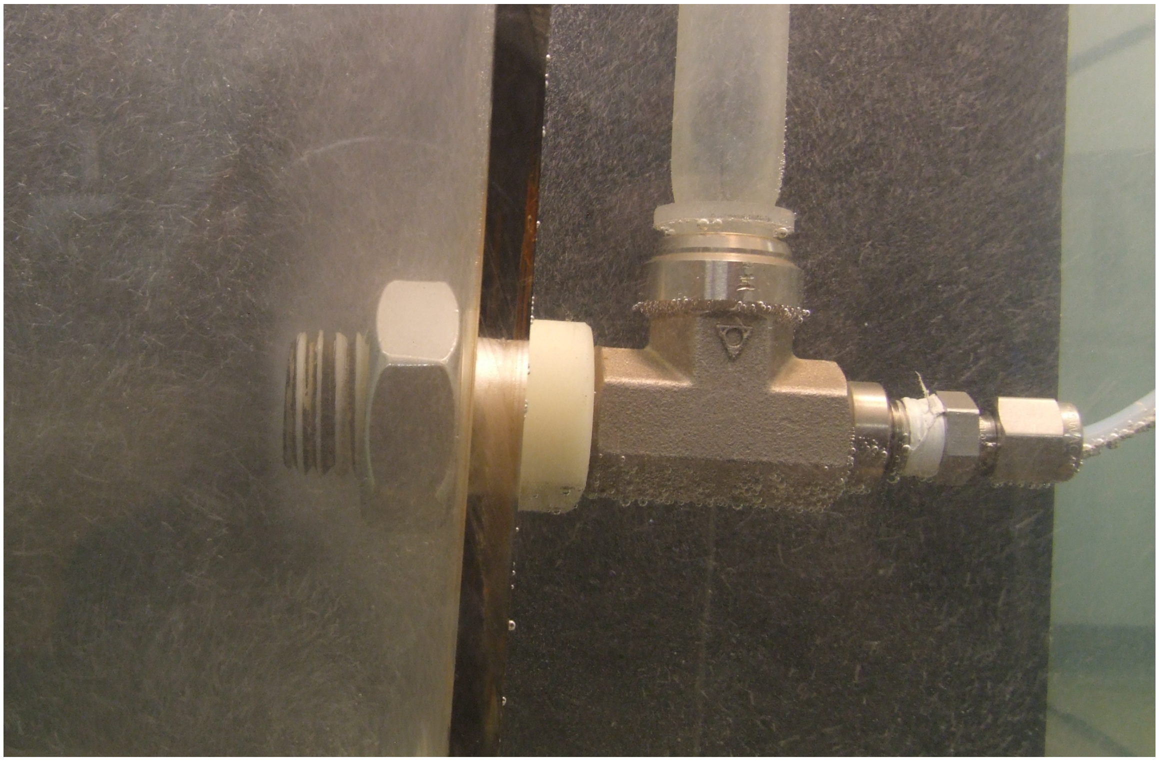

Figure 3.10.3: Image of commercial bubbler mounted in experiment tank.

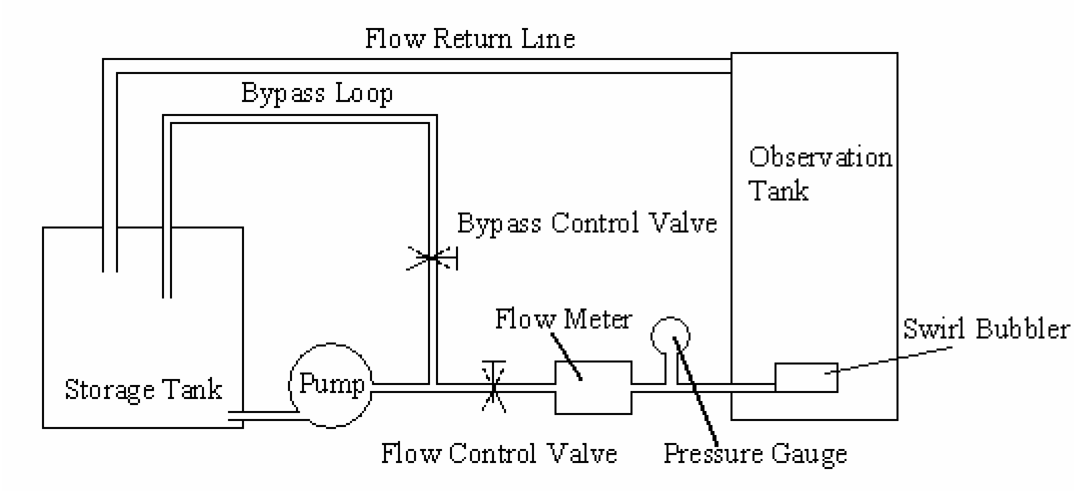


Figure 3.10.4: Schematic of test flow loop.

rates were measured using an inverted graduated tube assembly with an accuracy of 1.0 standard $cm^3/\min$ (1.0sccm).

Figure 3.11.1 shows the upstream pressure versus exit Reynolds number, with the downstream pressure near one atmosphere. The pressure losses scale according to the kinetic energy of the flow and the functional form given in (3.7.5) is confirmed quadratic. This suggests that the pressure losses scale according to the kinetic energy with a loss coefficient, $K_{loss}$ ~ 20, which is dependent only on the device geometry and body material; these data are compared in Figure 3.11.2. Figure 3.11.2 represents a comparison of three data sets denoted as: calibration, high speed video and still images. The calibration data set represents flow data collected during a calibration run on the flow loop, the high speed video data represents data collected during swirl rate data collection, and still images represent data collected while measuring bubble sizes using a high resolution still camera; Appendix E demonstrates the image processing steps.

## 3.12 Swirl Scaling Results

The flow swirl is introduced via a fluted insert that forces the flow into a spiral within the nozzle; located inside Part (a) of Figure 3.10.1. The flute pitch, $p_{flute}$, nozzle diameter and liquid viscosity determine the ratio of the exit angular frequency to the exit Reynolds number.

$$\begin{aligned} \omega_{exit} &= \kappa_{\omega} \cdot \upsilon_{liq} \cdot \mathrm{Re}_{exit} \\ \kappa_{\omega} &= \frac{p_{flute}}{D_{nozzle}} \end{aligned} \tag{3.12.1}$$

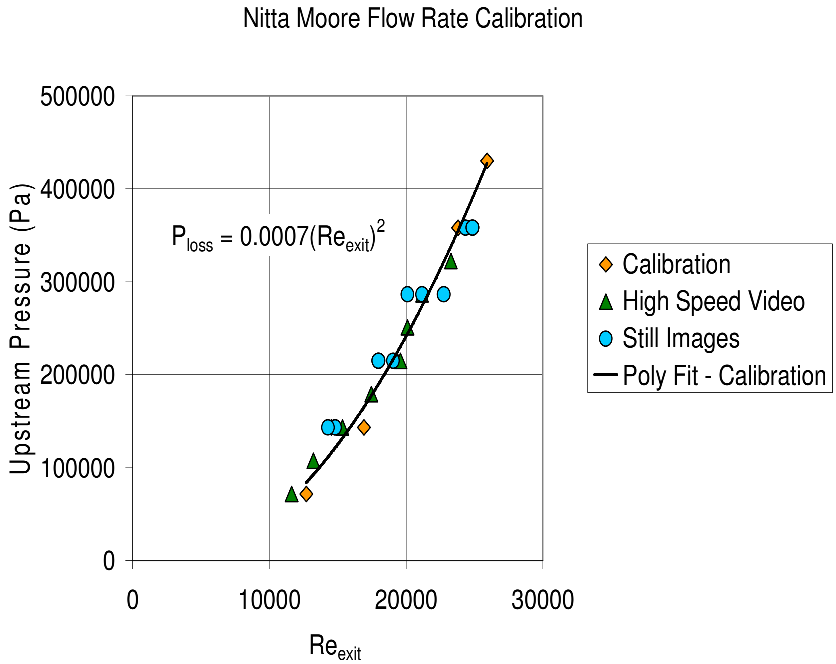


Figure 3.11.1. Comparisons of pressure losses versus exit Reynolds number, (3.11.1) is confirmed quadratic.

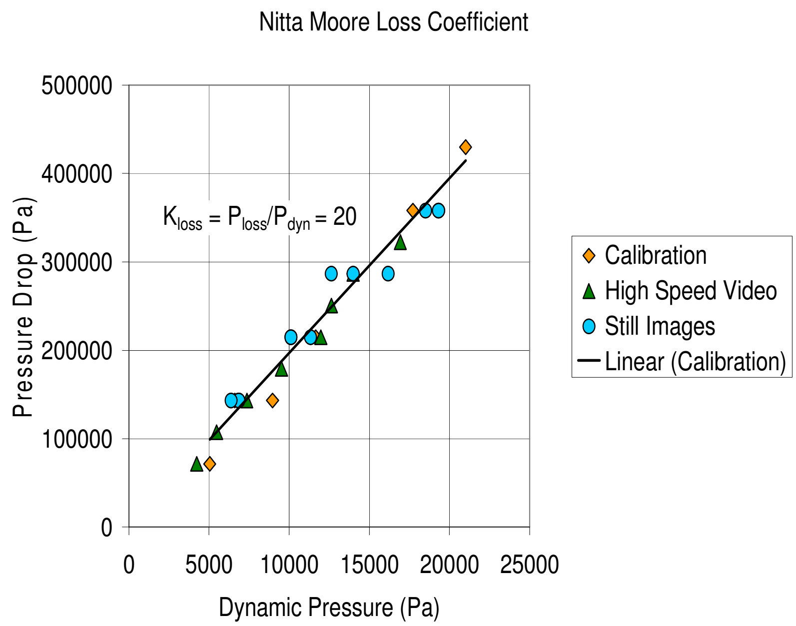


Figure 3.11.2. Pressure drop versus dynamic pressure; $K_{loss}$ ~20.

Measurement of the flute pitch, $p_{flute}$ =4.1$mm/rev$, generates the proportionality constant, $\kappa_{\omega} = 6.1\times 10^{4}\left\lfloor rev/m^{2}\right\rfloor$, which depends only on the bubbler geometry. The swirl rate in the flute is accelerated as the nozzle reduces the flow diameter while the angular momentum of the flow is conserved. Jet exit swirl rates are determined using an Olympus High-Speed camera to range from 600-1350 RPS; this data is presented in Figure 3.12.1. A proportionality constant of $\kappa_{\omega} = 5.9\times 10^{4}\left\lfloor rev/m^{2}\right\rfloor$ is calculated using a linear least squares fit to data from the high speed videos.

An audible pitch change in the operating noise of the micro-bubbler is observed with increasing liquid flow rates; this suggests a method to verify bubbler operation in liquid metals. Therefore acoustic data was obtained using 1s time histories from a PCB dynamic pressure sensor mounted on the outside of the glass bubble discharge/observation tank and analyzed for peak amplitude in the frequency domain. Frequency peaks in the acoustic data correspond to rotation rate measurements taken using high-speed video at $\mathrm{Re}_{exit} > 15{,}000$; this data is compared to high speed video measurements in Figure 3.12.1. Below this range the acoustic content associated with the bubbler swirl is indistinguishable from the background noise; the frequency content of the acoustic data at $\mathrm{Re}_{exit} \cong 1.5\times 10^{4}, 1.75\times 10^{4}, 1.9\times 10^{4}, \mathit{and}\, 2.1\times 10^{4}$ is compared in Figure 3.12.2.

The data in Figure 3.12.1 confirms a linear relationship between exit flow rates and angular velocity. The angular velocity is found to be a function of $\mathrm{Re}_{exit}$ and $\nu_{liq}$

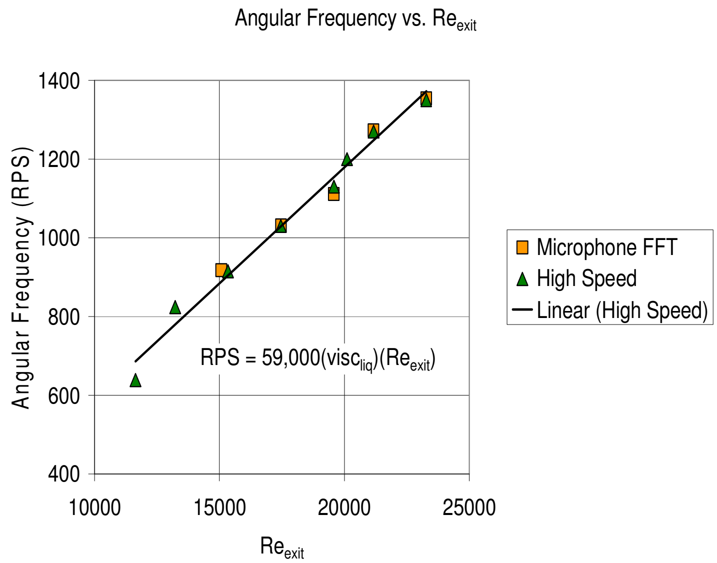


Figure 3.12.1. Angular frequencies as a function of exit Reynolds number; high-speed video data is compared to acoustic microphone data.

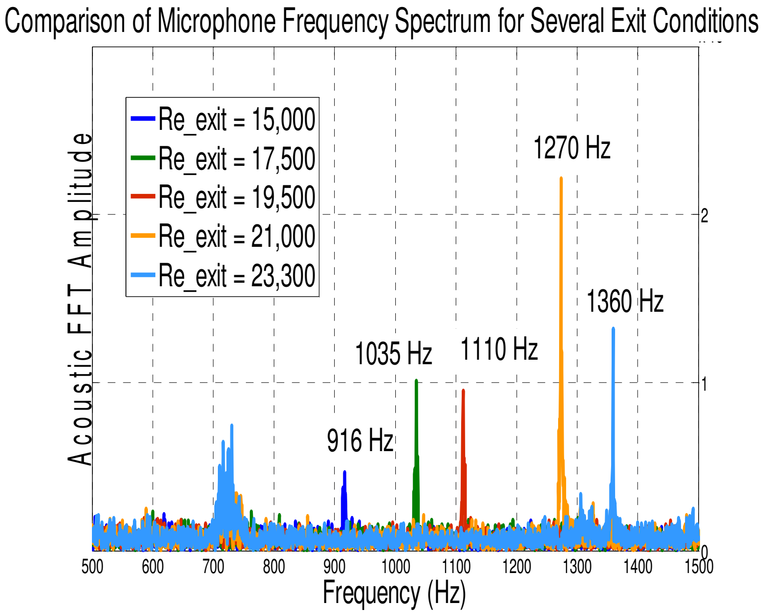


Figure 3.12.2. Frequency Spectrum of microphone data computed for various Reynolds numbers.

as well as a geometric proportionality constant, $\kappa_{\omega}$, which is independent of fluid flow properties. Finally, acoustic data correlates well with high-speed video provided $\mathrm{Re}_{exit} > 15{,}000$.

## 3.13 Critical Bubble Scaling Results

The average bubble diameter has been related to the Weber number associated with the kinetic energy of the liquid in (3.7.4). Also, (3.7.6) has been experimentally verified, suggesting that the dimensionality of the solution space is reduced from (3.7.3) to a power law relationship. A proposed power law exponent of $\alpha = 8/5$ based on isotropic turbulent jet theory is compared to an empirical value reported in the literature of $\alpha = 3/2$. The proposed power law relationship between liquid flow rate and critical bubble diameter is restated below

$$We = \beta \cdot \mathrm{Re}^{\alpha} \tag{3.8.1}$$

where,

$$\beta = \left(1.72 \times 10^{-6}\right) \cdot \varpi^{-3/2} \tag{3.8.3}$$

A high resolution still camera is used to determine that the bubble size distribution ranges from 50-200 microns with an average bubble diameter of ~100 micron; ~10 micron resolution provided bubble areas of about 50 pixels. An edge detection algorithm prepares raw images for a thresholding algorithm which creates binary images. These images are filtered for noise using a despeckle algorithm. The processed images are prepared for particle analysis using several morphological functions. These image processing techniques are implemented using WCIF Image-J freeware package.

The previous range of Reynolds numbers and gas flow rates were examined. Figure 3.13.1 compares the bubble size distribution at various $\mathrm{Re}_{exit}$ and gas flow rates. The 10micron imaging limits our ability to resolve the details of the size distributions. However, examination of the average bubble diameter at various Reynolds numbers demonstrates the functional relationship between Weber number and Reynolds number at the nozzle exit.

In Figure 3.13.2, a power law exponent of $\alpha = 8/5$ is compared to $\alpha = 3/2$ using (3.8.1). This result demonstrates that mixing-length type turbulence models correctly predict the gas break-up in a co-axial swirl jet bubbler while the empirical model under predicts the average bubble size. The model coefficient, given in (3.8.3), is also deemed probable based on legacy empirical models, mechanistic scaling and air/water data.

The breakup mechanism of a swirling jet bubbler requires a large relatively quiescent volume to initiate gas breakup. Designing a geometry suitable for bubble delivery within the mercury flow loop remains a challenge. A co-flowing geometry is examined briefly in Appendix O. Initial tests indicate that the swirling jet flow is preserved when the co-flowing pipe diameter is small compared to the exit nozzle. When the co-flow pipe diameter is increased to 15 times larger than the nozzle exit and the bubbler is placed off the pipe centerline the breakup mechanism is restored and an average bubble diameter of 250 microns is measured.

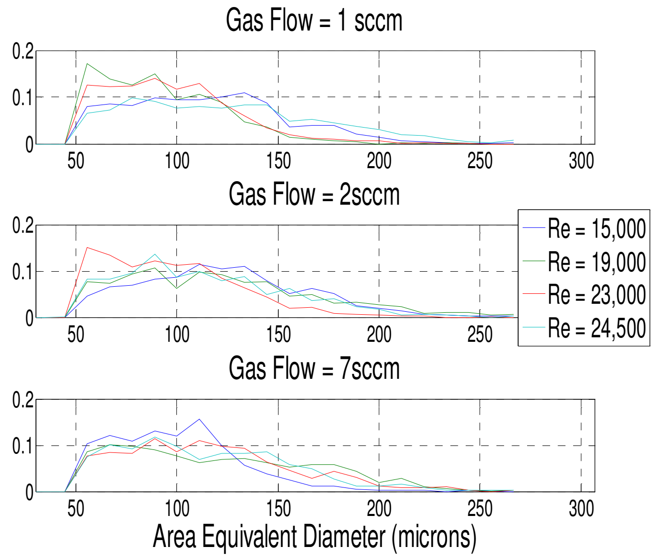


Figure 3.13.1. Bubble size distributions from still image data analyzed using WCIF ImageJ.

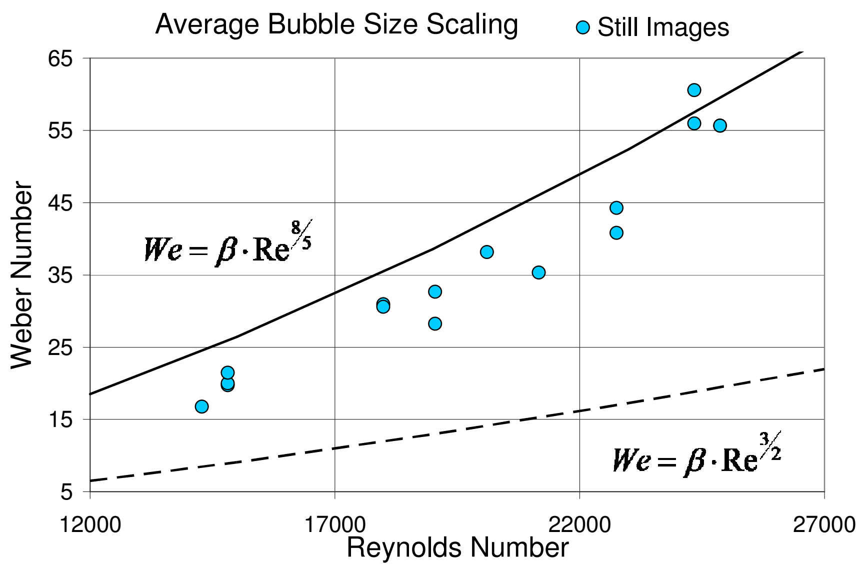


Figure 3.13.2. Experimental relationship between Weber number and Reynolds number.

# 4 GAS-VOID FRACTION DETERMINATION

## 4.1 INTRODUCTION

Verifying the performance of bubble injection methods for damage mitigation within the mercury target requires the measurement of bubble populations, including size distribution and gas volume fractions. Sound speeds are a strong function of void fraction, therefore measuring the mixture sound speed may provide a viable technique for verifying the performance of microbubble generators at the SNS. A vertical waveguide has been developed to measure sound speeds in bubbly water mixtures. Two strategies for determining sound speeds in bubbly mixtures along a waveguide which involve measuring pressure nodes and antinodes have been presented in the literature [20,21]. A fixed point strategy is better suited for the SNS environment. However fixed-point techniques present sound speed resolutions which are limited by the time required to establish sufficient acoustic energy to form standing wave modes. A two-point correlation technique is presented as the basis for a void-fraction measurement strategy suitable for the SNS application involving a single fixed pressure sensor. Several notable features of this strategy include: fixed pressure sensor, single (or a few) drive frequencies, and resolution limited by the system hardware/software sampling rates.

## 4.2 TWO-PHASE SOUND SPEED

Referring to Figure 4.2.1, Equation (4.2.1) gives the one-dimensional continuity equation for an incompressible fluid in a constant cross sectional area prism. Performing the

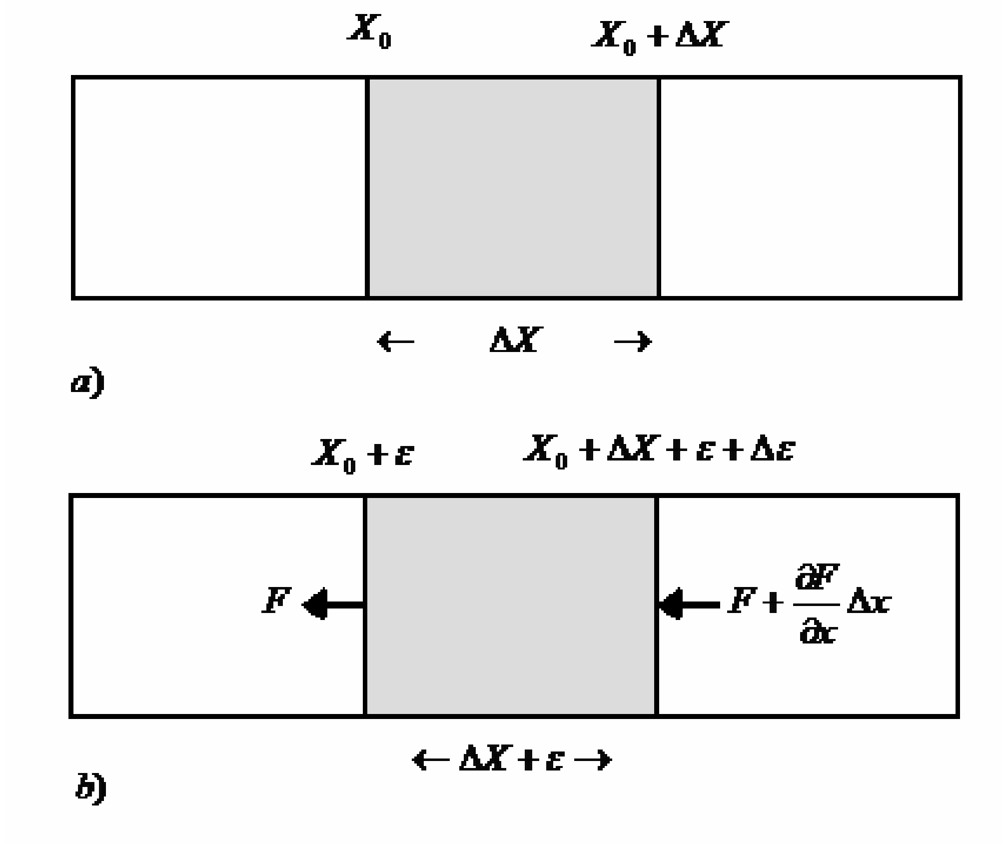


Figure 4.2.1: Prismatic volume used to develop force balance; adapted from Leighton [30].

indicated operation where, $\partial P / \partial \rho = c^2$ is the sound speed squared, yields (4.2.2)

$$\left[\frac{\partial \rho}{\partial t} + \rho \frac{\partial v}{\partial x} = 0\right] \cdot \frac{\partial P}{\partial \rho} \tag{4.2.1}$$

$$\frac{\partial P}{\partial t} + \rho c^2 \frac{\partial v}{\partial x} = 0 \tag{4.2.2}$$

The one dimension momentum equation reduces according to (4.2.3) with the assumption of an inviscid fluid and utilizing the incompressible continuity equation, $\nabla \cdot \vec{u} = 0$,

$$\frac{\partial v}{\partial t} + v \frac{\partial v}{\partial x} = g - \frac{1}{\rho}\frac{\partial P}{\partial x} + \frac{\partial}{\partial x}\tau \Rightarrow \frac{\partial v}{\partial t} = -\frac{1}{\rho}\frac{\partial P}{\partial x} \tag{4.2.3}$$

Differentiating (4.2.2) with respect to time and (4.2.3) with respect to space provides a substitution for $\frac{\partial}{\partial t}\frac{\partial v}{\partial x}$ yielding (4.2.4)

$$\frac{\partial^2 P}{\partial t^2} - c^2 \frac{\partial^2 P}{\partial x^2} = 0 \tag{4.2.4}$$

Integrating twice with respect to time yields the one dimensional linear wave equation given by

$$\frac{\partial^2 \varepsilon}{\partial t^2} = c^2 \frac{\partial^2 \varepsilon}{\partial x^2} \tag{4.2.5}$$

which describes a wave disturbance, $\varepsilon$, travelling in the $\pm x$ direction at speed, c.

The displacement of a fluid particle relative to the datum due to pressure changes within the system characterizes a bulk modulus, B,

$$B = -V\frac{\partial p}{\partial V} = \rho\left(\frac{\partial p}{\partial \rho}\right)_T \tag{4.2.6}$$

where $\partial p$ is the change in pressure due to a change in volume, $\partial V$. Applying (4.2.6) to a prismatic volume of width, $\Delta x$, provides the force on a plane at $x_0$ [22]

$$F(x_0) = -BA\frac{\partial \varepsilon}{\partial x} \tag{4.2.7}$$

where A gives the cross sectional area of the volume. Performing a first-order explicit Taylor series expansion of the force across the width of the volume and applying Newton's Second Law provides the net force on the element

$$\Delta F(x_0 + \Delta x/2) = -\Delta x\left.\frac{\partial F}{\partial x}\right|_{x=x_0} = \rho V\ddot{\varepsilon} \tag{4.2.8}$$

combination with (4.2.6) suggests

$$\rho\ddot{\varepsilon} = B\nabla^2\varepsilon \tag{4.2.9}$$

with the usual notation for time and spatial derivatives. Realization that (4.2.9) describes a longitudinal wave in the x-direction suggests that the solution has arguments of the form $(ct \pm x)$. Comparison with the linear wave equation (4.2.5) provides

$$c = \sqrt{\frac{B}{\rho}} \tag{4.2.10}$$

This solution extends to include any media acting as a compressible continuum with a definable average bulk modulus. Note that the derivation of the linear wave equation uses the assumption of inviscid, incompressible, irrotational flow which violates the assumption of a definable bulk modulus, however when the density fluctuations are small such that the density depends weakly on the magnitude of the pressure perturbations, such as in solids and Newtonian fluids or when wave amplitudes are small relative to the bulk properties, the linear wave equation holds. Also, since the solutions are sinusoidal in time and space, application of an implicit Taylor series ensures an $O(\Delta x^3)$ truncation error with identical results to (4.2.8).

The equation of state for gases is of the form

$$pV^{\gamma} = const \tag{4.2.11}$$

where the polytropic index, $\gamma$, varies from unity in the case of an isothermal process to $\gamma \sim 1.4$ in the case of an adiabatic process; for a perfect gas (4.2.11) reduces to the well-known Ideal Gas Law. The thermodynamic process line of the gas bubble compression is examined in Section 4.4. Differentiation of (4.2.11) with respect to V and substitution into (4.2.6) provides the bulk modulus

$$B = p\gamma \tag{4.2.12}$$

As mentioned, if the wave amplitudes are small in comparison to the bulk properties then the linear wave equation holds. Consequently (4.2.10) provides the sound speed in a gas for any thermodynamic process as

$$c = \sqrt{\frac{p\gamma}{\rho}} \tag{4.2.13}$$

with the gas density, $\rho$, being a constant.

Focusing on two phase sound speed requires several assumptions to be made; at low frequencies, such that the wave nature of the sound energy may be ignored, a bubbly mixture is assumed to be homogeneous [23]. This allows the density and elasticity or bulk modulus to be calculated as a mean value according to

$$\rho_m = \alpha \cdot \rho_g + (1-\alpha) \cdot \rho_l \tag{4.2.14}$$

$$\frac{1}{B_m} = \frac{\alpha}{B_g} + \frac{(1-\alpha)}{B_l} = \frac{\alpha \cdot B_l + (1-\alpha) \cdot B_g}{B_g \cdot B_l} \tag{4.2.15}$$

with subscript according to phase and given the volume fraction of gas, $\alpha$. Using (4.2.14) and (4.2.15), the sound speed is found using the ratio of the elasticity to the density according to (4.2.13)

$$c_m{}^2 = \frac{B_m}{\rho_m} = \frac{B_g \cdot B_l}{\{\alpha \cdot B_l + (1-\alpha) \cdot B_g\} \cdot \{\alpha \cdot \rho_g + (1-\alpha) \cdot \rho_l\}} \tag{4.2.16}$$

The elasticity of the bubble is found by differentiation of (4.2.11) according to

$$B_g = -V \cdot \frac{dp}{dV} = p\gamma \tag{4.2.17}$$

here $\gamma$ is the ratio of the heat capacity of the gas at constant pressure to that at constant volume. The bulk modulus of the gas undergoing isothermal compression is given by

$$B_T = p \tag{4.2.18}$$

Figure 4.2.2 shows the velocity of sound in a mixture of helium and water and Figure 4.2.3 shows velocity of sound in a mixture of helium and mercury for various thermodynamic process lines. In each case the velocity decreases with void fraction to a minimum at α = 50%. The minimum velocity for the case of water is ~22 m/s while for mercury the minimum is ~6 m/s. The bulk modulus and density of water are $2.2\times10^{9}\,Pa$ and $1\times10^{3}\,Kg/m^{3}$ and for mercury $28.5\times10^{9}\,Pa$ and $13.5\times10^{3}\,Kg/m^{3}$ .

## 4.3 Resonance Frequency; Minnaert Frequency

The dynamic response of an oscillator is examined in order to establish the limit on bubble size which will respond to pressure variation on the time scales involved in the energy deposition at the SNS as well as the sub-resonant response of a bubble. A spherical gas bubble suspended in a Newtonian fluid suddenly undergoing a step pressure change acts as an freely-oscillating spring-mass system where the gas compressibility generates the restoring force and the mass is the inertia of the moving liquid, hence (4.3.1) states an equation of motion,

$$m\ddot{\varepsilon}+k\varepsilon=0 \tag{4.3.1}$$

Where m is the mass of the oscillator, k is the spring constant, and $\varepsilon$ is the displacement of the oscillator.

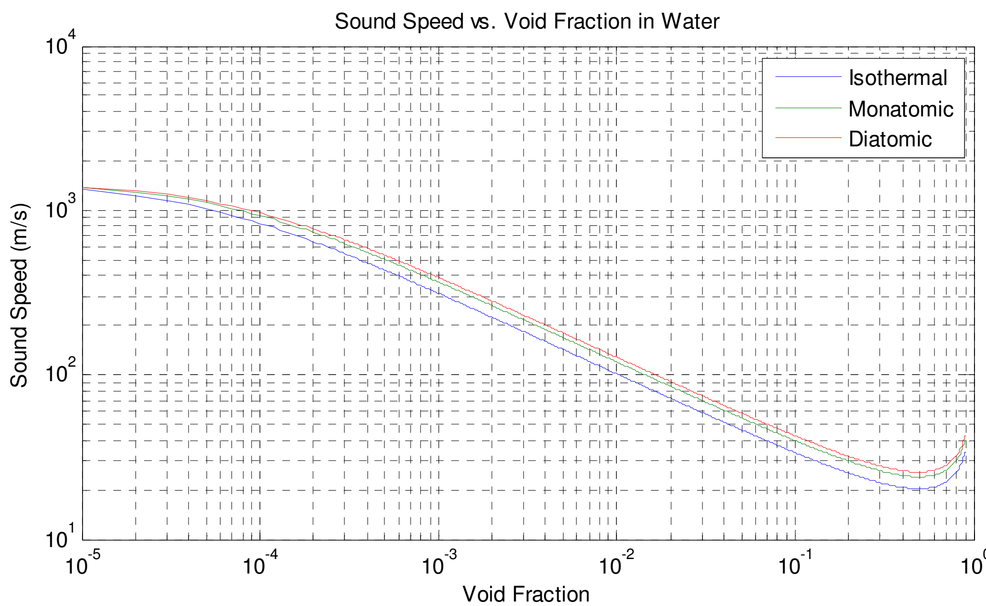


Figure 4.2.2: Sound Speed as a function of void fraction for helium/water system

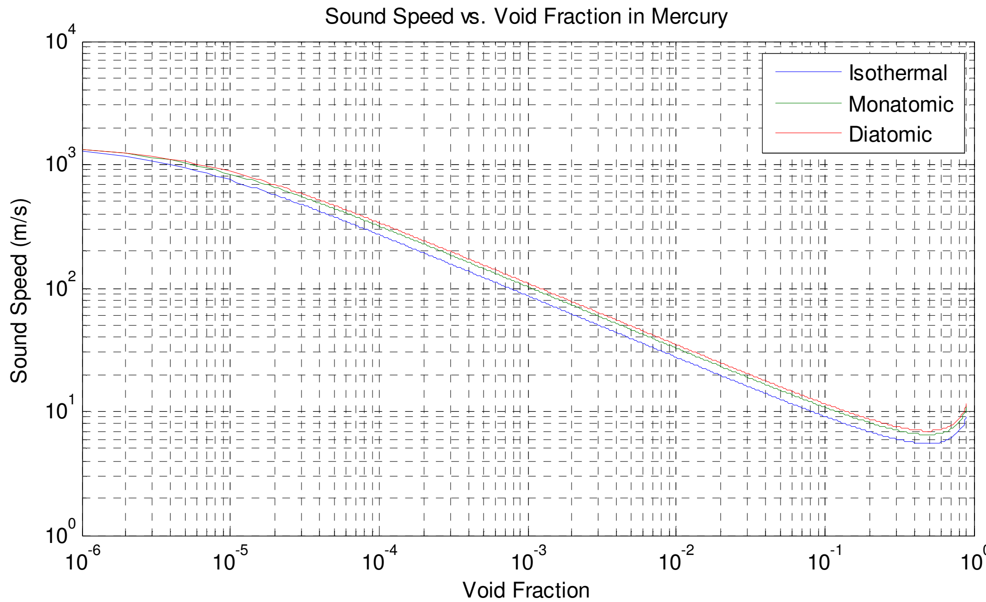


Figure 4.2.3: Sound Speed as a function of void fraction for helium/mercury system

Substitution of a trial solution, $\varepsilon = Ae^{i\omega_0 t}$, into (4.3.1) generates

$$\omega_0^2 = \frac{k}{m} \tag{4.3.2}$$

where $\omega_0$ is the resonant frequency of the bubble.

Minnaert first calculated the natural frequency of a spherical gas bubble undergoing low-amplitude oscillations by equating the kinetic energy of the liquid surrounding the bubble to the internal energy of the gas. He found the kinetic energy by taking the general solution of (4.3.1) and integrating the flow of liquid over shells extending from the bubble wall; for incompressible fluids conservation of mass dictates that the fluid flow in any shell can be equated to the flow at the surface of the bubble. He then found the internal energy from the work done in compressing the gas bubble using the assumption of an adiabatic process line. Thus Minnaert found the natural frequency [24],

$$\omega_0 = \frac{1}{2\pi R_{bub}}\sqrt{\frac{3\kappa p_0}{\rho}} \tag{4.3.3}$$

Strictly speaking the inertia associated with the bubble oscillating in a vacuum must also be included, however since the gas density is significantly smaller than the liquid density only the inertia of the surrounding liquid must be considered [22]. Also, the effects of surface tension have been ignored.

## 4.4 THERMAL BEHAVIOR OF AN OSCILLATING GAS BUBBLE

A thermal group that is important to thermal transient analysis is the thermal effusivity defined as

$$\varepsilon = \sqrt{k\rho c_p} \tag{4.4.1}$$

where k is the thermal conductivity, $\rho$ is the density and $c_p$ is the specific heat capacity. This thermal group is a measure of a materials ability to transport energy by conduction. A material with low effusivity has low conductivity and low heat capacity per unit volume. When two materials are in contact during a thermal transient the interface temperature is controlled by the material with high effusivity. The mercury effusivity, $\varepsilon_{Hg} = 3900$, is an order of magnitude larger than the thermal effusivity of helium, $\varepsilon_{He} = 360$, for conditions of interest to this study therefore the gas/liquid interface will be nearly isothermal and controlled by the temperature of the mercury during pressure and temperature changes in the helium.

Prosperetti [25]shows that an oscillating gas bubble expands/contracts along an isothermal or adiabatic process line depending on the thermal penetration depth and bubble radius. A dimensionless diffusivity is defined as

$$D = \frac{k}{\rho c_p \omega R_0^2} = \frac{\delta_{pen}^2}{R_0^2} \tag{4.4.2}$$

Neglecting initial conditions and convoluting the small amplitude gas pressure, a dimensionless frequency is defined as

$$\eta = \left(\frac{2}{D}\right)^{1/2} \tag{4.4.3}$$

In the limit that the dimensionless frequency is large the gas bubble expands/contracts along an adiabatic process line while in the limit that the dimensionless frequency is small the bubble undertakes an isothermal process line. Table 4.4.1 summarizes the thermal behavior of a gas bubble undergoing small amplitude oscillations.

A 30 μm gas bubble in mercury undergoing oscillations with a 1 μs period will have a thermal penetration depth of order, $O(\delta_{pen}) = 10^{-3}$. Comparison with Table 4.4.1 suggests the bubbles will expand/contract following an isothermal process line. The above analysis shows that under the conditions of interest to this study the gas temperature will be controlled by the temperature of the mercury.

## 4.5 Legacy Sound Speed Measurement Techniques: Fixed Point and Fixed Frequency

Legacy methods of calculating sound speeds in pipes employ an acoustic source to establish standing wave modes within the pipe. One technique uses a pair of fixed hydrophones and varies the drive frequency such that pressure nodes or antinodes are located at the measurement location. The other technique uses a pair of hydrophones with one being fixed and the other able to traverse

Table 4.4.1 Summary of the thermal behavior of an oscillating gas bubble.

$$\frac{O(R_0)}{O(\delta_{pen})} = O(\eta)$$

$$O(R_0) = O(\delta_{pen}) \Rightarrow O(\eta) = 1 \Rightarrow isothermal\,/\,adiabatic$$

$$O(R_0) > O(\delta_{pen}) \Rightarrow O(\eta) > 1 \Rightarrow adiabatic$$

$$O(R_0) < O(\delta_{pen}) \Rightarrow O(\eta) < 1 \Rightarrow isothermal$$

the length of the waveguide. A standing wave mode is established at a single drive frequency and the traversing hydrophone is positioned such that the wavelength of the standing mode can be measured.

Both techniques rely on knowledge of both the drive frequency and wavelength of the associated standing wave mode to calculate the speed of sound according to

$$c = \lambda \cdot f_{drive} \tag{4.5.1}$$

where $\lambda$ is the measured wavelength and $f_{drive}$ is the frequency of the acoustic source. The first technique utilizes a fixed pressure sensor and the sound speed resolution is a function of the resolution in the drive frequency such that

$$\Delta c = \lambda \cdot \Delta f_{drive} \tag{4.5.2}$$

The second technique utilizes a fixed drive frequency and the sound speed resolution is controlled by the resolution in the position of traversing pressure sensor such that

$$\Delta c = \Delta\lambda \cdot f_{drive} \tag{4.5.3}$$

## 4.6 Fixed Point Auto-Correlation Technique

A vertical waveguide, Figure 4.6.1, was developed to measure the sound speed of a bubbly mixture within the Woods limit. The main features of the vertical waveguide include: the main tube, anechoic chamber, side branch, bubble injection array, and traversing hydrophone (not shown). An electrodynamic shaker is coupled to the side-

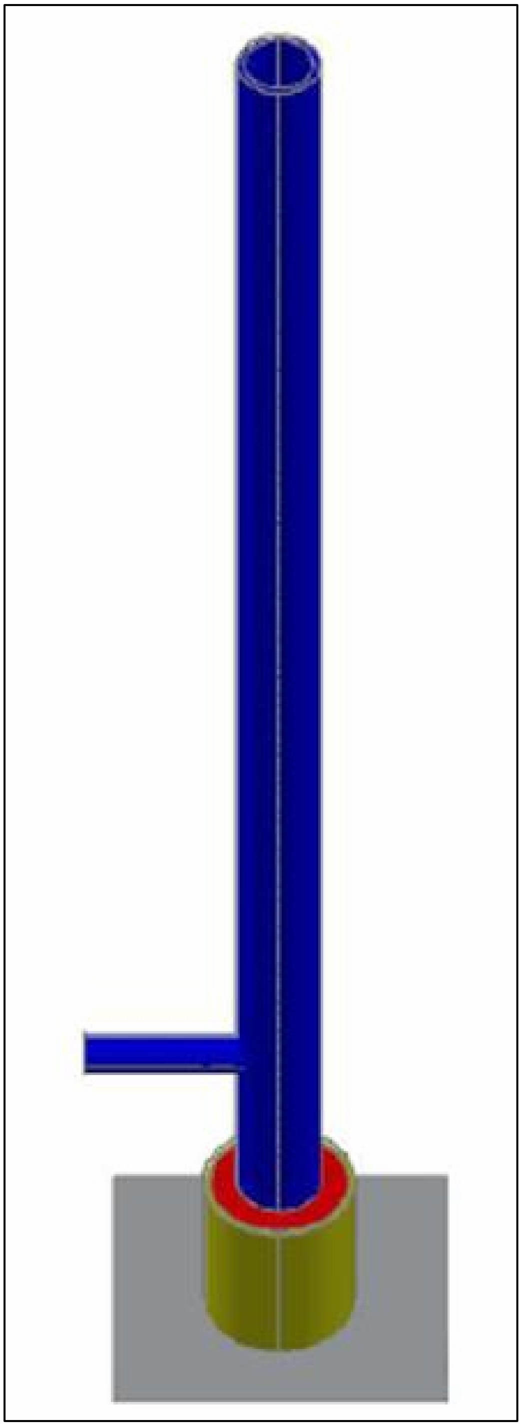

Figure 4.6.1. Rendered drawing of vertical waveguide.

branch through a piston-membrane assembly. The one-dimensional pressure distribution in the waveguide as a result of the piston movement at a given frequency, $\omega_{drive}$, can be written as

$$P(x,t) = P_0 \cdot e^{j \cdot (\omega_{drive} \cdot t - k \cdot x)} \tag{4.6.1}$$

Where the wavenumber is given by

$$k = \frac{\omega}{c_m} \tag{4.6.2}$$

And the mixture sound speed is the product of the waveguide length and the frequency of the first harmonic

$$c_m = \frac{\omega_{natural} \cdot L_{WG}}{n} \tag{4.6.3}$$

The spectral density represents a transformation in coordinates to the frequency domain and the pressure distribution can be defined by

$$\hat{P}(x,\omega) = \frac{P_0}{2\pi} \cdot e^{-ikx} \cdot \delta(\omega - \omega_{drive}) \tag{4.6.4}$$

A single-point correlation function is defined by integrating the product of the spectral densities at one location over the entire frequency domain

$$g(\xi) = \int_{-\infty}^{\infty} \hat{P}(x\ ,\omega) \cdot \hat{P}(x\ ,\omega + \xi) d\omega \tag{4.6.5}$$

This single point correlation is a measure of the 2-norm energy of the pressure signal as measured in the frequency domain at a frequency shift of $\xi$.

Substitution of the pressure distribution provides the following form

$$g(\omega_n\zeta)=\left(\frac{P_0}{2\pi}\right)^2\cdot\int_{-\infty}^{\infty}e^{-j\omega\cdot\frac{2x}{c_m}}\cdot\delta(\omega-\omega_{drive})\cdot\delta(\omega-\omega_{drive}+\omega_n\zeta)d\omega \tag{4.6.6}$$

Upon integration we are left with

$$g(\omega_n\zeta)=\left(\frac{P_0}{2\pi}\right)^2\cdot e^{-j(\omega_{drive}-\omega_n\cdot\zeta)\cdot\frac{2x}{c_m}}\cdot\delta(\omega_n\cdot\zeta) \tag{4.6.7}$$

If $\zeta\le 0$ then the above expression has maxima when the exponent is zero. Since the single-point correlation function is symmetric about zero we can conclude

$$\sup g(\omega_n\zeta)\Rightarrow|\zeta|=\frac{\omega_{drive}}{\omega_{natural}}\le\frac{\pi}{2} \tag{4.6.8}$$

The correlation coefficient, $\zeta$, defined above as the ratio of the drive frequency to the natural frequency of the waveguide is compared to pure water data in the following section.

## 4.7 WAVEGUIDE DESIGN: PISTON SOURCE AND PRESSURE AMPLITUDE IN WAVEGUIDE

The analysis of the linear wave equation demonstrates that the two-phase sound speed is a strong function of the gas volume fraction. Within the Woods limit the relationship between sound speed and void fraction is easily found from (4.2.18). Thus, measurement of pressure nodes and antinodes within an oscillating pressure field allows void fractions to be inferred from sound speed data. For this research an electrodynamic shaker in conjunction with a flat piston assembly introduces a pressure disturbance and dynamic pressure sensors map the resultant pressure field. Design parameters for the electrodynamic shaker and the piston assembly follow from a theoretical development of the axial pressure field due to an oscillating circular piston source in the near and far fields.

A flat piston source, Figure 4.7.1, is thought of as a collection of point sources each with a differential pressure given by (4.7.1) [26].

The piston source has a radius, a, and elemental pressure at a point $r'$ given by

$$dp(r', \theta, t) = j\frac{\rho_m \cdot \omega}{2\pi \cdot r'} \cdot u_0 \cdot e^{j(\omega t - kr')} \cdot dS \tag{4.7.1}$$

and source frequency, $\omega$, and wave number, k. The axial pressure is found by setting $\theta = 0$ so that $r' = r$ and integrating (4.7.1) over the disc according to

$$p(r,0,t) = \rho c u_0 e^{j(\omega t - kr)}\left[1 - e^{-jk\left(\sqrt{r^2 - a^2} - r\right)}\right] \tag{4.7.2}$$

The magnitude of the above expression gives the axial pressure amplitude

$$p(r,0) = 2\rho c u_0 \left|\sin\left\{\tfrac{1}{2} kr\left[\sqrt{1 + \left(a/r\right)^2} - 1\right]\right\}\right| \tag{4.7.3}$$

It is often convenient to define the input mechanical impedance of an acoustic source in terms of the mechanical impedance of the device radiating into a vacuum and the

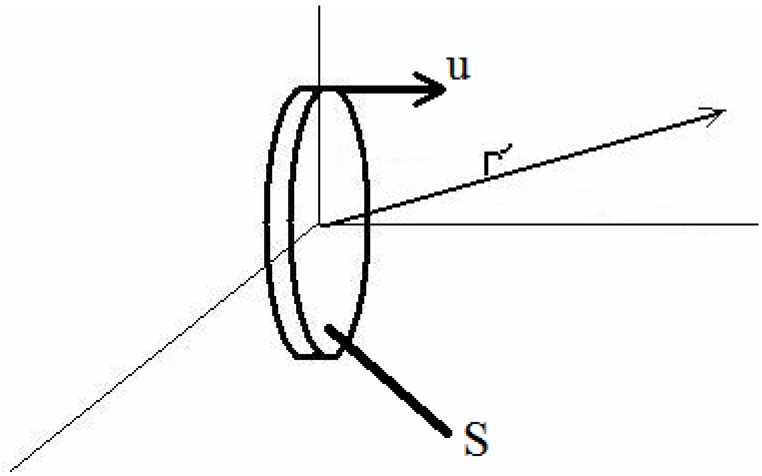


Figure 4.7.1. Piston Source.

radiation impedance of the wave propagating into a fluid [26]. Consider the transducer in Figure 4.7.1 with active area, S, moving with a normal velocity, u, and a normal force, $df_S$ , acting on dS of the transmitting face. If each component of the transducer is small compared to the wavelength of the propagated wave a lumped analysis of the impedance is used. The radiation impedance is then defined by

$$Z_r = \int_S \frac{df_S}{u} \tag{4.7.4}$$

According to (2.32), with a diaphragm with mass m, mechanical resistance $R_m$, and stiffness s, moving uniformly according to $u_0 = j\omega\xi_0$ under the applied force $f = Fe^{j\omega t}$ , Newton's Law yields

$$f - f_S - R_m \frac{d\xi_0}{dt} - s\xi_0 = m\frac{d^2\xi_0}{dt^2} \tag{4.7.5}$$

Taking the mechanical impedance $Z_m = R_m + j(\omega m - s/\omega)$ and solving for $u_0$

$$u_0 = \frac{f}{Z_m + Z_r} \tag{4.7.6}$$

Thus the applied force encounters the sum of the mechanical impedance of the source and the radiation impedance of the fluid [26]. The radiation impedance of a piston source is found by integrating the force on the element over the active face according to

$$Z_r = \rho c S\left[R_1(ka) + jX_1(ka)\right] \tag{4.7.7}$$

With the piston resistance and reactance functions given by

$$R_1(x) = 1 - \frac{2J_1(x)}{x}$$
$$X_1(x) = \frac{2H_1(x)}{x} \qquad (4.7.8)$$

Where $J_1$ and $H_1$ are Bessel functions.

The mechanical impedance of the source into a vacuum is calculated according to an electrical analogy given various mechanical properties of the diaphragm and driver. Figure 4.7.2 gives the mechanical impedance of a 110N shaker with an applied mass of 0.1 kg at frequency above resonance.

Taking the velocity of the piston in (4.7.6) as the velocity of the fluid to obtain the axial pressure amplitude of a circular piston source yields

$$p(r,0) = \frac{2\rho c f}{Z_m + Z_r}\left|\sin\left\{\tfrac{1}{2}kr\left[\sqrt{1+\left(a/r\right)^2} - 1\right]\right\}\right| \qquad (4.7.9)$$

At a point, $P$ ,near a piston source of finite size with all points oscillating in phase pressure waves are out of phase as demonstrated in Figure 4.7.3. Waves from $S$ have a shorter travel distance than those from $S'$; hence at some point, $P'$, the phase difference will generate an interference pattern within the noise level of the measurement device and this is the demarcation of the near and far field.

Taking the distance, $z = \overline{SP}$, we have the small angle approximation for the path difference, $\delta$,

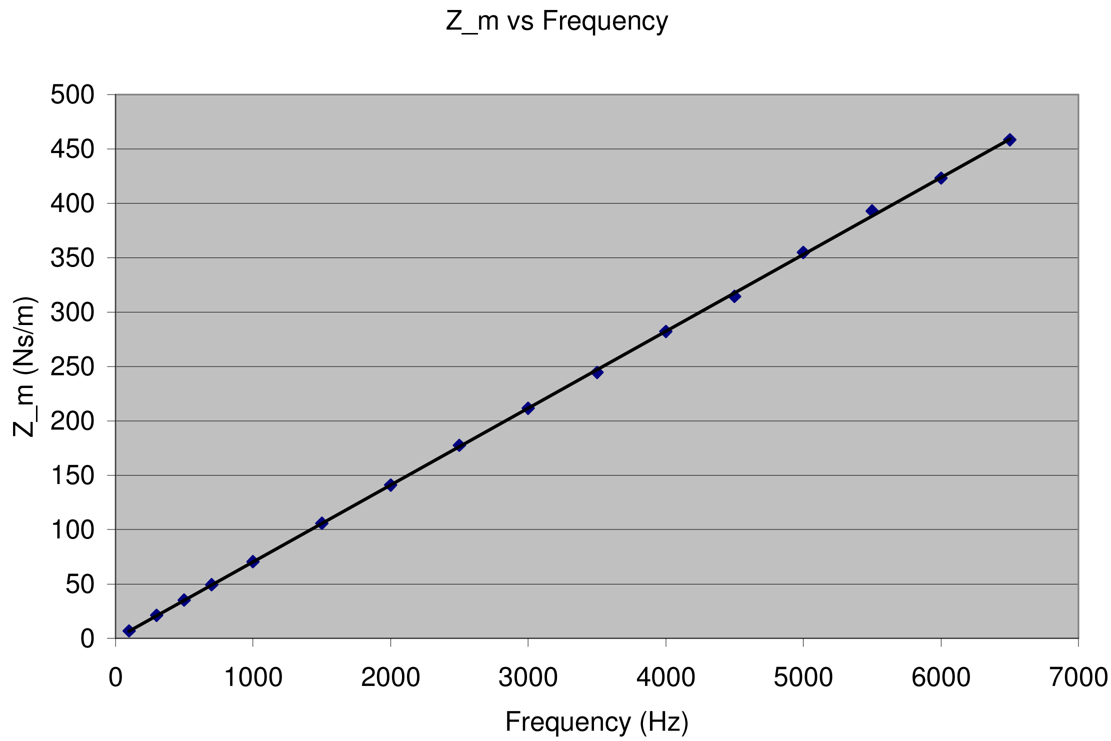


Figure 4.7.2. The mechanical impedance of a 110N shaker with an applied mass of 0.1 kg at frequency above resonance.

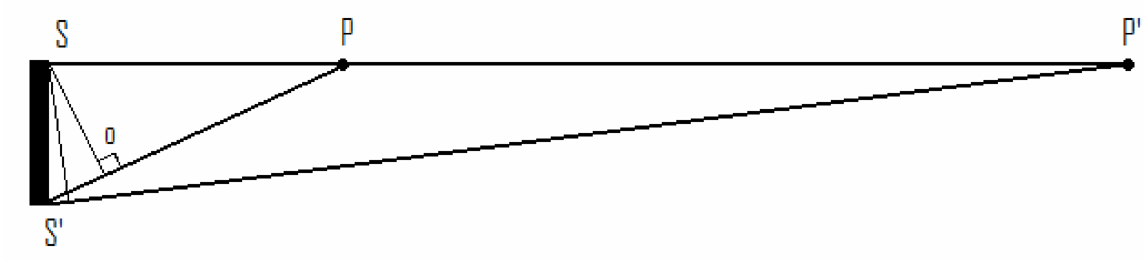


Figure 4.7.3: Path difference for the near and far field of a flat piston source.

$$\delta = 2a\sin\theta = 2a\tan\theta \approx \frac{4a^2}{z} \tag{4.7.10}$$

for $\theta = \angle SPO' = \angle OSS'$. The path difference represents a fraction of a wavelength that the two waves are out of phase, $\beta_\lambda = \frac{\delta}{\lambda}$ or equivalently $\phi = 2\pi\frac{\delta}{\lambda}$, thus it is clear as the distance between the source and receiver increases the phase difference becomes small [22]. Figure 4.7.4 shows a typical interference pattern for a short wavelength circular piston source, at wavelengths of interests such that the wavelength is much greater than the piston diameter; the directional factor in the far field is nearly unity and only the major lobe is observable [26].

Using (4.7.9) and the far field assumption we calculate the axial peak pressure from the shaker force and frequency, (4.7.11); Figure 4.7.5 shows the results of these calculations.

$$p(r) = \frac{\rho c^2 f}{2(Z_m + Z_r)} \cdot \frac{1}{\omega\ r} \tag{4.7.11}$$

Woods limit has provided a secondary tool which can be used to measure the void fraction of a given bubble population. An electro dynamic shaker can be used in order to establish a longitudinal standing wave in a bubbly mixture containing 300 μm radius bubbles with resonant frequency of 10 kHz. A standing wave of 0.3 m wavelength can measure void fractions between $\alpha = 1\times10^{-4}$ to $\alpha = 1\times10^{-2}$ with a frequency range of 300

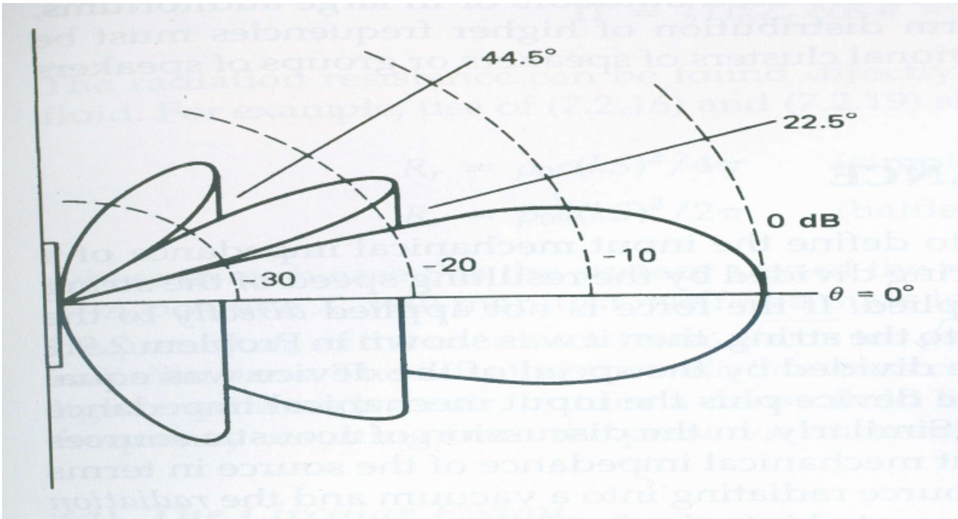


Figure 4.7.4 : Typical interference pattern for a circular plane source [31].

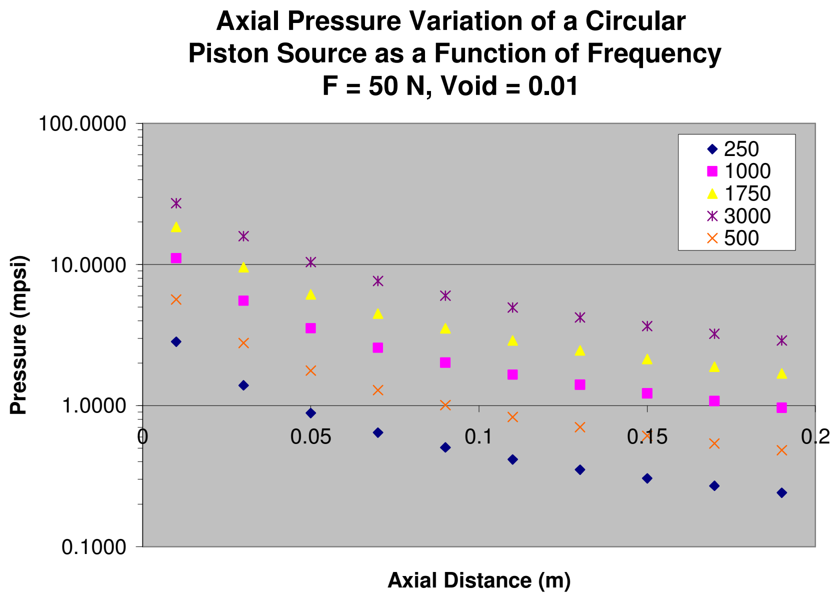


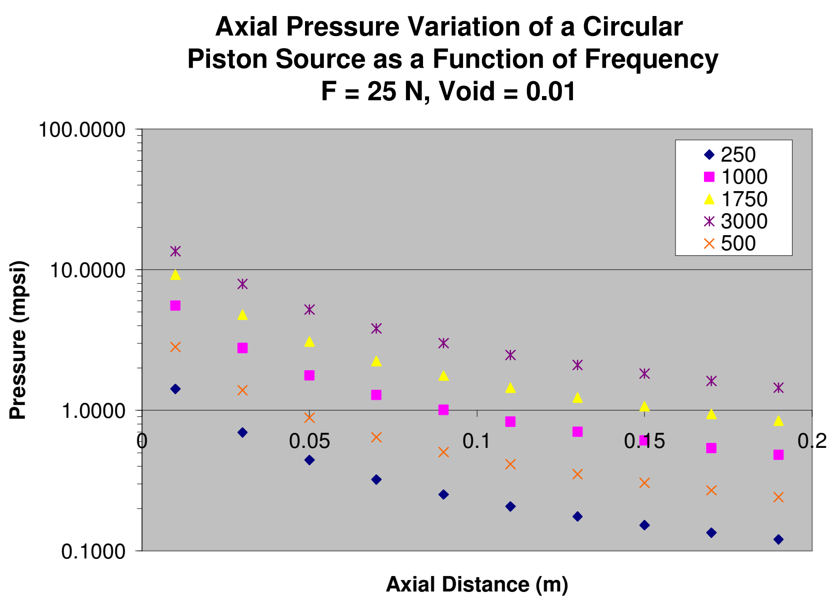


Figure 4.7.5. The axial pressure solution from (4.7.11) as a function of frequency and distance for a 25N peak force and 50 N peak force at a void fraction of $\alpha = 0.01$.

Hz to 3000 Hz.  A pressure variation at a distance of 0.15 m should vary by a maximum of 0.001 psi for a 10 N peak shaker at the minimum frequency.

## 4.8 RESULTS

The auto-correlation function defined in section 4.6 allows the natural frequency of the waveguide to be determined at any drive frequency using pressure measurements at one location.  This analysis was verified in a pure water system at several drive frequencies listed in Table 4.8.1.

Pressure data is collected using the RESON hydrophone picture in Figure 4.8.1. This device is suited well for laboratory applications due to the relatively high sensitivity.  An EC 6069 18VDC power source and an EC 6073 signal conditioner are also purchased. The 0-5VDC output is read directly from the DAQ board using previous MATLAB scripts.  The spectral density of the pressure data is calculated using a discrete Fourier transform; the spectral content of the 1000 Hz signal is shown in Figure 4.8.2.  Higher modes have distinct peaks at 2000 Hz and 3000 Hz and sub-drive frequency spectral content is also present.  The discrete auto-correlation is calculated according to (4.8.1); where N is the number of samples and n is the discrete correlation coefficient; Figure 4.8.3 shows this calculation for a drive frequency of 1000 Hz.  At a drive frequency of 1000 Hz the auto-correlation function has periodic maxima; the correlation coefficient corresponding to these peaks represents the ratio of the drive frequency to the natural frequency in the waveguide.  The correlation coefficient corresponding to peaks in the auto-correlation function are plotted in Figure 4.8.4.  The slope of the best-fit line, $m = 3.3\times 10^{-4}$, represents the inverse of a natural frequency in the waveguide,

$\omega_n = 3000Hz$. From 4.5.1, a standing wave mode with wavelength of 0.5m indicates that the sound speed in the pure water waveguide is c = 1,500 m/s.

$$g_{xx}(n) = \frac{1}{N}\sum_{i=1}^{N-n}(x_i - m_x)(x_{i+n} - m_x) \tag{4.8.1}$$

Further validation of this technique requires the measurement of two-phase sound speeds. Several difficulties were encountered when attempting this validation. Establishing a two-phase flow required the use of a pump which introduced significant noise into the system. Also, as indicated earlier, the swirling jet bubbler introduces noise at exit Reynolds numbers higher than 15,000. Further, the added system compressibility reduces the pressure intensity along the waveguide for a given piston source. Therefore the signal to noise ratio was reduced and spectral transformations were unreliable.

Table 4.8.1: Drive Frequencies for Piston Source

| Piston Drive Frequencies (Hz) | Water Column Height (m) |
| ---: | ---: |
| 1000 | 0.99 |
| 1250 | 0.98 |
| 1500 | 1.01 |
| 2000 | 1.01 |
| 2500 | 0.98 |

Figure 4.8.1: RESON TC 4032 hydrophone with cable, input module (right), and DC power supply (left); approximate length is 30cm.

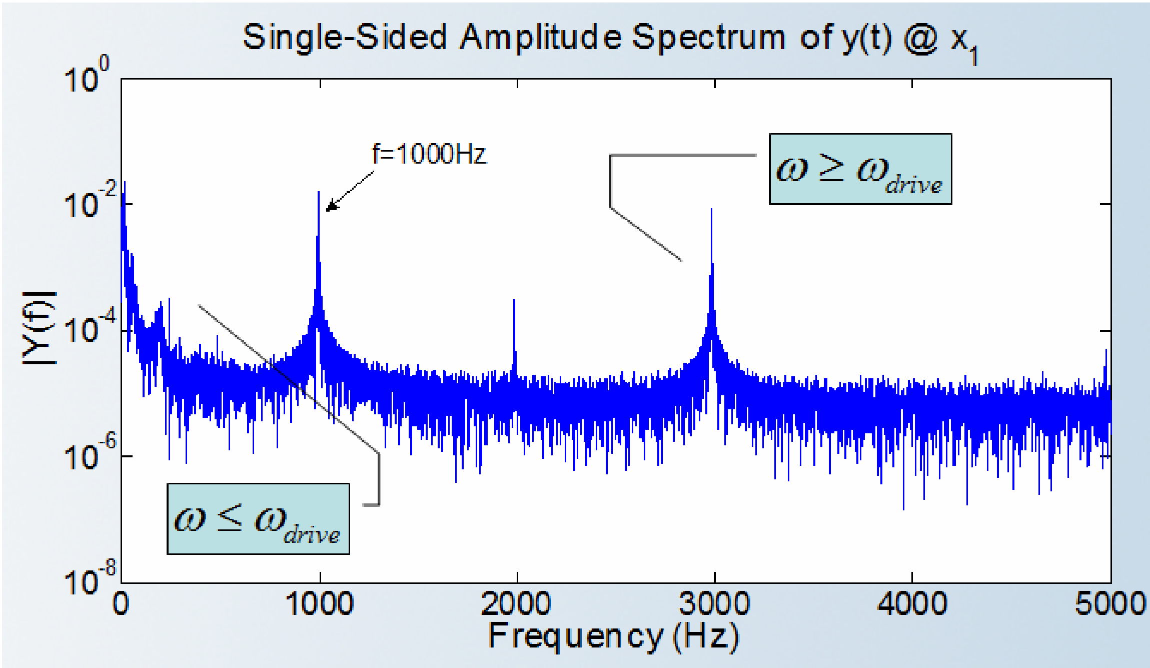


Figure 4.8.2: Spectral content at a drive frequency of 1000Hz.

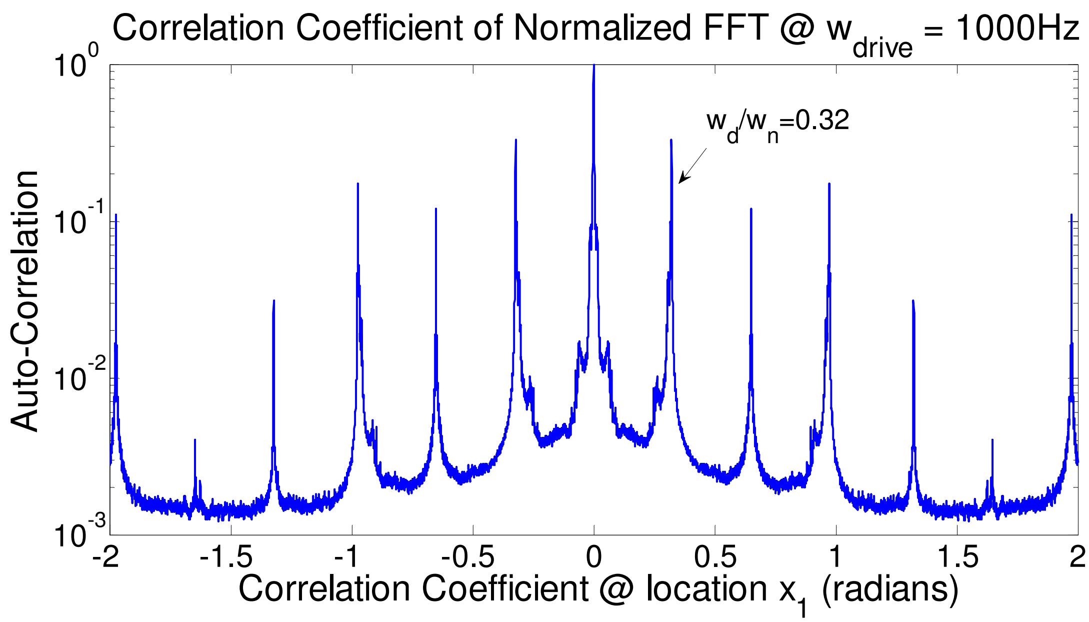


Figure 4.8.3: Auto-correlation of the spectral content at 1000 Hz drive frequency

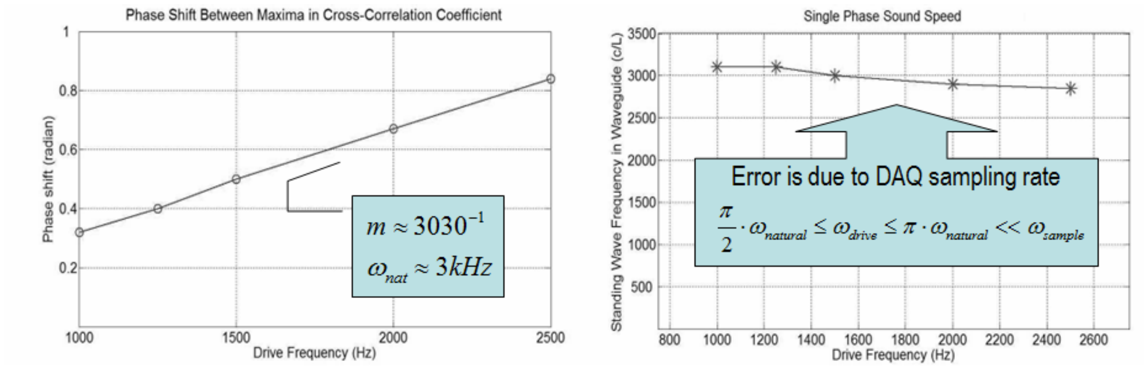


Figure 4.8.4: Correlation coefficient corresponding to maxima in the auto-correlation function plotted as a function of drive frequency.

# 5 CONCLUSION AND RECOMMENDATIONS FOR FUTURE WORK

The SNS target lifetime is limited by cavitation damage which can be mitigated by injecting a homogeneous mixture of small gas bubbles; a combination of bubble generation and bubble measurement methods were explored to address this challenge. Turbulent gas breakup models are developed to support scaling from water/air to mercury/helium systems. Verifying the performance of small gas bubble injection methods in the opaque liquid metal was explored using ultrasonic imaging methods by Nakamura. The mixture sound speed is a strong function of the gas void fraction; the so-called Woods limit predicts the sound speed of low frequency\low amplitude acoustic waves in a homogenous bubbly mixture. An innovative single-point auto-correlation method is developed and used herein to extract the single-phase sound speed from pressure measurements in a waveguide. Sounds speeds in a pure water system are measured in a vertical waveguide using the single point correlation technique. This water solid data set establishes the single point correlation technique as an experimentally viable theoretical method of determining sound speeds in a waveguide

Swirling jet bubblers have been used for production of small bubbles for some time. The modeling of the physics for the gas filament break-up was not well established. Dimensional analysis developed in this dissertation reveals the functional relationship between flow variables which assists in the development of closed form models for bubble breakup useful to engineering design. Pressure loss and swirl rate relationships are also presented in order to assist in engineering design. These combined models assist in extending the bubbler use to alternate fluids, such as liquid metals. A method for measuring jet swirl rates acoustically is verified using high speed video data. This will allow some validation of the bubbler performance in opaque fluids. Bubble break-up models based on energy dissipation generate a power-law relationship, with an exponent of $\alpha = 8/5$, relating Weber number to Reynolds number at the jet exit. Those models are compared to empirical models found in the literature providing a link between mechanistically based models, scaling arguments, and legacy empirical models. These models provide confidence in design parameters of swirl jet bubbles for the mercury/helium system.

All of the current experimental bubble breakup data is concerned with water/air and water/helium systems. Extending the experimental data sets to mercury/helium systems would enable verification of the scaling relationships in liquid metals. Bubble imaging techniques using ultrasound and proton radiography are two possible methods for measuring bubble size distributions in a lab setting. Further, the piston source strength and added noise due to bubble generation limit the ability of the current experimental setup to measure temporal pressure distributions. Therefore the auto-correlation technique needs experimental verification in a water/helium bubbly mixture as well as mercury solid and bubbly systems.

## REFERENCES

[1] Francis, M.F. Ruggles, A.E. Helium Bubble Injection Solution to the Caviation Damage at the Spallation Neutron Source. CAARI. 2008.

[2] Lu, B. Theoretical Study of Noble Gas Behavior in Mercury. University of Tennessee. May 2006.

[3] Riemer, B. In-beam experiment at WNR. Mitigation of Cavitation Damage in Liquid Metal Spallation Targets. SNS/ORNL. Feb. 2009.

[4] Felde, D. MIMTM Gas Wall Damage Mitigation Experiment. Mitigation of Cavitation Damage in Liquid Metal Spallation Targets. SNS/ORNL. Feb. 2009.

[5] Francis, M. The Solubility and Diffusivity of Helium in Mercury with Respect to Applications at SNS. University of Tennessee. May 2008.

[6] Hosack, L. Investigations on Hydrocyclones for the Spallation Neutron Source. University of Tennessee. Dec. 2007.

[7] Rosenblad, P. The SNS Target: Design, Parameters, and Constraints. SNS RRD Target Workshop. January 2008.

[8] neutrons.ornl.gov

[9] Ruggles, A.E. Spallation Neutron Source Target Window Response to the Pressure Pulses Caused by the Proton Beam. Final Report for SNS under subcontract #4000017011. December 2002.

[10] Moody, F. Introduction to Unsteady Thermofluid Mechanics. John Wiley & Sons. 1990.

[11] Walker, S.W. An Investigation of Gas Bubble Generation and Detection in Water and Mercury. The University of Tennessee. May 2010.

[12] Hinze, J.O. Fundamentals of the Hydrodynamic Mechanisms of Splitting in Dispersion Processes. Royal Dutch Shell Laboratory. A.I.Ch. E. Journal. Vol. 1. No.3.September 1955. pg.289-295.

[13] RELAP5/MOD 3.3 Code Manual, Volume 5, User's Guidelines, NUREG/CR-5535 , Rev 1- Vol 5 , December 2001.

[14] Batchelor, G.K. Proc. Cambridge Phil. Soc., 47, 359, 1951.

[15] Clay, P.H., Proc. Royal Acad. Sci., 43, 852, 1940.

[16] Martinez-Bazan, C. Montanes, J.L. Lasheras, J.C. On the Break-up of an Air Bubble injected in a Fully Developed Turbulent Flow. Journal of Fluid Mechanics. 1999.

[17] Todreas, N. Kazimi, M. Nuclear Systems I. Taylor & Francis. 1990.

[18] White, F. Viscous Fluid Flow, 3rd Ed. McGraw-Hill International. 2006.

[19] Tabei, K. Haruyama, S. Yamaguchi, S. Shirai, H. Takakusagi, F. Study of Micro-Bubble Generation by a Swirl-Jet. Journal of Environment and Engineering. Vol. 2. 2007.

[20] E. Silberman. J. Acoust. Soc. Am. 29. 925. 1957.

[21] A.E. Ruggles. The Propagation of Pressure Perturbations in Bubbly Air/Water Flows. RPI. 1987.

[22] T.G. Leighton. The Acoustic Bubble. Academic Press. 1994.

[23] A. B. Wood, A Textbook of Sound. (1941)

[24] Minnaert, M., 1933, On musical air-bubbles and the sound of running water. *Philosophical Magazine*, vol. 16, pp.235–248

[25] Prosperetti, A. The Thermal Behavior of an Oscillating Bubble. Journal of Fluid Mechanics, Vol. 222, pp:587-616, 1991.

[26] Kinsler, L., Frey, A. Fundamentals of Acoustics. Wiley Publishing. 4th Edition. 2000.

[27] Baker, A.J. The Computational Engineering Sciences. J-Computek Press. Loudon, TN. 2006.

[28] Sadatomi, M. Kawahara, A. Kano, K. Ohtomo, A. Performance of a new micro-bubble generator with a spherical body in a flowing water tube. Experimental Thermal and Fluid Science. Vol. 29. 2005. pg. 615-623.

[29] Gordillo, J. Cheng, Z. Ganan-Calvo, A. Marquez, M. Weitz, D.A. A new device for the generation of microbubbles. Physics of Fluids. Vol. 16. August 2004. pg. 2828-2834.

[30] Ruggles, A.E. Sawyer, A. Giar, R. Smith, T. Sounds Speeds, Fundamental Pipe Frequencies, and Fluid Transients: Annual Report #3. Subcontract # 4000021715. April 2004.

# APPENDIX A: THERMOPHYSICAL AND MECHANICAL PROPERTIES OF WATER, MERCURY, AND HELIUM

| | Water | Mercury | Helium |
|---|---|---|---|
| Sound Speed (m/s) | 1500 | 1450 | 972 |
| Density (kg/m^3) | 1000 | 13500 | 2.7 |
| Viscosity (Pa*s) | 1.00E-03 | 1.53E-03 | 1.90E-05 |
| Surface Tension (N/m) | 7.50E-02 | 4.87E-01 | - |
| Bulk Modulus (Pa) | 2.20E+09 | 2.85E+10 | - |
| Thermal Conductivity (W/(m*K)) | 6.00E-01 | 8.30E+00 | 0.15 |
| Isobaric Thermal Expansion (1/C) | 1.82E-04 | 2.07E-04 | - |
| Molar Volume (m^3/mole) | 1.80E-05 | 1.48E-05 | - |

# APPENDIX B: FINITE ELEMENT ALGORITHM

```
% FEm.PSE template

tic;

clear all

clc

global X1;        % array for node coordinates


% constant data

k_basis = 1;        %Basis

Ne = 50;             %number of elements

deltt = 1e-6;       %time step

total_time = 666e-6;    %Total simulation time (sec)


rho = 13500;

c = 1500;

A = rho*c^2;%1;

B = 1/rho;%1;

L = 1;              %Length of domain

f = 0;    %Moody friction factor

max_iteration = 10;

convergence = 1e2;

theta = 1;

CFL = c*(deltt)/(L/Ne)


% uniform discretization

ndelt = int32(total_time/deltt)        %number of time steps
```

```
nnode = k_basis*Ne+1;
X1 = linspace(0,L,nnode);
t = linspace(0,total_time/c,ndelt);
% distributed data at the nodes

% load the FE matrix library
load femlib;

%Initial Conditions
Q = zeros(2*nnode,ndelt);
%Q(nnode:nnode,1) = [20e6];
Q(1:nnode,1)=linspace(1e5,1e5,nnode);     %Press
%Q(nnode:nnode,1) = [20e6];
Q(nnode+1:2*nnode,1)=linspace(-1,-1,nnode);     %Vel
Q(2*nnode,1) = 0;

%loop for time
    MASSA = asjac1D([],[],[],0,'A200L',[]);
    A201A = asjac1D([],[],[],-1,'A201L',[]);
    MASSG = [MASSA,zeros(nnode,nnode);zeros(nnode,nnode),MASSA];
    A201G = [zeros(nnode,nnode),A*A201A;B*A201A,zeros(nnode,nnode)];
    error = zeros(max_iteration,ndelt);
    JPP = asjac1D([],[],[],0,'A200L',[]);
    JPv = asjac1D(theta*deltt*A,[],[],-1,'A201L',[]);
    JvP = asjac1D(theta*deltt*B,[],[],-1,'A201L',[]);
    Jvv = asjac1D([],[],[],0,'A200L',[]);
    JAC = [JPP,JPv;JvP,Jvv];
```

```
    %Neumann JAC BC
      %JAC(nnode+1,1) = 1e10;            %Wave dv/dx=0 @ node=1
     %JAC(nnode+1,nnode+1) = 1e10;            %Wave dv/dx=0 @ node=1
     %JAC(nnode,nnode) = 1e10;      %Wave dP/dx=0 @ node=nnode
%     JAC(nnode,2*nnode) = 1e10;      %Wave dP/dx=0 @ node=nnode
    JAC = JAC^(-1);
    for i = 1:ndelt
    RESPn = asres1D(A,[],[],-1,'A201L',Q(nnode+1:2*nnode,i));
    RESvn = asres1D(B,[],[],-1,'A201L',Q(1:nnode,i));
    %RESvn = RESvn +
asres1D(f,[],Q(nnode+1:2*nnode,i),0,'A3000L',Q(nnode+1:2*nnode,i));
    RESn = [RESPn;RESvn];

    %Solve linear algebra
    delQ = -JAC*(deltt*RESn);

    %Enforce BC
    %delQ(1) = 0; %dP/dx at left node
    %delQ(nnode) = 0; %dP/dx at right node
    delQ(nnode+1) = 0; %dv/dx at left node
    delQ(2*nnode) = 0; %dv/dx at right node


    %Advance Newton method
    Q(:,i+1) = Q(:,i)+delQ;
```

```
    if double(i)/500 == i/500
        i
    end

end
toc
%compute Energy Norm using [MASSG+A201G] (without Dirichlet BC)
format long; % display Enorm in long format
Enorm = 0.5*Q(:,ndelt)'*(MASSG+A201G)*Q(:,ndelt)
format short;
% Plot initial pressure profile using handle:
figure(1)
h1=plot(X1,Q(1:nnode,1),'erasemode','xor');
xlabel('Axial Distance (m)')
ylabel('Pressure (Pa)')
minQ = min(min(Q(1:nnode,:)));
maxQ = max(max(Q(1:nnode,:)));
% Now plot the rest of the profiles:
a=1;
for i=2:int32(ndelt/2000)+1:ndelt
  i = double(i);
  tz=Q(1:nnode,i);
  set(h1,'xdata',X1,'ydata',tz);   %change data given to handle h1
  drawnow;
  title(['Pressure profile @ t = ',num2str(i*deltt)])
  axis([0 L min([-0.01,1.1*min(min(Q(1:nnode,:)))])
max([0,1.1*max(max(Q(1:nnode,:)))])])
  pressure(a)=getframe(gcf)
```

```
  a = a+1;
  %pause(.01)

end
% % Plot initial pressure profile using handle:
figure(2)
h1=plot(X1,Q(nnode+1:2*nnode,1),'erasemode','xor');
xlabel('Axial Distance (m)')
ylabel('Velocity (m/s)')
minQ = min(min(Q(1:nnode,:)));
maxQ = max(max(Q(1:nnode,:)));
% Now plot the rest of the profiles:
for i=2:int32(ndelt/2000)+1:ndelt
  i = double(i);
  tz=Q(nnode+1:2*nnode,i);
  set(h1,'xdata',X1,'ydata',tz);   %change data given to handle h1
  drawnow;
  title(['Velocity profile @ t = ',num2str(i*deltt)])
  axis([0 L min([-0.01,1.1*min(min(Q(nnode+1:2*nnode,:)))])
max([0,1.1*max(max(Q(nnode+1:2*nnode,:)))])])

%pause(.01)

end
%Plot Pressure profile at several times
figure(3)
ndelt = double(ndelt);
```

```
plot(X1,Q(1:nnode,int32(1)),X1,Q(1:nnode,int32(ndelt*1/3)),X1,Q(1:nnode
,int32(ndelt*2/3)),X1,Q(1:nnode,int32(ndelt*3/3)))

title(['Pressure Profile: deltt = ',num2str(deltt),', L =
',num2str(L),', Ne = ',num2str(Ne),', c = ',num2str(sqrt(A*B)),', theta
= ',num2str(theta)])

legend('t = 0',['t = ',num2str(ndelt*1/3*deltt)],['t =
',num2str(ndelt*2/3*deltt)],['t = ',num2str(ndelt*3/3*deltt)])

axis([0 L min([-.01,min(min(Q(1:nnode,:)))])
max([0,1.1*max(max(Q(1:nnode,:)))])])

xlabel('Axial Distance (m)')

ylabel('Pressure (pa)')

%Plot Pressure profile at several times

figure(4)

ndelt = double(ndelt);

plot(X1,Q(nnode+1:2*nnode,int32(1)),X1,Q(nnode+1:2*nnode,int32(ndelt*1/
3)),X1,Q(nnode+1:2*nnode,int32(ndelt*2/3)),X1,Q(nnode+1:2*nnode,int32(n
delt*3/3)))

title(['Velocity Profile: deltt = ',num2str(deltt),', L =
',num2str(L),', Ne = ',num2str(Ne),', c = ',num2str(sqrt(A*B)),', theta
= ',num2str(theta)])

legend('t = 0',['t = ',num2str(ndelt*1/3*deltt)],['t =
',num2str(ndelt*2/3*deltt)],['t = ',num2str(ndelt*3/3*deltt)])

axis([0 L min([-0.01,1.1*min(min(Q(nnode+1:2*nnode,:)))])
max([0,1.1*max(max(Q(nnode+1:2*nnode,:)))])])

xlabel('Axial Distance (m)')

ylabel('Velocity (m/s)')
```

気液せん断方式マイクロバブル発生器

# 泡多郎
# AWATARO

CATA-10070A-01

NITTA MOORE

## Appendix D: Microphone Specs

Various properties of the 103B01 PCB sensor.

| **PERFORMANCE** | **ENGLISH** |
|---|---|
| Measurement Range(± 5 V output) | 3.33 psi |
| Useful Overrange(± 10 V output) | 6.67 psi |
| Sensitivity(± 15 %) | 1500 mV/psi |
| Maximum Pressure | 250 psi |
| Resolution | 0.02 mpsi |
| Resonant Frequency | ≥ 13 kHz |
| Rise Time | ≤ 25 µ sec |
| Low Frequency Response(-5 %) | 5 Hz |
| Non-Linearity | ≤ 2.0 % FS |
| **ENVIRONMENTAL** | |
| Acceleration Sensitivity | ≤ 0.0005 psi/g |
| Temperature Range(Operating) | -100 to 250 °F |
| Temperature Coefficient of Sensitivity | ≤ 0.2 %/°F |
| Maximum Flash Temperature | 1000 °F |
| Maximum Shock | 1000 g pk |
| **ELECTRICAL** | |
| Output Polarity(Positive Pressure) | Positive |
| Discharge Time Constant(at room temp) | ≥ 0.1 sec |
| Excitation Voltage | 20 to 30 VDC |
| Constant Current Excitation | 2 to 20 mA |
| Output Impedance | ≤ 100 ohm |
| Output Bias Voltage | 7 to 13 VDC |
| **PHYSICAL** | |
| Sensing Element | Ceramic |
| Housing Material | Stainless Steel |
| Diaphragm | 316L Stainless Steel |
| Sealing | Epoxy |

| | |
|---|---|
| Electrical Connector | Integral Cable |
| Cable Termination | Pigtail Ends |
| Weight | 0.115 oz |
| Cable Type | 32 AWG stranded wires |
| Cable Length | 15 in |

# APPENDIX E: IMAGE J PROCEDURE

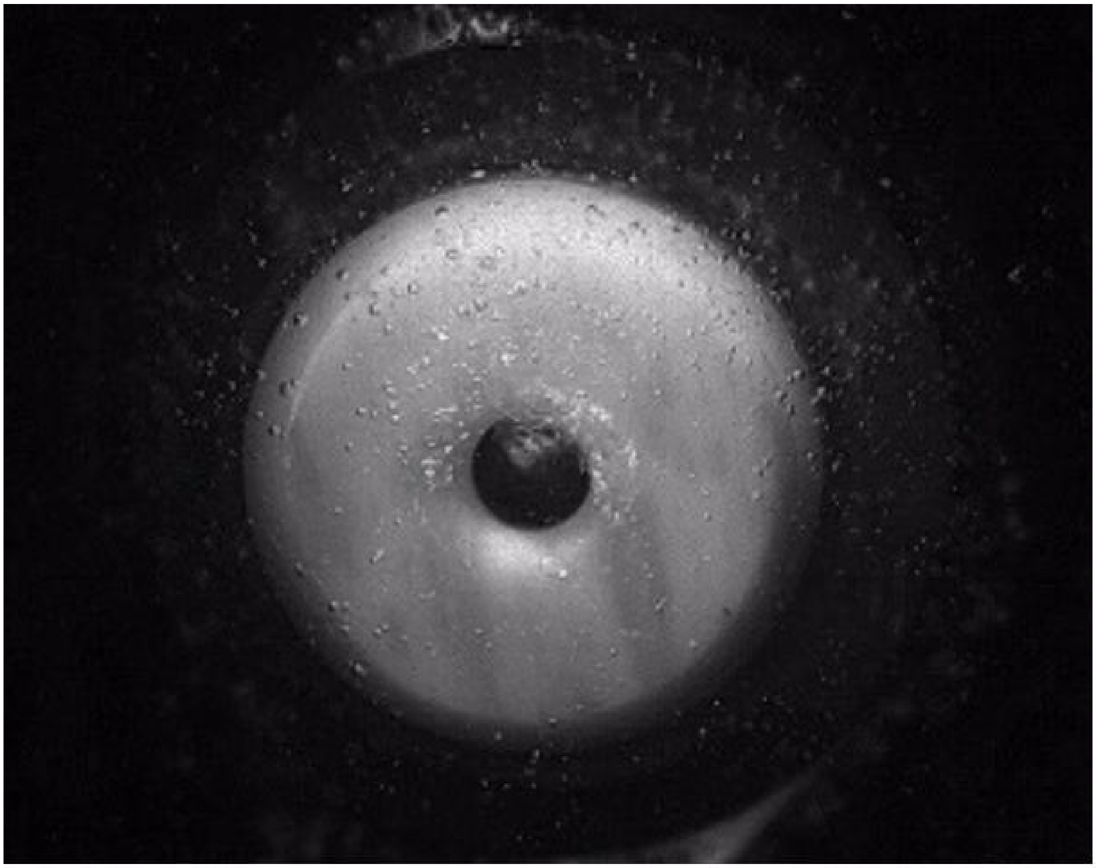

Figure E.1: Raw image.

Figure E.2: Cropped image with background subtracted.

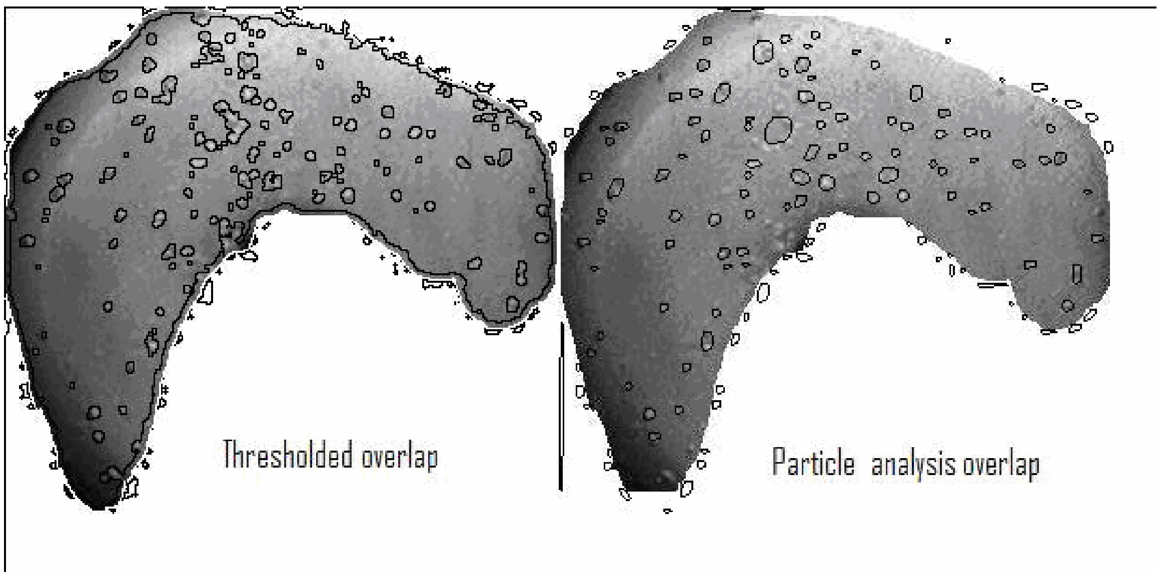


Figure E.3: Thresholded image.

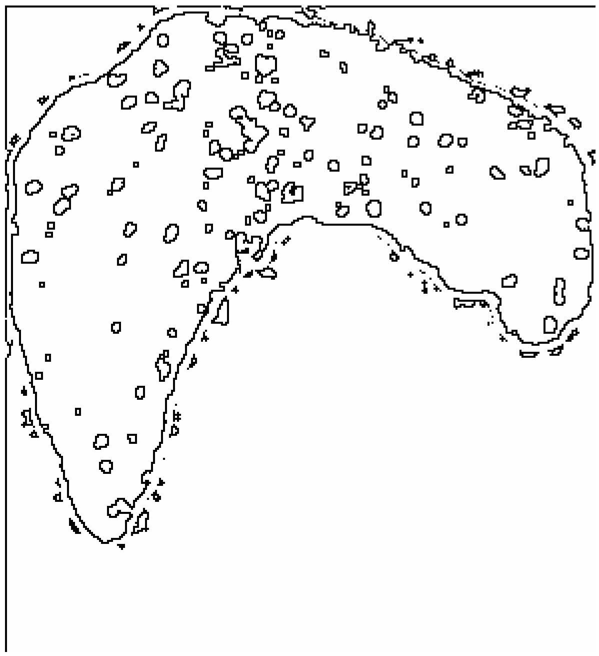

Figure E.4: Edge detection image.

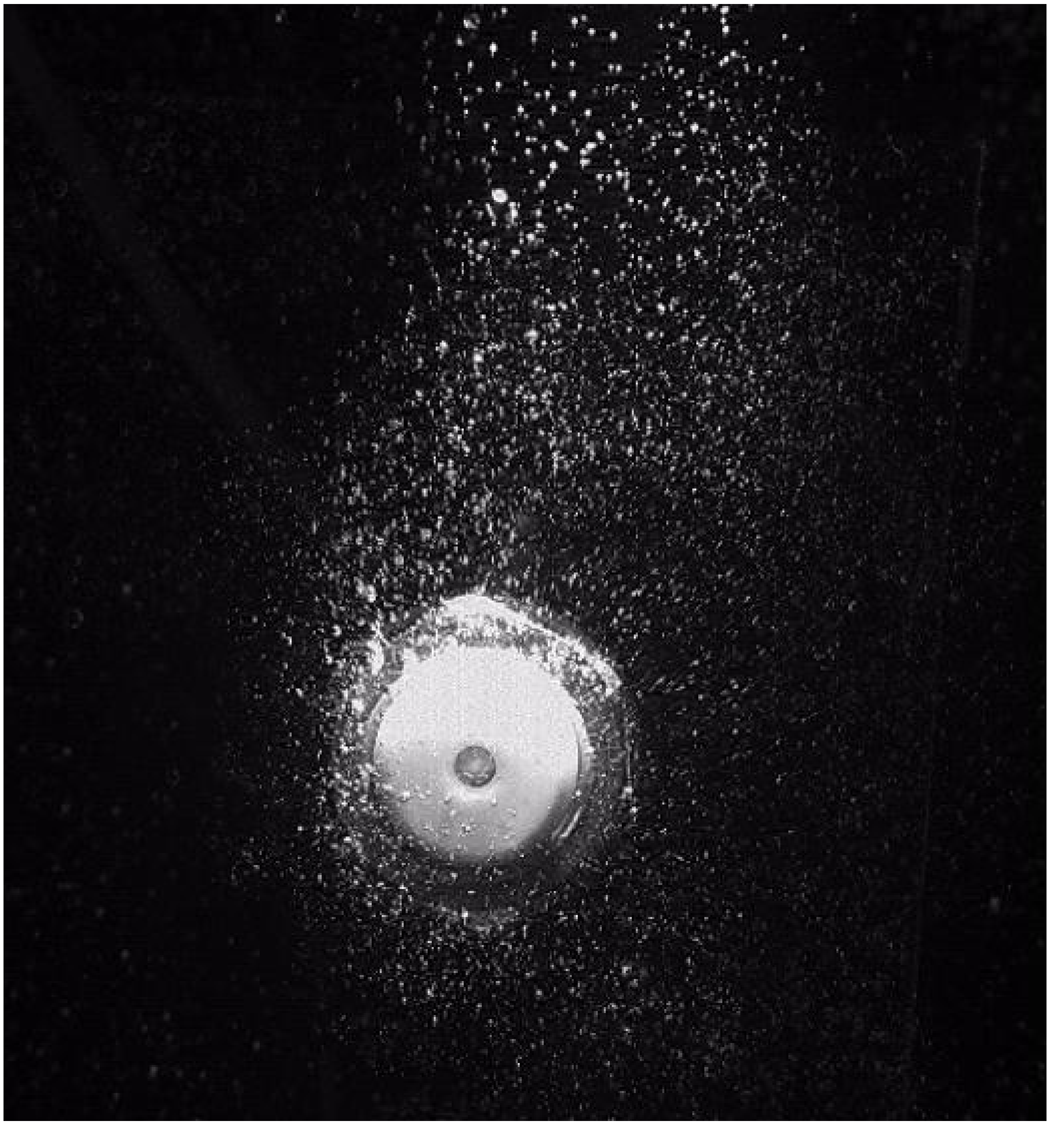

Figure E.5: Raw image.

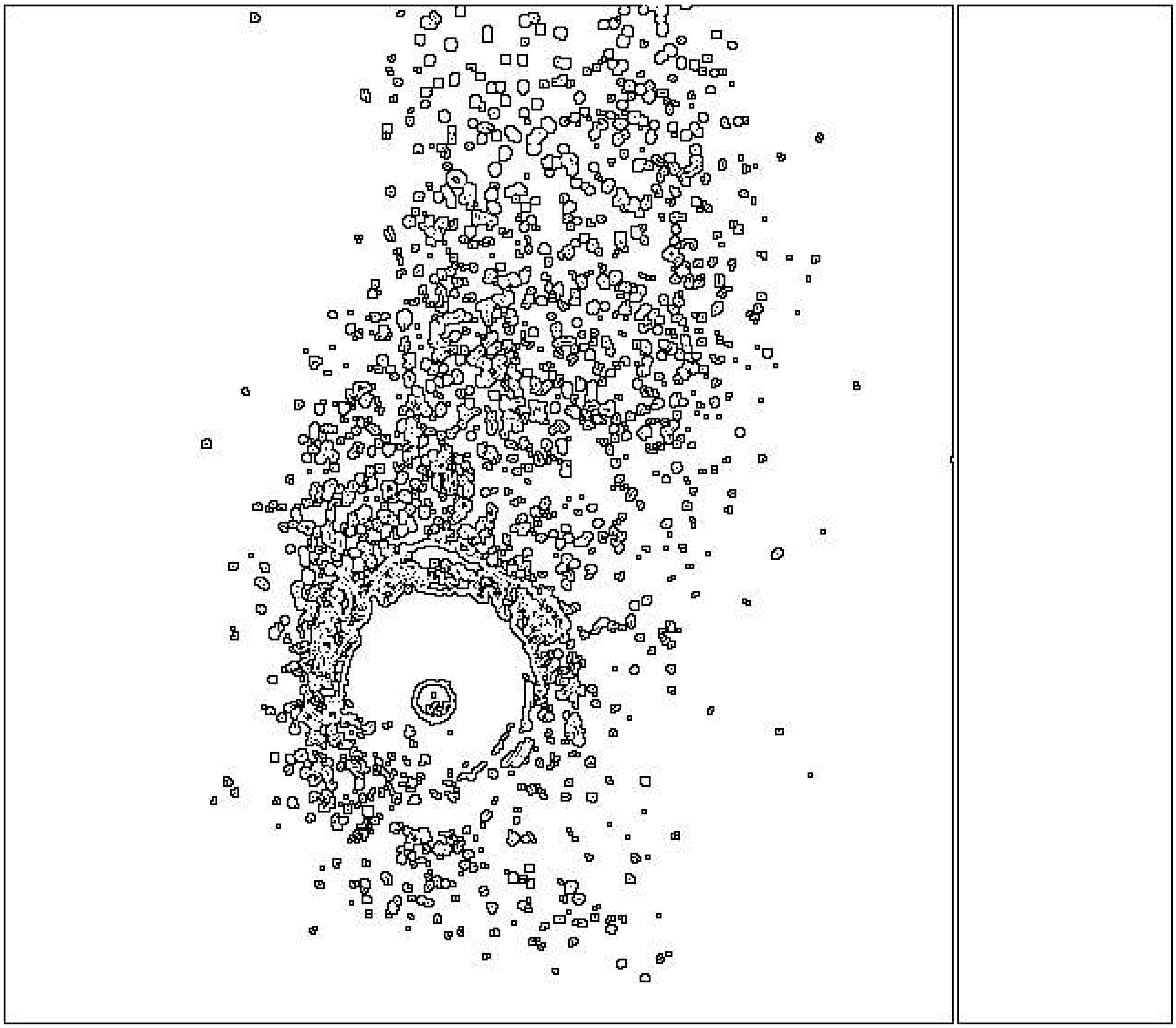

Figure E.6: Edge detection image.

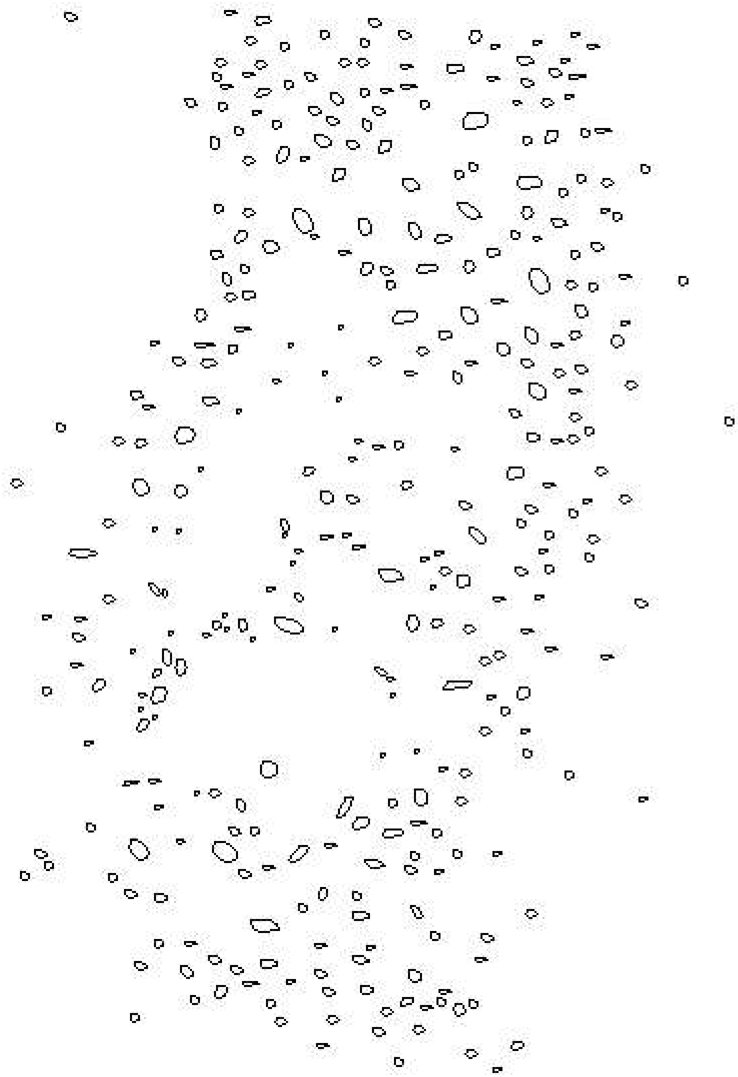

Figure E.7: Particle analysis image.

# APPENDIX F: IMAGE PROCESSING M-FILE

```
%%%%%%%%%%%%%%%%%%%%%%%%%%%%%%%%%%%%%%%%%%%%%%%%%%%%%%%%%%%%%%%%%%%%%%%
%%%

%%%%%%%%%%%%%%%%%%%%%%%%%%%%%%%%%%%%%%%%%%%%%%%%%%%%%%%%%%%%%%%%%%%%%%%
%%%

%Nitta Moore Image Processing

%%%%%%%%%%%%%%%%%%%%%%%%%%%%%%%%%%%%%%%%%%%%%%%%%%%%%%%%%%%%%%%%%%%%%%%
%%%

%%%%%%%%%%%%%%%%%%%%%%%%%%%%%%%%%%%%%%%%%%%%%%%%%%%%%%%%%%%%%%%%%%%%%%%
%%%


clear all;clc;


%%%%%%%%%%%%%%%%%%%%%%%%%%%%%%%%%%%%%%%%%%%%%%%%%%%%%%%%%%%%%%%%%%%%%%%
%%%

%Choose movie filename from disk

%%%%%%%%%%%%%%%%%%%%%%%%%%%%%%%%%%%%%%%%%%%%%%%%%%%%%%%%%%%%%%%%%%%%%%%
%%%


% cd 'C:\Documents and Settings\swalke18\Desktop\'

folder = 'C:\Users\Stu\HPT\Nitta_Moore\12_02_09 NM data';


l = ls(folder);

for i = 1:length(l)-2

    fprintf(1,'\t %i  %s \n',i, l(i+2,:))

end

i = input('import file #: ');

filename = l(i+2,:);    disp(['Loading... ' filename])
```

```
%%%%%%%%%%%%%%%%%%%%%%%%%%%%%%%%%%%%%%%%%%%%%%%%%%%%%%%%%%%%%%%%%%%%%%%
%

%Read movie file into Matlab

%%%%%%%%%%%%%%%%%%%%%%%%%%%%%%%%%%%%%%%%%%%%%%%%%%%%%%%%%%%%%%%%%%%%%%%
%


%Use mmreader codex to read filename to readerobj

readerobj = mmreader(filename);

vidFrames = read(readerobj);


%Truncate video file into time sets, data

for i = 1 : readerobj.NumberOfFrames

    data(i).cdata = vidFrames(:,:,:,i);

    data(i).colormap = [];

end


clear vidFrames

%%%%%%%%%%%%%%%%%%%%%%%%%%%%%%%%%%%%%%%%%%%%%%%%%%%%%%%%%%%%%%%%%%%%%%%
%%

%Create Image Data

%%%%%%%%%%%%%%%%%%%%%%%%%%%%%%%%%%%%%%%%%%%%%%%%%%%%%%%%%%%%%%%%%%%%%%%
%%


%%%%%

NumberOfFrames = 100;

%%%%%


if readerobj.NumberOfFrames<=NumberOfFrames
```

```
    NumberOfFrames = readerobj.NumberOfFrames;
end

disp(['Creating Data files from... ', filename])

%%Create time slices from movie data; Raw contains the x*y image data
for
%each time slice
disp(['Creating Raw Time Slice Data from... ', filename])
for i = 1:NumberOfFrames
        workingFrame = data(i).cdata;
        Raw(:,:,i) = workingFrame(:,:,1);
end
Frame = Raw;
[maxy,maxx,numberofframes] = size(Frame);
clear data

% %Adjust Contrast
% disp(['Creating Contrast Adjusted Data from... ',filename])
% Frame = Frame;
% for i = 1:NumberOfFrames
%     ContrastAdjustFrame(:,:,i) = imadjust(Frame(:,:,i),[0 .6],[0 1]);
% end
% Frame = ContrastAdjustFrame;

%%Sharpen Frame
disp(['Creating Sharpened Image Data from...', filename])
```

```
Frame = Frame;

H = fspecial('unsharp');

for i = 1:NumberOfFrames

    SharpFrame(:,:,i) = imfilter(Frame(:,:,i),H);

end

Frame = SharpFrame;


%%Filter speckle noise from time slice = Frame;

disp(['Creating Noise Filtered Data from... ',filename])

Frame = Frame;

for i = 1:NumberOfFrames

    NoiseFilterFrame(:,:,i) = medfilt2(Frame(:,:,i),[2 2]);

end

Frame = NoiseFilterFrame;


% %%Create Binary Frames from Frame

% disp(['Creating Binary Image Data from... ',filename])

% Frame = Frame;

% threshold = .01;

% for i = 1:NumberOfFrames

% %     threshold = graythresh(Frame(:,:,i));

%     BinaryFrame(:,:,i) = im2bw(Frame(:,:,i),threshold);

% end

% Frame = BinaryFrame;


%%Generates EdgeFrame data from Frame data using Prewitt

disp(['Creating EdgeFrame Data from... ', filename])
```

```
Frame = Frame;
threshold = .15;
for i = 1:NumberOfFrames
    EdgeFrame(:,:,i) = edge(Frame(:,:,i),'sobel',threshold);
end
Frame = EdgeFrame;

%Generate inverse of Frame image; make edges black and rest white
disp(['Creating Inverse Frame Data from... ',filename])
Frame = Frame;
for i = 1:NumberOfFrames
    ComplementEdgeFrame(:,:,i) = imcomplement(Frame(:,:,i));
end
Frame = ComplementEdgeFrame;

%%Morphologically clean unconnected pixels
Frame = Frame;
for i = 1:NumberOfFrames
    CleanFrame(:,:,i) = bwmorph(Frame(:,:,i),'clean');
end
Frame = CleanFrame;

% %%Morphologically clean individual pixels
% Frame = Frame;
% for i = 1:NumberOfFrames
%     BridgeFrame(:,:,i) = bwmorph(Frame(:,:,i),'bridge');
% end
```

```
% Frame = BridgeFrame;

%

% %%Morphologically clean unconnected pixels

% Frame = Frame;

% for i = 1:NumberOfFrames

%     CleanFrame(:,:,i) = bwmorph(Frame(:,:,i),'clean');

% end

% Frame = CleanFrame;


% %Morphologically open Frame

% Frame = Frame;

% for i = 1:NumberOfFrames

%     OpenFrame(:,:,i) = bwmorph(Frame(:,:,i),'open');

% end

% Frame = OpenFrame;


% %%Morphologically close Frame

% Frame = Frame;

% for i = 1:NumberOfFrames

%     CloseFrame(:,:,i) = bwmorph(Frame(:,:,i),'close');

% end

% Frame = CloseFrame;


% %%Calculate cross correlation from successive Frame data time slices

% %starting with time slice = StartFrame; store cross correlation as
xcorrFrame

% %with length = NumberOfCorrelations

%disp(['Creating Cross Correlation Data from... ', filename])
```

```
% Frame = EdgeFrame;

% StartFrame = 50;

% NumberOfCorrelations = 5;

% xcorrFrame = zeros(2*maxx-1,2*maxy-1,NumberofCorrelations);

% %NumberOfCorrelations = NumberOfFrames-StartFrame; %xcorr the

% %rest of the frames

% for i = 1:NumberOfCorrelations

%     xcorrFrame(:,:,i) = xcorr2(double(Frame(:,:,StartFrame+i-
1)),double(Frame(:,:,StartFrame+i)));

% end


% %%Calculate convolution from successive Frame data time slices

% %starting with time slice = StartFrame; store cross correlation as
xconvFrame

% %with length = NumberOfConvolutionss

% disp(['Creating Convolution Data from... ', filename])

% Frame = Raw;

% StartFrame = 50;

% NumberOfConvolutions = 5;

% xconvFrame = zeros(2*maxx-1,2*maxy-1,NumberOfConvolutions);

% %NumberOfConvolutionss = NumberOfFrames-StartFrame; %convolute the

% %rest of the frames

% for i = 1:NumberOfConvolutions

%     xconvFrame(:,:,i) = conv2(double(Frame(:,:,StartFrame+i-
1)),double(Frame(:,:,StartFrame+i)));

% end


% Frame = Frame;

% for i = 1:NumberOfFrames
```

```
%     LinCombFrame(:,:,i) =
imlincomb(1,double(ContrastAdjustFrame(:,:,i)),100,double(Frame(:,:,i))
);

% end

% Frame = LinCombFrame;


%%Combine Raw Data with Binary Frame to form transparent overlay

disp(['Creating transparent overlay data...', filename])

Frame = Frame;

OverlayFrame = 1*Raw;

for i =1:NumberOfFrames

    for j = 1:maxy

        for k = 1:maxx

            if Frame(j,k,i) == 0

                OverlayFrame(j,k,i) = 225;

            end

        end

    end

end

Frame = OverlayFrame;


% %Generate inverse of Frame image; make edges black and rest white

% disp(['Creating Inverse Frame Data from... ',filename])

% Frame = Frame;

% for i = 1:NumberOfFrames

%     ComplementEdgeFrame(:,:,i) = imcomplement(Frame(:,:,i));

% end

% Frame = ComplementEdgeFrame;
```

```
%%%%%%%%%%%%%%%%%%%%%%%%%%%%%%%%%%%%%%%%%%%%%%%%%%%%%%%%%%%%%%%%%%%%%%%
%%%%

%Plays movie of movie data, defined as one of the data matricees,

%with plot axis given by: minx, maxx, miny, maxy

%Default:minx=1,maxx=length(movie(1,:,1);miny=1;maxy=length(movie(:,1,:
));

%Data includes:Raw = Raw Image

%               EdgeFrame = Edge Data

%               Frame = Current Working Images

%               xcorrFrame = Cross Correlation between adjacent time
frames

%               xconvFrame = 2D Convolutino of successive time frames

%               NoiseFilterFrame = noise filtered data

%%%%%%%%%%%%%%%%%%%%%%%%%%%%%%%%%%%%%%%%%%%%%%%%%%%%%%%%%%%%%%%%%%%%%%%
%%%

disp(['Playing Movie of Data from...', filename])

movie = Frame;

miny=1;maxy=length(movie(:,1,1));minx=1;maxx=length(movie(1,:,:));

% minx = 100;

% maxx = 400;

% miny = 100;

% maxy = 350;

figure(1)

for i = 1:length(movie(1,1,:))

    imagesc(movie(miny:maxy,minx:maxx,i));

    colormap(gray);

    title([num2str(i)])

    pause(1/readerobj.FrameRate)
```

# APPENDIX G: HYDROPHONE SPECS

RESON

## Hydrophone TC4032

Low Noise Sea-State Zero Hydrophone

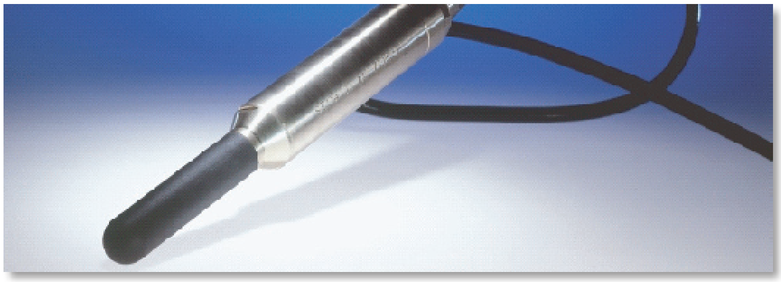

### TC4032

- Low noise performance
- High sensitivity
- Wide frequency range
- Flat frequency response
- Long term stability
- Individually calibrated

The TC4032 general purpose hydrophone offers a high sensitivity, low noise and a flat frequency response over a wide frequency range.

The high sensitivity and acoustic characteristics makes TC4032 capable of producing absolute sound measurements and detecting even very weak signals at levels below "Sea State 0".

The TC4032 incorporates an electrostatically shielded highly sensitive piezoelectric element connected to an integral low-noise 10dB preamplifier. The TC4032 preamplifier is capable of driving long cables of more than 1.000 meters, and the preamplifier features an insert calibration facility.
Per default the amplifier is provided with differential output. The differential output is an advantage where long cables are used in an electrically noisy environment. For use in single ended mode: Use positive output pin together with GND.
Versions with different filter characteristics are available: 4032-1 5Hz to 120 kHz, 4032-2 1Hz to 120 kHz and 4032-5 100Hz to 120 kHz.

| TECHNICAL SPECIFICATIONS | |
|---|---|
| Usable Frequency range: | 5Hz to120kHz |
| Linear Frequency range: | 15Hz to 40kHz ±2dB<br>10Hz to 80kHz ±2.5dB |
| Receiving Sensitivity: | -170dB re 1V/ μPa (-164dB with differential output) |
| Horizontal directivity: | Omnidirectional ±2dB at 100kHz |
| Vertical directivity: | 270° ±2dB at 15kHz |
| Operating depth: | 600m |
| Survival depth: | 700m |
| Operating temperature range: | -2°C to +55°C |
| Storage temperature range: | -30°C to +70°C |
| Weight in Air: | 720g without cable |
| Preamplifi er gain: | 10dB |
| Max. output voltage: | 3.5Vrms at 12VDC |
| Supply voltage: | 12 to 24VDC |
| High pass fi lter: | 7Hz -3dB |
| Quiescent supply current: | ≤19mA at 12VDC<br>≤22mA at 24VDC |
| Encapsulating material: | Special formulated NBR |
| Housing material: | Alu Bronze<br>AlCu10Ni5Fe4 |

www.reson.com

# Appendix H: Shaker Specs

Operating parameters of the ET-126HF Electrodynamic shaker.

| **PERFORMANCE** | **PHYSICAL** |
|---|---|
| Sine force | Armature weight 0.2 lb |
| Natural cooling 13 lbf pk | Suspension stiffness 15 lb/in |
| With blower 25 lbf pk | Rated armature current |
| Random force | Natural cooling 9 A rms |
| Natural cooling 8 lbf rms | With blower 17 A rms |
| With blower 17.5 lbf rms | Frequency range 2 DC-8,500 Hz |
| Shock force 53 lbf pk, 50 msec | Fundamental resonance 2 6,000-8,000 Hz |
| Max displacement | Stray magnetic field |
| Continuous pk-pk 0.75 in | Measured 1.0” above table <15 gauss |
| Between stops 0.75 in | Measured 0.5” from body <15 gauss |
| Maximum velocity 120 ips pk | Cooling 80 CFM @ 22 inch H20 |
| Acceleration 1,2 | Dimensions 6.5" H x 4.8" W x 4.25" D |
| Bare table 125 g pk | Shaker weight 11 lbs |
| 0.5 lb load 36 g pk | |
| 2 lb load 11 g pk | |
| Maximum acceleration | |
| Resonant 150 g pk | |
| Peak shock 175 g pk | |

## APPENIDX I: WOODS LIMIT DATA PROCESSING M-FILE

```
clc

% data(:,1) = f1000_1(1:10000,1);

% data(:,2) = f1000_2(1:10000,3);

% data(:,3) = f1000_8(1:10000,3);

% frequency_input = 1000;

% samplerate = 30000;

data = f_2500;

samplerate = 10000;

frequency_input = 2500;

%Bandwidth must be picked such that 2*bandwidth is greater than the
width of the center

%peak but 2*bandwidth < phase_diff*samplerate

bandwidth = input('Bandwidth= ')


for i = 2:length(data(1,:));

    L(i) = length(data(:,i));

NFFT = 2^nextpow2(L(i));

Y(:,i) = fft(data(:,i),NFFT)/L(i);

f = samplerate/2*linspace(0,1,NFFT/2+1);

end


fftdata = 2*abs(Y);


% Plot single-sided amplitude spectrum.

figure(1)

semilogy(f,fftdata(1:NFFT/2+1,2))
```

```
title('Single-Sided Amplitude Spectrum of y(t)')
xlabel('Frequency (Hz)')
ylabel('|Y(f)|')

%Calculate cross correlation between location x1 and x2
x1 = 2;
x2 = 6;
[A, lags] = xcorr(fftdata(:,x1),fftdata(:,x2),samplerate,'coeff');
del_f = 1/samplerate;

%Plot cross correlation as a function of phase difference
figure(2)
semilogy(2*lags/samplerate,A)
xlabel('Phase difference between location x1 and x2 (radians)')
ylabel('Correlation Coefficient of normalized fft at x1 and x2')

a = 1;
for i = bandwidth:length(A)-1
   maxA(i)=max(A(i-bandwidth+1:i));
end

%Plot the cross correlation spectrum with cutoff frequency given by
%bandwidth
figure(3)
semilogy(2*lags(1:length(lags)-1)/samplerate,maxA)
%semilogy(maxA)
grid on
```

```
%Guess threshold and main peak width from Figure 3

threshold_guess = input('Phase Difference Estimated threshold value= ')

if threshold_guess == 0

    break

end

mainpeakwidth = input('Guess of the main peak width= ')


j = 5;

threshold = threshold_guess;

while(j>3)

    clear peak

    clear as

    threshold = threshold + 0.001*threshold;

    a = 1;

peak(1) = 0;

for i = .25*length(maxA):length(maxA)

    if a == 1

       if maxA(i) > threshold

        peak(a) = 2*lags(i)/samplerate;

        as(a) = a;

        a = a+1;

        lasti = i;

       end

    else

        if maxA(i)> threshold && abs(lasti - i)>2*bandwidth

        peak(a) = 2*lags(i)/samplerate;
```

```
        as(a) = a;
        a = a+1;
        lasti = i;
        end
    end
end
j = length(peak);
end

frequency_input
phase_diff = sum(abs(peak))/(length(peak)-1)
L_waveguide = 0.91
wavelength = L_waveguide/(2*phase_diff)
c_meas = .15*frequency_input*(x2-x1)/(phase_diff)

figure(4)
plot(peak,as)

if 2*bandwidth > phase_diff*samplerate
    disp('BANDWIDTH ERROR1')
end
if 2*bandwidth<mainpeakwidth
    disp('BANDWIDTH ERROR2')
end
if length(peak)<3
    disp('BANDWIDTH ERROR3')
```

# APPENDIX J: NITTA MOORE HIGH SPEED IMAGING PROCEDURE

1) Initiate data acquisition
    a. Flow meter, power supply, DAQ board, MATLAB script
    b. Pressure gauge upstream from bubbler (0-60psi, 0-30psi, 0-15psi)
    c. Inverted tube assembly, specialized tank, 10cc graduated cylinder, He tank, two-stage regulator with 0-15psi gauge, stop watch
    d. Microphone assembly, mic, low-impedance cable, ICP unit, DAQ board, MATLAB script
    e. Strobotach
    f. 9MP still camera
    g. Olympus High Speed Camera
2) Check loop operation
    a. Visually inspect piping, pump, transfer pump, batch tank, bubble tank, bubbler, flow meter, pressure gauge, Swagelok connection, gas supply
    b. Install bubbler; double check compression fitting to fluid inlet, gas inlet, and mounting bracket; clamp flexible inlet tubing to bubble tank
    c. Check water cleanliness and level
    d. Remove unnecessary equipment from loop area
    e. Initiate gas flow at 10 psi and test inverted tube assembly; close valve at regulator outlet
3) Data acquisition: At each step pause and ensure loop operation
    a. Double check data matrix, data acquisition, and loop operation
    b. Fill batch tank via transfer pump; check water levels in batch and bubble tank

c. Always leave pump outlet valve open completely; open bypass valve; close main control valve to bubbler

d. Initiate flow through bypass via main pump

e. Open main flow valve completely to initiate flow through bubbler

f. Slowly close bypass valve until fluid pressure gauge reads 5psi; allow trapped gas to evacuate flow line; initiate flow meter and acquire flow rate for 20s , test microphone data acquisition

g. Slowly increase flow through bubbler via slow closure of bypass valve until desired upstream fluid pressure is obtained; record fluid flow rates via MATLAB script for 30s

h. Adjust gas flow via gas metering valve until desired bubble dispersion is obtained

i. Measure gas flow rate via inverted tube assembly; reinsert gas delivery tube; ensure desired bubble population

j. Obtain remaining data according to data matrix

k. Open bypass valve completely, shut off pump power, remove gas supply and close regulator shut off valve

l. Repeat (a-k) as desired

4) Double check data matrix; shut off all systems

# APPENDIX K: NITTA MOORE MICROBUBBLER PROCEDURE

--Ensure loop is operational; BATCH TANK, TEST TANK, FITTINGS, PUMP, TRANSFER PUMP, and NM BUBBLER; record placement of BUBBLER

--Ensure measurement methods are operational.

--Liquid measurement:

-Flow Rate: Turbine meter; m-file; power supply; scope; DAQ board

-BUBBLER inlet pressure; 30 psi dial gauge

-Flow bypass pressure; 15 psi dial gauge

--Gas measurement:

-Flow Rate; 10mL inverted tube assembly, inline gas flow regulator

-Inlet pressure; 15 psi dial gauge; 10 psi regulator

--Move liquid to BATCH TANK 1 using the TRANSFER PUMP.

--Open bypass to BATCH TANK 1. Close bypass to TEST TANK and close valve to NM BUBBLER.

--Increase 2-stage regulator pressure to 10 psi; adjust single stage pressure to ensure gas flow using the inverted assembly as a guide; connect flow to BUBBLER using Quick Connect fitting.

--Power on pump using a power strip, only one pump should be plugged in at a time; ensure fluid flow through BATCH TANK bypass.

--Slowly open BUBBLER control valve; observe flow rate measurement and BUBBLER inlet pressure increasing.

--Adjust BATCH TANK and TEST TANK bypass to reach desired fluid flow rate and inlet pressure.

--Adjust gas pressure and flow rate; record the effects on bubble population using the inverted tube assembly to record gas flow rates

# APPENDIX L: PROPOSED MICRO-BUBBLER PROTOTYPE

A swirling type micro-bubbler with lower liquid pressure drops than the Nitta Moore device, similar to that of Tabei (2007), is proposed for consideration as a test section within the test mercury flow loop. Figure 1 shows the layout from engineering sketches. The liquid and gas are supplied near the base of the swirl device. The liquid is delivered tangentially while the gas is delivered axially; the original design shows an axial gas injection tube which can be adjusted along the flow axis while the proof of concept device simply injects gas through a small bore orifice at the base. The proof of concept experiment was performed using the device in Figure 2. The liquid was supplied by the Nitta Moore loop and helium was delivered from a pressurized tank with 2-stage regulator and 0-30psi gauge. Figure 2 shows the prototypic device constructed from acrylic; two nozzles with diameter 4.5 and 8.5 mm have been constructed for further proof of concept experiments. Note the gas injection tube has not been included in this design. Figure 3 shows the device operating at near optimal gas and liquid inlet conditions with the 4.5mm ID nozzle attached. Helium was delivered axially through a Swagelok fitting similar to Fig.1(a) at 5psi and water was delivered tangentially according to Fig. 1(b) and 2(b) at 5L/min at ~10psi (these flow parameters are not arbitrary, small bubbles and a large gas void fraction were sought; liquid flow was increased to nearly the maximum available in the Nitta Moore loop and then gas pressure was adjusted to generate large voids yet still allowing adequate breakup). The device operation is shown in Fig. 3(a), the gas filament swirl can clearly be seen in Fig. 3(b), and jet mixing is shown in Fig. 3(c).

I propose that this device be optimized according to Tabei (2007) and Ganan-Calvo (2004). Scaling of this physics to mercury will lay the groundwork for eventual implementation in the test mercury flow loop. For water validation experiments, the construction of this device can be accomplished in-house in a minimal time period.

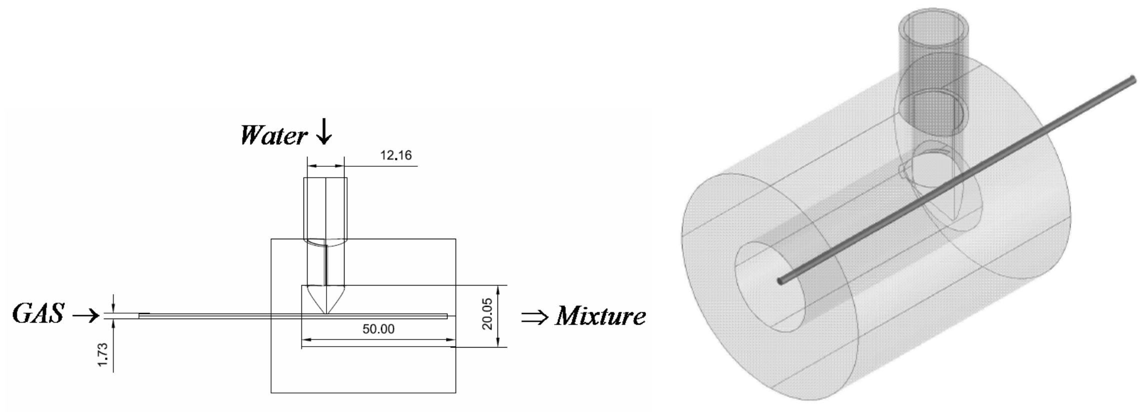


Figure L.1:Sketch of proposed swirl device.

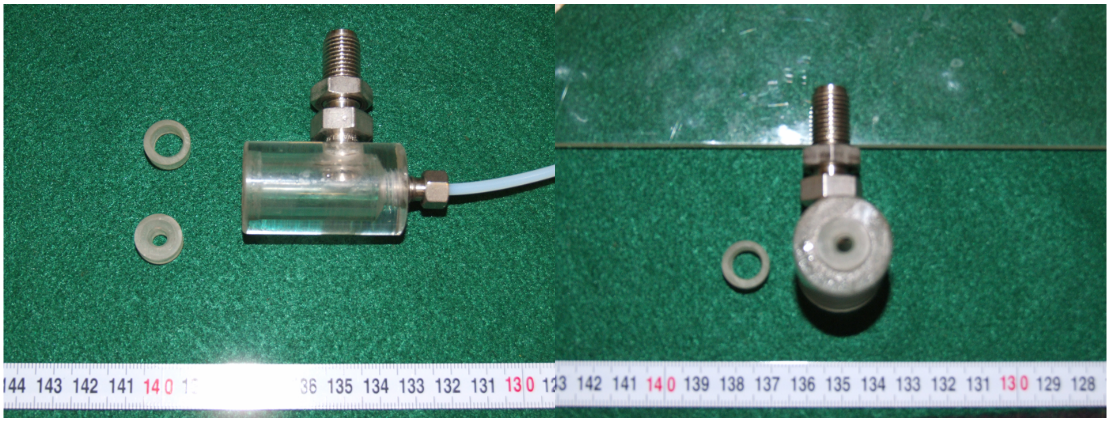


Figure L.2: Prototype swirling microbubbler.

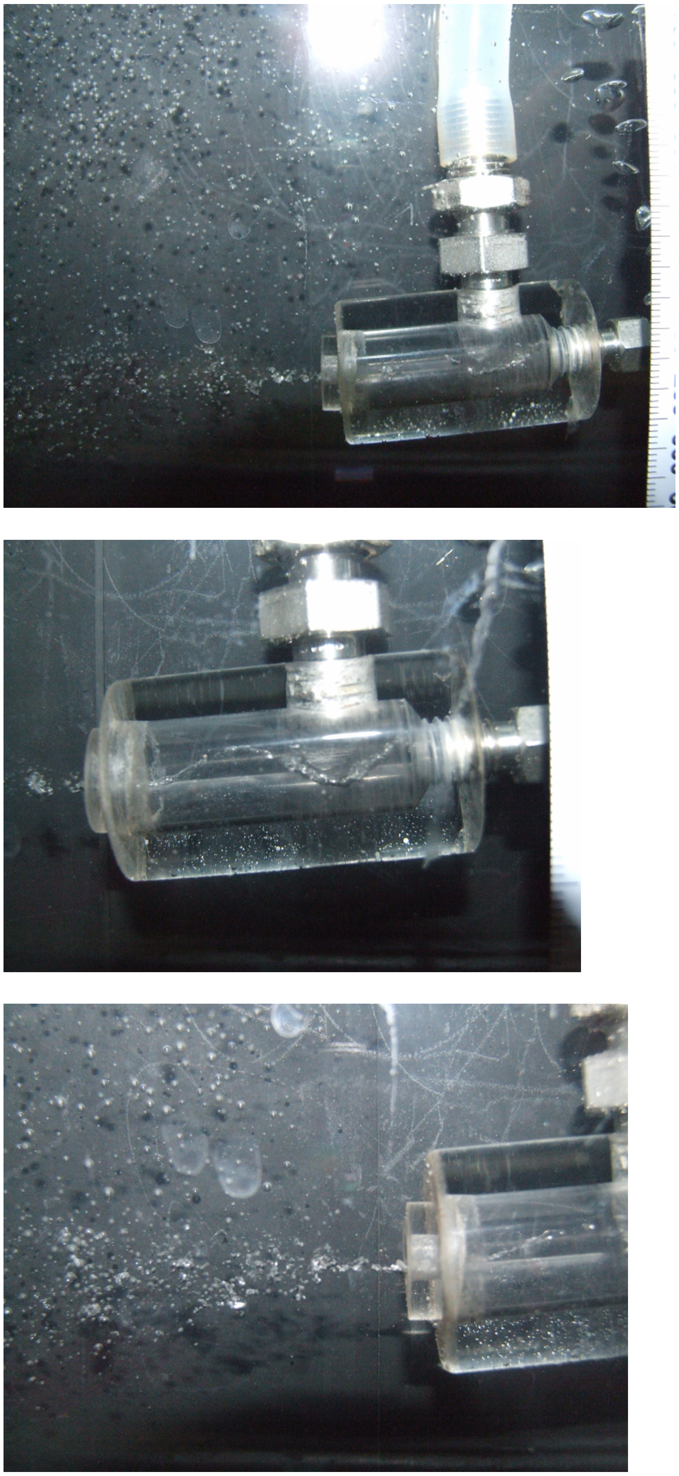

Figure L.3: Initial results of prototype micro-bubbler.

# APPENDIX M: WOODS LIMIT PROCEDURE

**Equipment:**

______: -Tank

______: -ED Shaker

______: -Laptop

______: -DAQ

______: -4-Channel ICP

______: -EDS Power Amp

______: -Scope

______: -Piston

______: -Catch Basin

______: -Accelerometer (10’ low noise cable)

______: -Pressure Sensor (10’ low noise cable)

______: -Gas Delivery System

  ______--Helium cylinder (two-stage regulator)

  ______--Single-stage cylinder (10 psi)

  ______--Metering valve

  ______--Various tubing and valves

  ______--Inverted tube assembly

______: -Camera

______: -Overhead projector

______: -UVP (2 transducers)

______: -1” tubing (15’)

______: -Crescent wrench (X2)

______: -“C”-Clamp

______: -Sink/faucet

**Pre-fill Procedure**

______: -Equipment checklist

______: -Test gas delivery system

______--Zero out inverted tube assembly

--Purge two-stage regulator to 15 psi before connecting to system/close shut-off valve

--Check all connections according to Appendix A (V1:0,V2:0,V3:1,V4:0,3W:2,MV:0)

______--Reduce gas pressure to 5 psi using single stage regulator and dial guage

______--Ensure bubble formation at the inverted tube assembly

______--Set V1:1

______--Detach homogenizer inlet for DAQ testing

: -Test DAQ system

--Check all connections according to Appendix A

--Power Up Laptop

______--Load LabView VI Module (C:\My Documents\Woodslimit.vi)

______--Power up Scope

______--Power up ICP unit

______--Switch between channels 1 + 2 ensuring that the each circuit is complete

______--Ensure gain on EDS power amp is set to 0

______--Power up EDS power amp

______--Set ‘Write Measurement’ file to a test folder

______--Set signal generation at 500 Hz

______--Switch ICP unit to accelerometer channel

______--Run VI observing the signal generation on the scope output

--Slowly increase the EDS amp gain until the accelerometer output is approximately 1.0V

______--Allow data to collect for 10 seconds and reduce gain to 0

______--Switch ICP unit to pressure sensor channel

______--Reduce gas pressure to 2 psi using the single stage regulator

______--Activate pressure sensor with 2 psi He observing the response

--Stop VI

--Shut off gas flow using two-stage shut off valve

--Attach homogenizer inlet

______--Import data into EXCEL worksheet

______--Test camera and overhead projector

______--Test UVP

**Fill Procedure**

______: -Ensure tank is within catch basin

______: -Attach piston to tank and EDS

______: -Attach 1” tubing to faucet using hose clamp

______: -Secure 1” tubing to tank using “C” clamp

______: -Slowly increase water flow until tank is filled to predetermined mark

**Data Acquisition Procedure**

______: -Set (V1:0, V2:0, V3:1,V4:0, 3W:2)

______: -Increase gas pressure using single stage regulator to 5 psi

______: -Set gas flow rate using the inverted tube assembly

______: -Set (V1:0, V2:0, V3: 1, V4:1, 3W:1)

______: -Set homogenizer power level

______: -Ensure bubble formation using camera and UVP

: - Using the VI determine a pressure response for input signals over a range of frequencies for a given amplifier gain (500 – 2000 Hz); always reduce the gain before starting and ending the VI

: -Retest for a new flow rate or homogenizer power level

: -Set (V1:1, V2:1, V3:1, V4:1, 3W:1)

**Siphon Procedure**

______: -Using 1” tubing siphon water from tank to the sink drain

______: -Remove piston and EDS

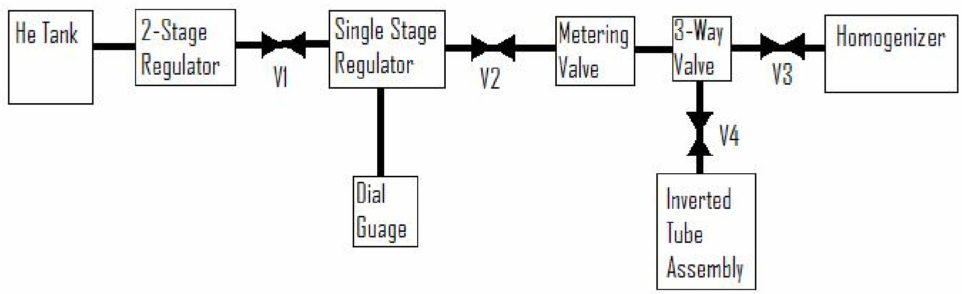


He Tank—Helium cylinder (~500psi)

V1-V4: Globe valves (0:open,1:closed)

3-Way Valve: (1:V3,2:V4)

## Appendix N: Piston Assembly for Woods Limit Examination

The piston assembly will consist of a membrane sandwiched between two aluminum disks. Part 1 from Figure 1 is the front active face of the piston. This disk will be machined from 6061 aluminum to 1.5” dia. and ¼” thick. A ½” dia. ¾” long nipple will be machined in the center of the disk and threaded with 13 threads/inch. A ½” deep 10-32 hole will be drilled and tapped in the center of the nipple for attachment to the ED shaker. The second disk (Part 4) will be ¼” thick disk with a through hole large enough to easily fit around the nipple and will be secured to the front piston using a ½”-13 aluminum nut (Part 5). A 1.5” long 10-32 threaded rod (Part 3) will connect the piston assembly to the center hole of the ED shaker. The mass of the piston assembly should be approximately 60 g.

Table 1: Parts list for the piston assembly

| | | |
|---|---|---|
| 9062K231 | 1.5”X12” Al 6061 Rod precision ground | 34.39 |
| 93225A782 | 10-32 Al 6061 threaded rod 1.5” long pack of 25 | 8.93 |
| 90670A033 | ½”-13 Al nut pack of 25 | 8.15 |
| 8574K55 | ¼” thick 24” square clear polycarbonate | 34.21 |
| 85995K11 | 0.004” thick latex rubber 6” wide 1 yard | 2.03 |
| 85995K13 | 0.008” thick latex rubber 6” wide 1 yard | 2.31 |
| 93190A542 | ¼”-20 SS-316 cap screws pack of 25 | 12.09 |
| 91850A029 | ¼”-20 SS-316 machine nuts pack of 50 | 12.50 |
| 91950A029 | ¼” SS-316 plain washer pack of 50 | 7.59 |
| 7587A33 | Dow 732 multipurpose clear silicone 10.1 oz | 5.91 |

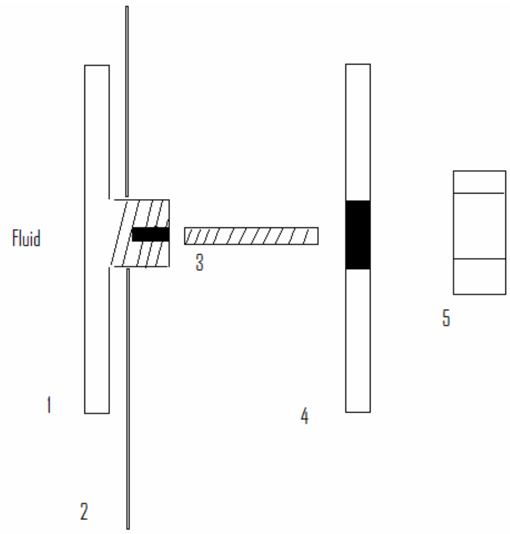


Figure 1: Exploded diagram of piston assembly. Not drawn to scale. Including: Part 1: Front Piston Face, Part 2: Latex Membrane, Part 3: 10-32 Threaded Rod, Part 4: Back Piston, Part 5: Securing nut

# APPENDIX O: CO-FLOW BUBBLER TEST SECTION DESCRIPTION

Producing micro-bubbles in a mercury flow remains a challenge. A proposed dead-leg bubbler section has been tested in mercury with inconclusive results. Another design proposal placed swirling jet bubblers in-line with the mercury flow using a flow diversion to supply mercury to the bubblers and an external helium supply; a schematic is given in Figure 1.

Testing of the in-line design was initiated by placing several sections of tubing at the exit nozzle. Previous testing indicated that the swirling flow would be preserved downstream and centrifugal forces would confine the gas to the centerline of the flow; this can be seen in Figure 2. By placing the bubbler off the pipe centerline and increasing the pipe diameter to 15 times the nozzle diameter (the pictured pipe diameter is 2.5") a shear layer develops and the gas breakup mechanism is preserved Figure 3.

The main tests were conducted using a flow loop constructed from 1" PVC. The test section is shown in Figure 4. The main flow is diverted through the bypass to the Nitta-Moore bubbler; each bubbler has an individual supply control valve. The bubbler test section houses the two NM devices in a 6" diameter section; pictured in Figure 5.

A typical bubble cloud is shown in Figure 6; the nozzle OD of 20mm was used as a reference measurement. The milky bubble cloud seen in Figure 3 is not present. Bubble sizes were measured in a 250mm square subsection of the figure. A histogram of the measured bubble diameters is given in Figure 7; an average bubble diameter of

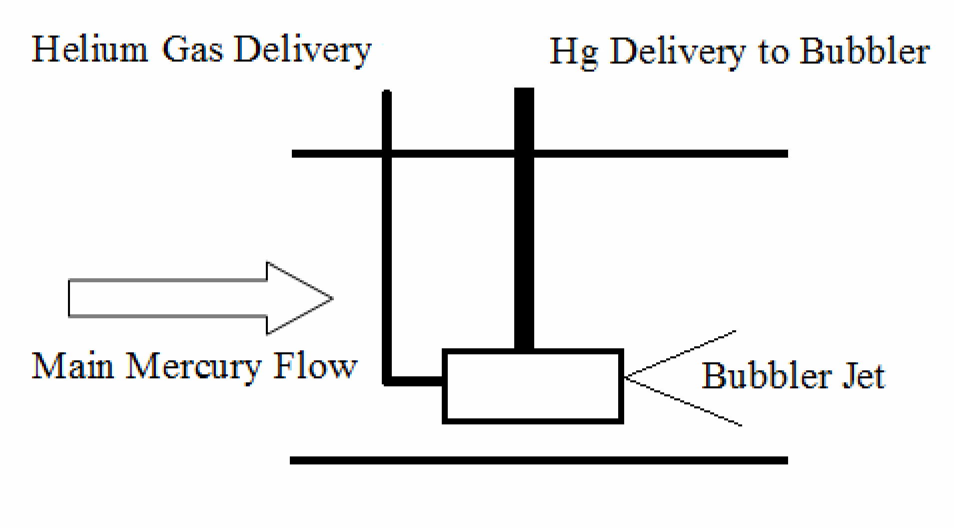


Figure O.1: Schematic of co-flowing test section.

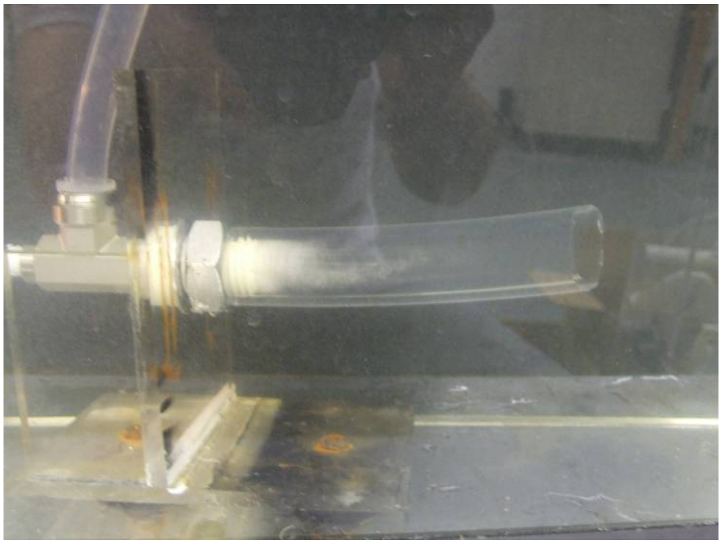

Figure O.2: Small diameter pipe attached to the nozzle exit; the swirling flow is confined by the pipe walls and a centerline gas filament is established.

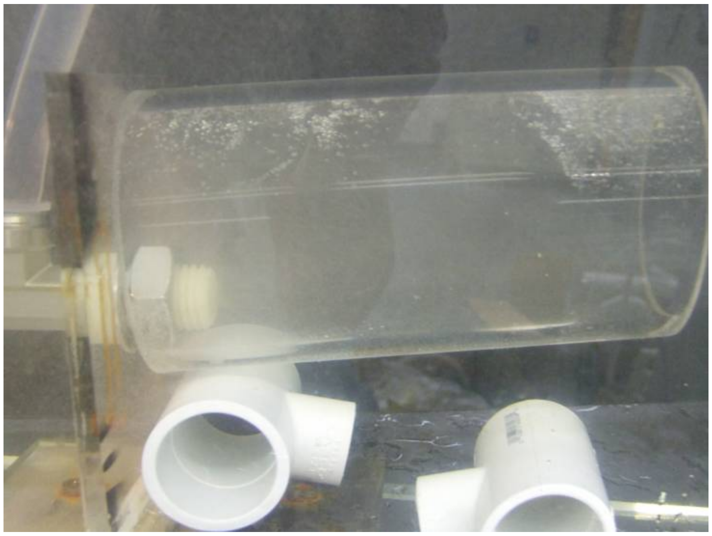

Figure O.3: A larger pipe diameter and off-center bubbler placement allows the development of the shear layer.

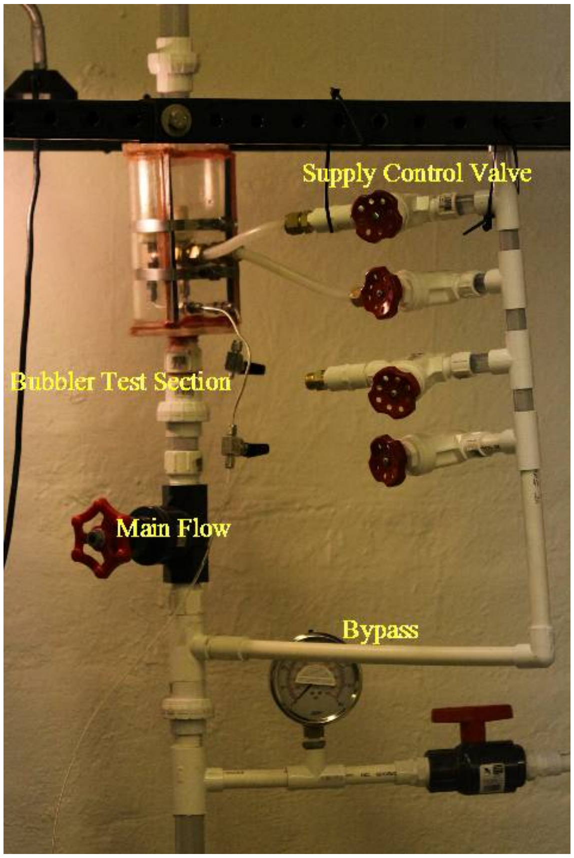


Figure O.4: Bubbler test section and water delivery bypass.

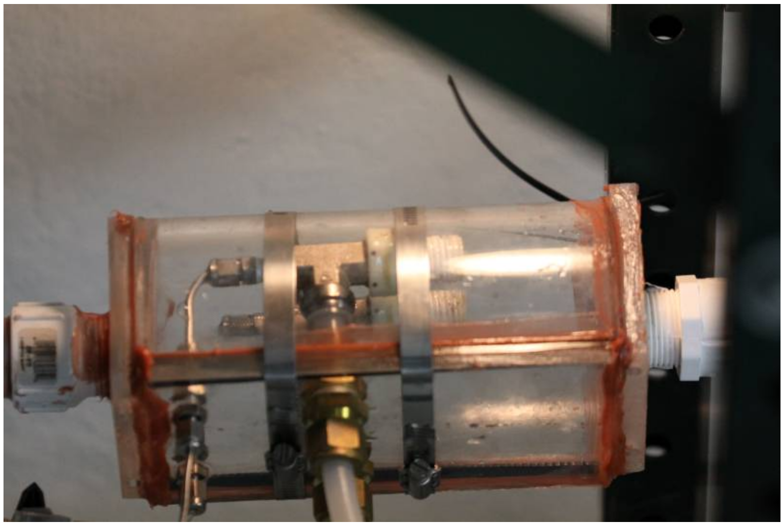

Figure O.5: Bubbler test section.

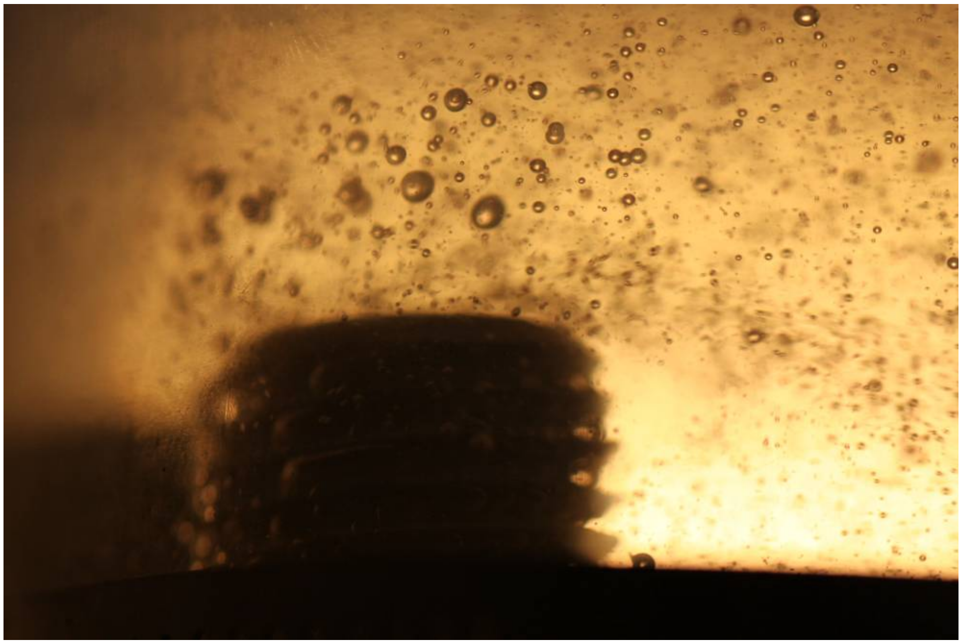

Figure O.6: Optimal bubble production; average radius is ~170micron.

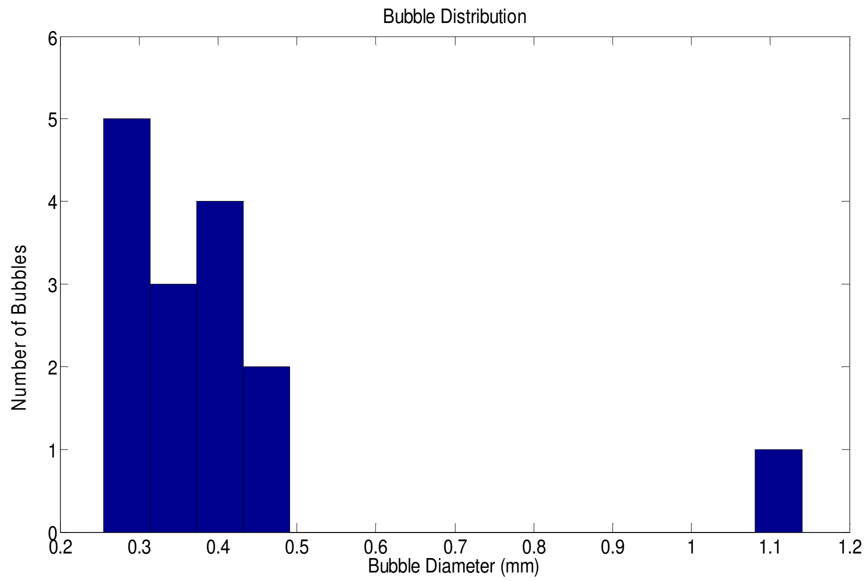


Figure O.7: Histogram of measured bubble diameter.

374microns was measured. The average bubble diameter is approximately 400% larger than the situation without co-flow. [1]

The co-flow bubbler design has overcome the tendency of the swirling flow to be preserved downstream using a large diameter reservoir and off-centerline placement. The presence of a co-flowing stream leads to the production of larger bubbles compared to the case without a co-flowing stream. The measured bubble diameters indicate that bubbles of 100micron diameter are not present therefore one would expect that the bubble breakup mechanism is being impeded. The presence of very large bubbles (~1mm diameter) may be attributed to the long residence times of the bubbles within the test chamber leading to coalescence.

[1] Ruggles, A.E., Walker, S. Mercury Scaling of a Swirling Jet Micro-Bubble Generator. FEDSM2010-ICNMM2010-30534

# APPENDIX P: CRITICAL BUBBLE DIAMETER CALCULATION IN A PIPE FLOW

```
%Calculates the critical bubble diameter in a pipe system using Weber

%numbers based on bulk dynamic pressure and turbulent dynamic pressure
for

%the mixer model (Clay) and the free jet model (Martinez-Bazan)


%Water

% sigma = 0.075

% rho = 1000

% We_crit = 10

% c1 = 1.5

% c2 = 2.6

% visc = 1e-6

% D_pipe = .1

% v = [0:.01:5];


%Mercury

sigma = 0.486

rho = 13500

We_crit = 10

c1 = 1.5

c2 = 2.6

visc = .1e-6

D_pipe = .1

v = [0:.01:5];
```

```
D_relap = We_crit.*sigma./(rho.*v.^2);

D_turb1 = c1.*(sigma/rho)^(3/5).*D_pipe^(1/2).*visc^(-1/10).*v.^(-
11/10);

D_turb2 = c2.*(sigma/rho)^(3/5).*D_pipe^(1/2).*visc^(-1/10).*v.^(-
11/10);

semilogy(v,D_relap,v,D_turb1,v,D_turb2)

legend('RELAP Model', 'Mixer Model', 'M-B Jet Model')

xlabel('Bulk Velocity (m/s)')

ylabel('Maximum Bubble Diameter (m)')

title('Comparison of RELAP and Turbulence Critical Bubble Diameter
Models for Mercury')

grid on
```

# CURRICULUM VITAE

**Stuart A. Walker**

PhD Candidate
The University of Tennessee
Nuclear Engineering Department
Arthur E. Ruggles, Advisor

**Education**
Master of Science – Nuclear Engineering – The University of Tennessee, January 2010.

Computational Fluid Dynamics Graduate Certificate – Engineering Science – The University of Tennessee, August 2009.

Bachelor of Science – Nuclear Engineering – The University of Tennessee, December 2007.

**Work History**
January 2011 to Present, Doctoral Research Assistant, The University of Tennessee. Conduct research under contract with the HFIR RRD group pertaining to fuel-coolant interactions and the associated steam excursion. Analysis of in-vessel energy source terms and the subsequent fluid structure interaction.

August 2009 to December 2010, Doctoral Research Assistant, The University of Tennessee. Conduct research under contract with the Spallation Neutron Source (SNS) pertaining to turbulent breakup of gas bubbles in a water and liquid metal application. Also, the development of a 2Bar mercury flow loop for testing turbulent bubble generation.

January 2007 to August 2009, Graduate Research Assistant, The University of Tennessee. Conduct research under contract with the Spallation Neutron Source (SNS) pertaining to bubble production and detection techniques in a liquid metal application. Thesis research examined the relationship between gas volume fraction and sound speed within the Woods limit as well as inertia controlled bubble formation in mercury.

January 2006 to January 2007, Undergraduate Research Assistant, The University of Tennessee. Conduct research under contract with the Spallation Neutron Source (SNS) correlating bubble rise velocity measurements via particle image velocimetry and ultrasonic Doppler shifting.

**Special Skills**
Experience in finite element numerical simulation and algorithm construction of the Reynolds averaged conservation principles with emphasis on turbulence closure models.